

Doctoral Dissertation

博士論文

A Study of the Soft X-ray Diffuse Background in 0.2-2 keV
with the Suzaku Observatory

(すざく衛星を用いた0.2-2 keVにおける軟X線背景放射の研究)

A Dissertation Submitted for the Degree of Doctor of Philosophy
March 2019

平成 31 年 3 月 博士 (理学) 申請

Department of Physics, Graduate School of Science,
The University of Tokyo

東京大学大学院 理学系研究科 物理学専攻

Kenichiro Nagayoshi

永吉 賢一郎

Acknowledgements

I would not have been able to complete this thesis without kind, dedicated, persevering and continuing supports I have got from many people. About four years have past since I started working on this project and I am writing this last part of my thesis finally. I would like to express my gratitude here.

I sincerely thank to my supervisor Prof. K. Mitsuda. My idea one day came up "use the *Suzaku*'s 1/4 keV band" has been brushed up through constructive discussions with him and grown up to the core of this thesis. His insights and comments on data analysis results based on a deep scientific knowledge have been always sharp and to the point. He have taught me how to think logically when I lost the way. He has been incredibly patient and so kind over the last four years. I genuinely respect you and it is an honor to be taught by you.

I would like to thank to Prof. N. Y. Yamasaki. Without her scientific advices, encouragements and kindness, I would not have been able to continue this project. I have learned a lot from you how to approach to difficult subjects by changing a point of view, and importance to get rid of a biased way of thinking. I will not forget what once you told me "Any data says something, regardless of whether you want it or not.". I know I have kept you worried about me. I apologize deeply but nevertheless, I am sincerely grateful to you.

Secretaries N. Takahashi and A. Yokoyama have helped me a lot especially when I visited to ISAS form SRON. They have cheered me up always and I have enjoyed daily chatting with them. "Thank you" is not enough for all the help I have received from you.

I thank to my colleagues in the lab.: N. Sekiya, K. Sakai, R. Yamamoto, T. Kikuchi, T. Hayashi and M. Muramatsu. We have talked a lot about our detector development and that kind of things have helped me recover when I was in a tough moment.

Finally I appreciate my parents for their great help and encouragement over a number of years.

Kenichiro Nagayoshi

Abstract

The hot gas of 0.1 keV filled in the cavity surrounding the solar neighborhood (so-called local bubble; LB) has been studied since the beginning of X-ray astronomy, as one of the emission components which contributes to the Soft X-ray Diffuse Background (SXDB) below 2 keV. However, another local diffuse component has become evident since 1990s; the emission induced by the charge exchange interaction of the solar wind and neutrals in the Heliosphere (H-SWCX; Heliospheric Solar Wind Charge eXchange). The properties and possibly even existence of the LB has been suspected due to this discovery. Moreover, it has been also pointed out since 1970s that the LB cannot be in dynamical equilibrium because the pressure of the hot gas in the LB far exceeds the thermal pressure of the interstellar medium (ISM). X-ray spectroscopy with modern X-ray CCD instruments is one of the keys to deepen our understanding of the SXDB. However, the energy band below 0.3 keV has not been available mainly due to instrumental issues, while the bulk of the emissions from the LB and H-SWCX would present in 0.1-0.3 keV.

In this thesis, we for the first time enable quantitative spectral analysis for the SXDB in 0.17-2.0 keV and investigate the origin of the local diffuse emission. The core of our research is the XIS1 CCD instrument on-board the *Suzaku* observatory. It is known as one of the best detectors to study the SXDB owing to the low and stable background, good energy resolution and excellent Gaussian-like response for monochromatic X-rays. However, due to uncertainty in contamination accumulation in orbit, the energy band below 0.4 keV could not be analyzed.

The neutron star RXJ1856.5-3745 is known as a standard calibration source for the low energy band. We carefully analyzed data taken from 2005 to 2014 biannually and discovered that the degradation of the quantum efficiency below 0.3 keV is well explained if we assume existence of sulfur as a new contaminant element. We developed a new contamination growth curve based on this result and validated that the calibration accuracy is significantly improved within $\pm 10\%$ below 0.4 keV from 2005 to 2014.

Our SXDB analysis was performed toward the Lockman Hole field, known as a blank field without bright sources. *Suzaku* observed this field annually from 2006 to 2012, corresponding to the period for which the solar activity migrated from minimum to maximum. The H-SWCX

emission is the only time-variable component in the SXDB reflecting the solar activity. We compared spectra observed in the solar minimum (2006-2009) and solar maximum (2010-2012) periods and found a systematic brightening in the solar maximum spectrum over the range of 0.17-1.0 keV. It became clear that the H-SWCX emission does contribute to the SXDB spectrum below 0.3 keV at least in the solar maximum period. In contrast, we found that the spectrum below 0.3 keV taken during the solar minimum period is well explained only with a thermal emission model characterized by temperature of 0.093 (0.06-0.11) keV. This result is consistent with the historical LB picture and suggests the contribution from the H-SWCX is minimal.

The SWCX-contributed spectrum was evaluated with existing H-SWCX models and revealed that none of the models can fully explain the observation. There seems an uncertainty in modeling of the emissions from heavier ions for example Si, S, Mg and Fe, whereas the emissions from C, N and O are in good agreement with the observed spectrum. We also estimated the pressure of the LB to be $p/k = 8.1 (5.9 - 9.1) \times 10^3 \text{ cm}^{-3} \text{ K}$. This value is still higher than the ISM pressure of $\sim p/k = 2 \times 10^3 \text{ cm}^{-3} \text{ K}$ but about half of the LB pressure estimated in 1970s. The pressure of the magnetic field is estimated to be $\sim p/k = 8 \times 10^3 \text{ cm}^{-3} \text{ K}$. If the LB is relatively free of the global magnetic field, then it can be in pressure equilibrium with the environment around the LB.

Table of contents

List of figures	ix
List of tables	xvii
1 Introduction	1
2 A Review	5
2.1 Brief History of the Soft X-ray Diffuse Background below 1 keV	5
2.2 Spectrum, Intensity, and Origins of the CXB above 2 keV	8
2.2.1 Spectrum of the CXB above 2 keV	8
2.2.2 Resolving the CXB into Point Sources	9
2.3 Spectrum, Intensity, and the Origins of the SXDB	10
2.3.1 The SXDB in the 1/4 keV Band and the Local Bubble (LB)	11
2.3.2 Heliospheric SWCX	15
2.3.3 Hot Gas in the Halo of our Galaxy	18
3 Instrument	21
3.1 The <i>Suzaku</i> X-ray Observatory	21
3.2 The X-ray Imaging Spectrometer	23
3.2.1 Basics	23
3.2.2 Energy Gain and Resolution	26
3.2.3 Non X-ray Background	29
3.3 Degradation of the Low Energy Quantum Efficiency	29
4 Revising the Quantum Efficiency Calibration Model for the XIS1 Instrument	31
4.1 Purpose of Analysis	31
4.2 RX J1856.5-3754 as a soft X-ray calibrator	32
4.3 Observation and Data Reduction	33
4.3.1 Observational Data Set	33

4.3.2	Data Screening	36
4.4	Non X-ray Background	38
4.5	Detector Response Function	38
4.6	X-ray background	38
4.7	Spectral model	40
4.8	Spectral Analysis	42
4.9	Revising Contamination Growth Model	49
4.10	Discussion	55
5	Spectral Analysis of the Soft X-ray Diffuse Background in 0.2-2.0 keV	57
5.1	Purpose of Analysis	57
5.2	Observations and Data Reduction	58
5.3	Spectral Modeling	64
5.3.1	Extragalactic Component: CXB	64
5.3.2	Galactic Component: Hot Galactic Halo	64
5.3.3	Local Component 1: Hot Gas in the LB	64
5.3.4	Local Component 2: H-SWCX Line Emissions	64
5.4	Spectral Analysis Results	67
5.4.1	Investigation of the Origin of the Local Emission	67
5.4.2	Characterization of the excess emission in the LH10-12 spectrum .	72
5.5	Systematic Errors	79
5.6	Discussion	81
5.6.1	Possible H-SWCX detection at ~ 0.7 keV	81
5.6.2	Discrepancy between the SWCX-contributed spectrum and Gaussian H-SWCX Emission Model	83
5.6.3	Pressure of the LB	85
6	Conclusions	89
	References	91
	Appendix A Data Screening with the Day Earth elevation angle	97
	Appendix B Modeling of the H-SWCX Emission	103

List of figures

2.1	The band response function of the <i>ROSAT</i> position sensitive proportional counter with definitions of the energy bands. B-band, C-band, M-band and I-band for the Wisconsin sound rocket experiment are marked over the plot. L-band and M-band for Tanaka and Bleeker (1977) are also indicated. . . .	6
2.2	Comparison of the instrumental response functions to the monochromatic 0.37 keV X-ray for <i>Chandra</i> (red), <i>XMM-Newton</i> (blue) and <i>Suzaku</i> (black and green).	7
2.3	X-ray background spectra (photon spectrum $\times E^2$, presented in the right figure) and the intensity in 2-10 keV band obtained with different instruments is shown in the left figure. Taken from Revnivtsev et al. (2003).	8
2.4	X-ray background spectra from 3 keV to 1 MeV observed with the HEAO-1 observatory. Taken from Boldt (1992).	9
2.5	$\log N - \log S$ plot of the CXB in the 2-8 keV band obtained with Chandra. Contribution of object types are shown with different colors and marks: AGN (blue triangles), galaxies (red rectangles), and stars (green stars) (Lehmer et al. (2012)).	10
2.6	Top: C band (~ 0.2 - 0.3 keV) counting rate obtained with the Wisconsin sounding rocket all sky survey plotted as a function of total Galactic Hydrogen column density of the direction (N_H). Bottom: B-band (~ 0.1 - 0.2 keV) to C-band count rate ratio plotted as a function of N_H . The ratio of the transmissions of N_H in B to C bands is plotted with a dashed line, which is very different from the observation. Thus, although the C band intensity shows anti-correlation with N_H , it can not be due to the Galactic absorption. Figures are taken from McCammon and Sanders (1990).	12

2.7	ROSAT counting rates in the directions of the MBM-12 molecular cloud ($D \sim 100$ pc) plotted as functions of $100 \mu\text{m}$ far infrared intensity (I_{100}) (Snowden et al. (1993)). Three panels show different energy bands, ROSAT R12 (1/4 keV) band, R45 (3/4 keV band), and R67 (1.5 keV) band. The $100 \mu\text{m}$ intensity is known to show correlation with the total (atomic + molecule + dust) H column density of the direction; $(N_{\text{H}}/10^{20} \text{ cm}^{-2}) = 1.4I_{100}(\text{MJy sr}^{-1}) + 0.15$	13
2.8	Spatial extension of the LB estimated from the ROSAT 1/4 keV band observation (left) and spatial extension of local cavity estimated from for NaI Fraunhofer D1 and D2 absorption lines of local ~ 900 stars whose distances were determined by the Hipparcos satellite. Figures are taken from Snowden et al. (1998) and Lallement et al. (2003).	14
2.9	ISM pressure as a function of vertical distance from the Galactic plane at the solar neighborhood. Original figure was taken from Cox (2005), and annotations are added. The two horizontal lines (orange and green) show the LB pressures from the literature. The total pressure at the mid plane is explained by a sum of four pressure components shown in the figure.	15
2.10	The spectrum of SWCX emission calculated by Koutroumpa et al. (2009) (Figure is taken from Kuntz (2019)). This spectrum was compiled from various theoretical calculations of cross sections and using carefully selected solar wind abundances. However, note that there are still significant uncertainties left in line intensities and ratios. The bulk of the emission is in the 1/4 keV band and is composed of many lines from various species and ionization states. The 3/4 keV band is, on the other hand, contributed by a few lines.	17
2.11	Long-term variation of the O_{VII} intensity toward the Lcokman hole direction obtained with the Suzaku observation and the Sun spot numbers. Taken form Yoshitake et al. (2013).	17
2.12	O_{VII} and O_{VIII} surface brightnesses relation obtained for 14 high-latitude directions observed with Suzaku near the solar minimum (Yoshino et al. (2009)).	18
3.1	The 96 minute <i>Suzaku</i> orbit.	22
3.2	Side view of <i>Suzaku</i> with the internal structures after the EOB deployment. Taken from Mitsuda et al. (2007).	22
3.3	The XIS1 CCD detector put onto a heat sink.	23
3.4	Cross sectional view of the XIS instrument.	24
3.5	Schematic of top view of the XIS instruments.	25

3.6	Comparison of simulated spectra for SNR E0102-72.3 with <i>Suzaku</i> (top left), <i>Chandra</i> (top right) and <i>XMM-Newton</i> (bottom) response functions.	27
3.7	Response of the back-illuminated (BI; red) and front-illuminated (FI; black) XIS sensors to characteristic X-rays from a boric oxide target (Bautz et al. (2004)). Note that the BI device also detects boron-K emission, indicating that it can measure the energy range as low as 180 eV.	28
3.8	Time dependence of the column density for each element for each detector. The dots show the estimated column densities based on observations of a line-dominated supernova remnant (E0102.2-7219, red), a blazer (PKS2155-304, blue) and a a super-soft isolated neutron star (RXJ1856.5-3754, green). The solid black lines are the contamination growth curves modeled with phenomenological functions of time. The stars shows column densities predicted by using the current contamination file (released on August 25th, 2014).	30
4.1	The top panel shows the countrate spectra of RX J1856 obtained with XMM-Newton and Chandra with the best single blackbody model fit to each instrument. The bottom two panels show the ratio between the data and the model for both the CCD detectors and the high resolution grating instruments. . . .	33
4.2	An example of RXJ1856 images of RX05b in different energy bands taken by the XIS1 . The energy ranges are (a) 0-100 eV, (b) 100-150 eV, (c) 150-200 eV and (d) 200-284 eV. The source is clearly detected that above 100 eV. . . .	35
4.3	The count rate for LH07 in the 0.45-0.6 keV as a function of the day earth elevation angle. the observed counting rate (black dots) was compared with an averaged counting rate observed during <i>Suzaku</i> moved around the night earth side, where there is no contamination from the solar scattered X-rays. In this case, We used data acquired when the elevation angle was more than 60 degrees.	37
4.4	Comparison of the data (black, X-ray and non X-ray background is not subtracted), NXB (red), non-corrected XRB (blue) and corrected XRB (green, see text) spectra.	39
4.5	Spectral model best estimated in Beuermann et al. (2006).	42
4.6	Comparison of the observed spectra and folded model in the energy range of 0.17 - 0.8 keV. Note that spectral fitting was not performed for any observation.	43

4.7	Transmission factors assuming the column densities of $1 \times 10^{18} \text{ cm}^{-2}$ for various elements. The top left plot shows a transmission factor for H, C, N and O assuming an approximate column density obtained from the current contamination model (note that the Hydrogen column density is a factor of 1000 higher than the other elements).	44
4.8	RX09b spectral fit results, by replacing H to He, Na, Al, Si, S, Cl and Ar while maintaining carbon, nitrogen and oxygen. The column densities of 4 elements were treated as free parameters when fitting the spectrum.	46
4.9	Spectral fit results with the CNOS contamination model. The best fit parameters are shown in Table 4.5.	48
4.10	Contamination growth curves for C, N, O and S. The details for the fitting functions are presented in Table 4.6.	50
4.11	Comparison of the current HCNO and new CNOS contamination models. .	51
4.12	Calibration results with the new contamination growth curves.	52
4.13	Calibration uncertainties that has to be taken into account in the 200-280 eV (top) and 300-400 eV (bottom) energy ranges, from 2005 to 2014.	53
4.14	Calibration uncertainties that has to be taken into account in the 400-500 eV (top) and 520-590 eV (bottom) energy ranges, from 2005 to 2014.	54
4.15	Residual differences between the HCNO (black) and CNOS (red) contamination models with the E0102 spectra observed in 2005, 2007, 2009 and 2011. A systematic residue above $\sim 1.5 \text{ keV}$ for each data is because spectral fit is not performed, in order to reveal differences between the contamination models.	56
5.1	A trend of the O_{VII} line intensities toward the Lockman Hole observed from 2006 till 2011. Dots with error bars (1σ) show O_{VII} intensities and lines indicate the relative sun spot number (Yoshitake et al. (2013)).	58
5.2	An X-ray image in the 0.1-0.2 keV band for LH09. The vignetting effect is not corrected and the NXB is not subtracted. The areas enclosed by the solid green rectangle and circles was excluded from the data analysis. Point sources (indicated with the two circular regions) are removed form the image. An unusual bright region was detected in the middle of the most left column, or the segment A (indicated as the green rectangular box).	59
5.3	Comparison of the processed data and NXB for LH06-09 (top) and LH10-12 (bottom). The NXB becomes dominant above $\sim 5 \text{ keV}$. The signal-to-noise ratio at the 1/4 keV band (defined as the energy range of 0.17-0.284 keV) is 87 and 39 for LH06-09 and LH10-12, respectively.	61

- 5.4 Comparison of the effective areas from 0.1 to 2 keV for LH06-09 (black) and LH10-12 (red). The effective area for each spectrum was calculated based on the new contamination transmission developed in Chapter 4. 62
- 5.5 Top panel: NXB subtracted spectra of LH06-09 (black) and LH10-12 (red). The energy bin size was determined to meet the minimum photon count of 150 cts for the LH10-12 data (before subtracting the NXB spectrum), Middle: Ratio of the spectra. The observed photon count rate in LH10-12 was simply divided by the one observed in LH06-09 for each bin. The plotted errors were calculated taking into account the error propagation. The ratio of the effective areas is also indicated with a blue solid line. Bottom: H-SWCX model predicted by Koutroumpa et al. (2009) (indicated with 103 black vertical lines) and the folded model by the XIS1 response (indicated with a blue solid line). The intensity is shown in units of LU ($\text{photons cm}^{-2} \text{ s}^{-1} \text{ sr}^{-1}$). 63
- 5.6 Schematic Grotian diagram for a helium-like ion with selected radiative (downward) transitions. Taken from Smith et al. (2014). 65
- 5.7 Temperature dependence of the ACX model in the 0.17-1 keV band. The APEC model with the temperature of 0.1 keV is also plotted (magenta) for comparison. The flux for each model is adjusted to be roughly matched each other around the O_{VII} emission line. 66
- 5.8 68 % (red) and 90 % (green) confidence contours of the LB temperature vs. the ISM temperature for the LB SXDB model given in Table 5.2. 68
- 5.9 Spectral fit result of the LH06-09 spectrum. Top panel: The NXB subtracted data is shown as the black crossed points and best fit curve folded by the detector response is indicated with a black solid line in Table 5.2. The LB, galactic halo and CXB components with the best fit parameters (Table 5.2) are indicated with blue, green and red solid lines respectively. Bottom panel: Residual plot defined as the data minus best fit model. 69
- 5.10 Spectral fit result of the LH06-09 spectrum. Top panel: The NXB subtracted data is shown as the black crossed points and the best fit curve folded by the detector response is indicated with a black solid line. The H-SWCX (ACX model), Galactic halo and CXB components with the best fit parameters (Table 5.3) are indicated with magenta, green and red solid lines, respectively. Bottom panel: Residual plot defined as the data minus best fit model. 70
- 5.11 Same as Fig. 5.10 but the ISM temperature is fixed at the best fit values of 0.177 keV obtained from the spectral fit with the LB model (presented in Table 5.2). The temperature of the ACX model is a free parameter. 71

5.12	The LH10-12 spectrum along with the base model (Table 5.2) folded by the XIS1 response for LH10-12. A clear enhancement can be seen below 1 keV.	72
5.13	The SWCX-contributed spectrum along with the ACX model (solid red line). The black solid line indicates the LB model derived from the LH06-09 spectrum.	73
5.14	A typical spectral fit result to the mock spectrum produced from the 103 H-SWCX induced emission lines taken from Koutroumpa et al. (2009). The solid red lines indicate the Gaussian models whose width were fixed at zero but the line center energies and normalizations were free. 9 Gaussian lines well reproduced the mock spectrum created by assuming the typical exposure time of 200 ksec.	75
5.15	Spectral fit to the SWCX-contributed emission with the Gaussian line model described in Table 5.4. The black solid line indicates the LB model derived from the LH06-09 spectrum.	77
5.16	Comparison of the intensity for each emission line between the observation and the Gaussian H-SWCX model. The intensities are normalized by the ones for $O_{VII} K\alpha$ located at 567 eV. The error bars indicate 90 % statistical error range (The error for the $O_{VII} K\alpha$ is propagated to calculate the errors for line ratios).	78
5.17	Spectral fit to the LH06-09 spectrum, adding a Gaussian model (thick orange line) to the LB SXDB model presented in Fig. 5.9.	82
5.18	Comparison of the intensity for each emission line between the observation and the Gaussian H-SWCX model without Mg contributions. The intensities are normalized by the ones for $O_{VII} K\alpha$ located at 567 eV. The error bars indicate 90 % statistical error range (The error for the $O_{VII} K\alpha$ is propagated to calculate the errors for line ratios).	84
5.19	Pictures taken from Lallement et al. (2003), showing iso equivalent width contours for 20 mÅ and 50 mÅ, and cut in the 3D volumic density obtained from the global inversion of the column densities. The density map is cut out along with the cross section of 150°-330°. The line-of-sight (LOS) toward the Lockman hole is indicated with a blue line. A red solid line indicates the distance from the Sun to the LB boundary ($W = 50$ mÅ). From the figure, the distance can be read about 230 pc.	85

5.20	68 % (red), 90 % (green) and 99 % (blue) confidence contours of the LB temperature vs. normalization. The broken lines indicate the relation $kT \times \text{norm} = \text{const.}$ that were used to estimate the upper and lower values of the 90 % statistical errors for the LB pressure. Note that the norm here is an Xspec normalization, not the emission measure integrated over the line of sight.	87
A.1	Net count rate in 0.45-0.6 keV as a function of the <i>DYE_EL</i> V angle. The results for RX05b to RX10b are presented.	99
A.2	Net count rate in 0.45-0.6 keV as a function of the <i>DYE_EL</i> V angle. The results for RX11b to RX14b are presented.	100
A.3	Net count rate in 0.45-0.6 keV as a function of the <i>DYE_EL</i> V angle. The results for LH06 to LH12 are presented.	101
B.1	Histograms of the best fit parameters of the energy center and intensity for each line, obtained by fitting 1000 mock H-SWCX spectra with the zero-width Gaussian model.	104
B.2	Continue from Fig. B.1	105
B.3	Continue from Fig. B.1	106

List of tables

3.1	Overview of <i>Suzaku</i> capabilities related to the XIS instruments.	25
3.2	Error Budgets of Scientific Instrument Calibrations, given by the XIS team.	26
4.1	The best fit parameters to the RXJ1856 spectrum with the two-temperature blackbody radiation model determined by Beuermann et al. (2006).	32
4.2	Suzaku RXJ1856 observation log. The nominal exposure is the exposure time left after the standard data processing. The usable exposure means the exposure time after further data screening applied.	34
4.3	X-ray counting rate for each energy band for the observation RX05b.	40
4.4	Parameter details of the spectral model as a reference. The spectral model is expressed as $tbvarabs(bbodyrad + bbodyrad)$ in XSPEC.	41
4.5	Spectral fit results with the CNOS contamination model.	47
4.6	Fitting curve models and best fit parameters for each element.	50
5.1	<i>Suzaku</i> Observation log of the Lockman hole from 2006 until 2012. The nominal exposure is the exposure time left after the standard data processing. The usable exposure means the exposure time left after further data screening applied.	60
5.2	Spectral fit result of the LH06-09 spectrum with the LB model.	67
5.3	Spectral fit result of the LH06-09 spectrum with the ACX model.	70
5.4	Spectral fit result with the simulated Gaussian model based on the H-SWCX emission lines calculated by Koutroumpa et al. (2009). The predicted emission lines for the 219, 267 and 362 eV give an idea of what sort of ions contribute to those lines.	76
5.5	Summary of the systematic uncertainties investigated for the temperature and normalization obtained with spectral fit to the LH06-09 spectrum.	80
5.6	Spectral fit result of the LH06-09 spectrum with the LB model.	82

A.1	Summary of the data screening threshold for the day Earth elevation angle (<i>DYE_ELV</i>).	98
-----	--	----

Chapter 1

Introduction

Soft X-ray Diffuse Background (SXDB) is truly diffuse emission that contributes significantly to the X-ray background sky below 2 keV. From the observations using the X-ray focusing optics and the X-ray CCD camera onboard Suzaku, XMM-Newton and Chandra observatories after 2000, the SXDB is now considered to consist of at least three different emission components; (1) the emission from the Heliosphere by the charge exchange interaction of the solar wind and neutrals in the planetary space (SWCX), (2) the emission from the ~ 1 MK hot plasma in the so-called local bubble, which is a cavity surrounding the solar system (LB), (3) the emission from the ~ 2 MK hot plasma in the halo of our Galaxy (e.g. Yoshino et al. (2009) and Henley and Shelton (2013)). However, in previous observations, the first two components, the SWCX (the solar wind charge exchange) and the LB (Local Bubble), could not be separated well from each other in the X-ray spectra. In most cases, the sum of the two components were represented with a single thermal-emission model. However, there is clear evidence for the existences of both components.

The LB was first suggested from the sounding rocket experiments in late 1960's (Tanaka and Bleeker (1977)). Those rocket experiments extensively studied a large-scale spatial variations in intensity of the emission in ~ 0.1 to ~ 0.3 keV band, which is often called the 1/4 keV band or C band. They found that the intensity in the C band shows an anti-correlation with the total line-of-sight column density of the neutral interstellar medium (ISM) of our Galaxy. However, the anti-correlation is clearly not due to the X-ray absorption of the ISM because the hardness ratio of the emission, e.g. 0.1-0.2 keV to 0.2-0.3 keV intensity ratio is constant (e.g. McCammon and Sanders (1990)). Those results were interpreted by a displacement model of the hot gas in a cavity. Namely, the solar system is surrounded by a cavity where neutral ISM density is low and replaced with a hot gas of a temperature of ~ 1 MK. The line-of-sight length of the cavity depends on the direction and in the direction with longer sight length, the total Galactic neutral ISM column density is low. This model

was supported by the 1/4 keV band observations of the ROSAT observatory in 1990's. The existence of the cavity is supported by NaI absorption-line observations of the background stars. Lallement et al. (2003) combined the NaI absorption data with the star-distance data by Hipparchus and created a 3D map of the cavity. The cavity is extended with about 100 pc length scales depending on directions.

We recognized the importance of the SWCX after the discovery of the X-ray emission from comets (e.g. Lisse et al. (1996)). XMM-Newton, and Chandra observations clearly detected temporal variation of O_{VII} emission at ~ 0.57 keV in the X-ray background. Moreover, Yoshitake et al. (2013) discovered using the Suzaku observations, a long-term increase of the O_{VII} emission intensity correlated with the 11-year solar activity. Given the chemical composition and their ionization states in the solar wind, the SWCX emission must contain emission in the 1/4 keV band.

Since the early phase of the investigation, a pressure problem of the LB has been suggested (e.g. Tanaka and Bleeker (1977)). Namely the pressure of the hot gas in the LB far exceeds the thermal pressure of the ISM, thus the LB cannot be in dynamical equilibrium. Snowden et al. (2014) recently proposed a solution; by including the SWCX in the SXDB, the pressure of the LB hot gas decreases. Although the reduced hot gas pressure is still higher than the thermal pressure of the ISM, it can balance with the sum of the thermal pressure of the ISM and magnetic fields. They thus suggested that if the supernova explosion that created the cavity swept out the magnetic fields there, the pressure balance problem can be solved.

In the previous Suzaku observations, the energy band used for the analysis was limited to above 0.4 or 0.5 keV, excluding below 0.3 KeV because of the uncertainty in the detection efficiency of the detector system. Above 0.4 or 0.5 keV, both LB and SWCX emission spectrum can be approximated with a single O_{VII} emission line, and the emission spectrum can be modeled with a single 1 MK thermal emission model. Both XMM-newton and Chandra were also not suited for spectroscopy below 0.5 keV.

We consider that the spectroscopy including the 1/4 keV band is the key to deepen our understanding of the SXDB, especially in terms of the LB and the SWCX. For that purpose we re-visited the detection efficiency calibration of the X-ray camera onboard Suzaku. Soon after the commissioning operation of the CCD camera, accumulation of contaminants on the optical blocking filters was noticed. The absorption of X-ray by the contaminants was calibrated onboard by using calibration targets. However, the degradation of the efficiency below ~ 0.4 keV was not reproduced well.

In this thesis, we for the first time enables quantitative spectral analysis for the SXDB in 0.17-2.0 keV and investigate the origin of the local diffuse emission. The core of our research is the XIS1 CCD instrument on-board the Suzaku observatory. We first try to

calibrate the detection efficiency in all energy bands including the 1/4 keV band by using the data biannually taken from 2005 to 2014 for the neutron star RXJ1856.5-3745. Then, we study the SXDB using observations of the Lockman hole field from 2006 to 2012, covering the period from the solar activity minimum to maximum. It is known in this field that the O_{VII} line intensity is enhanced during the solar maximum period. This characteristic is useful to separate the H-SWCX emission from others because only the H-SWCX emission is considered to be the time variable component in the SXDB. This thesis is organized in the following manner. In Chapter 2, we present a brief history of the SXDB study together with remarkable observational facts and what have been the subjects of controversy. We then introduce the Suzaku CCD instrument (XIS1) that is a core of our research. We explain the advantage of this instrument and provide some technical aspects in Chapter 3. Our main research results are presented in Chapters 4 and 5. We start with an instrument calibration focussing on the quantum efficiency in the 1/4 keV band, that varies with time due to the contamination accumulation onto the instrument in orbit. We then show our spectral fit results for the SXDB in 0.17-2 keV toward the Lockman Hole field. We examine the origin of the local diffuse emission and characteristic of the LB and H-SWCX emission. we also estimate the pressure of the LB and compared with the previous results. We lastly conclude our research findings throughout this dissertation in Chapter 6.

All error ranges quoted in text are for 90 % confidence level unless otherwise noted, while vertical bars in figures show 1σ errors. Throughout this thesis, we use Asplund et al. (2009) abundances as a nominal solar abundance table.

Chapter 2

A Review

2.1 Brief History of the Soft X-ray Diffuse Background below 1 keV

X-rays from an extra-solar object were first discovered in 1962 by Giacconi et al. (1962) using a sounding rocket experiment with Geiger counters sensitive to 2-6 keV. In the same experiment they also found the X-ray background emission, namely X-rays coming from all the directions of the sky the rocket payload had scanned. This emission is now known as the cosmic X-ray background (CXB), which has been studied extensively in a wide energy band from about 2 keV to a few hundred keV. Soon after this discovery, the observation below 1 keV started with sounding rocket (Bowyer et al. (1968)) and it was already noted that the surface brightness below 1 keV far exceeds the extrapolation of the flux above 1 keV after correcting for the absorption by the neutral interstellar medium in our Galaxy (Henry et al. (1968)). As reviewed in the next section, the CXB above 2 keV is considered to be resolved into faint individual sources. On the other hand, the excess emission below 1 keV over the CXB is considered to be spatially diffuse in nature. Thus it is often called the soft X-ray diffuse background (SXDB).

The SXDB was extensively studied with a series of sounding rocket experiments, e.g. Nagoya and Nagoya-Leiden sounding rocket experiments. The most important finding of those experiments is the concept of the local bubble (LB) ¹, in which the solar system is surrounded by a ~ 1 MK hot plasma extending 100 pc scales (Tanaka and Bleeker (1977)). The Wisconsin sounding rocket experiments conducted all sky observations (McCammon and Sanders (1990)). Then the *ROSAT* observatory in orbit conducted all sky observations

¹ Although in those papers, the wording, local hot bubble (LHB) was used, here we use the wording presently used.

in 1994-1997. From those observations we recognized the emission beyond the bulk of the absorption of our Galaxy. Then the discovery of X-ray emission from the comet Hyakutake by *ROSAT* (Lisse et al. (1996)) brought a new insight into the origin of the SDXB, namely the solar wind charge exchange induced X-ray emission (SWCX). Soon after the discovery, it was suggested that a significant fraction of the SXDB can be explained with the SWCX with the interplanetary neutrals in the Heliosphere (Cox (1998)). Although the existence of the LB is still required from a number of observations in various wavelengths (section 2.3.1), and the so-called displacement model (section 2.3.1) strongly suggests the significant contribution of the LB to the SWCX is now thought to be a dominant component of the SXDB Yoshino et al. (2009).

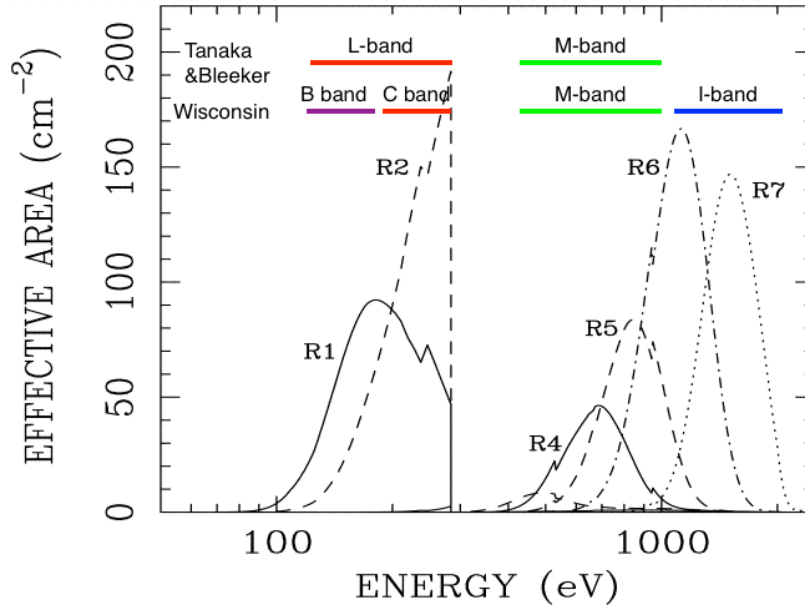


Fig. 2.1 The band response function of the *ROSAT* position sensitive proportional counter with definitions of the energy bands. B-band, C-band, M-band and I-band for the Wisconsin sound rocket experiment are marked over the plot. L-band and M-band for Tanaka and Bleeker (1977) are also indicated.

Until the *ROSAT* era, the SXDB was studied with the band spectroscopy with $E/\Delta E \sim 1$; the surface brightness was studied in three or four energy bands given in Fig. 2.1. There is an energy gap in 0.3-0.4 keV because of the X-ray absorption of the carbon K edge at the window of the X-ray instruments. The *ROSAT* R1+R2 band is often called the 1/4 keV band (the R4+R5 band is called 3/4 keV band). We use this terminology in this thesis as well, when referring to the energy range below the carbon edge. In 2002, emission lines from the SXDB were clearly resolved for the first time with sounding rocket experiments using an X-ray microcalorimeter (McCammon et al. (2002a)). However, the extensive spectral studies of the

SXDB were conducted with the CCD instruments onboard three large observatories, *Chandra* (1999-), *XMM-Newton* (1999-), and *Suzaku* (2005-2014). These instruments enabled an energy spectroscopy with $E/\Delta E \sim 10$. O_{VII} (570 eV) and O_{VIII} (653 eV) were clearly resolved, deepening the understanding of the SWCX and the Galactic halo emission from the observations of the absolute line intensities and ratios. On the other hand, 1/4 keV band has been somewhat "forgotten" in the CCD instrument era. *Chandra* and *XMM-Newton* cannot observe below ~ 0.35 keV due to their high/unstable instrumental background and poor detector responses represented as a spectral tail on the low energy side (see Fig. 2.2). *Suzaku* has a better energy resolution, a stable background, and ideal detector responses but the quantum efficiency at the low energy band had been rapidly degraded due to the contamination accumulated in orbit. The 1/4 keV band has been crucial for studying the LB and the SWCX emission but not yet researched with the modern CCD instruments.

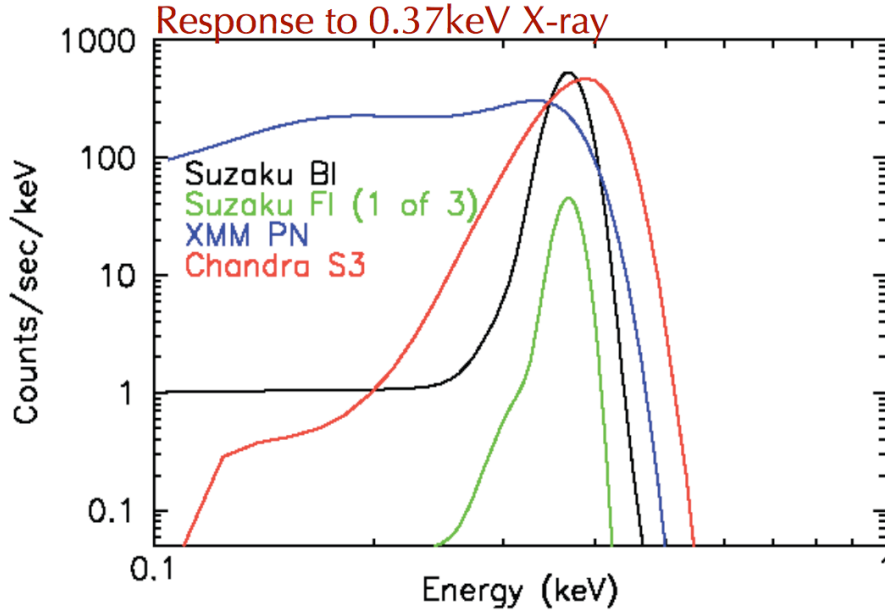


Fig. 2.2 Comparison of the instrumental response functions to the monochromatic 0.37 keV X-ray for *Chandra* (red), *XMM-Newton* (blue) and *Suzaku* (black and green).

The main focus of this thesis is the SXDB. However, for the study, we need to understand the nature of the CXB above 2 keV, because the faint sources that contribute to this energy band should also contribute to the flux below 1 keV. We thus briefly review the CXB above 2 keV in the next section. Then we will review the present understanding of the SXDB in the following sections.

2.2 Spectrum, Intensity, and Origins of the CXB above 2 keV

2.2.1 Spectrum of the CXB above 2 keV

In Fig.2.3 the CXB spectra measured by different instruments are shown Revnivtsev et al. (2003). The intensity of the CXB depends on flux of point sources that can be removed from the field of view. The threshold of those plots are different but all the measurements indicate surface brightness of $1 \times 10^{-12} \text{ erg s}^{-1} \text{ cm}^{-2} \text{ deg}^{-2}$ in the 2-10 keV band.

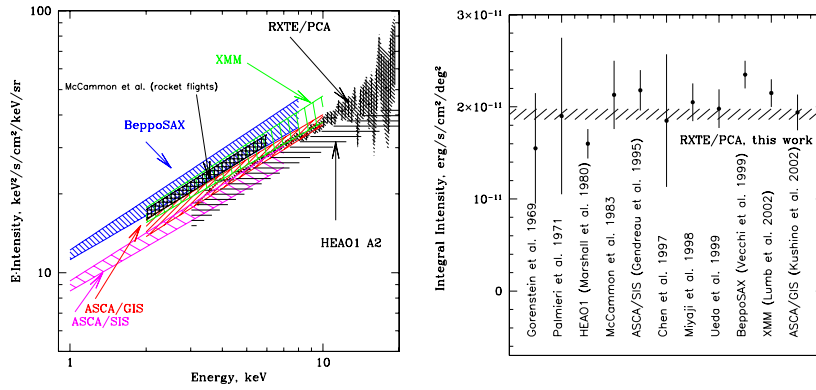


Fig. 2.3 X-ray background spectra (photon spectrum $\times E^2$, presented in the right figure) and the intensity in 2-10 keV band obtained with different instruments is shown in the left figure. Taken from Revnivtsev et al. (2003).

The CXB spectra in the energy band shown in the figure can be represented with a single power-law function

$$\frac{dN(E)}{dE} = NE^{-\Gamma}, \quad (2.1)$$

after correcting for the Galactic absorption. All previous studies show similar photon index (Γ) about 1.4 (eg. Kushino et al. (2002), Revnivtsev et al. (2003)).

In the higher energy range (Fig.2.4), the spectrum shows an exponential cut-off and the spectrum can be represented with a function,

$$\frac{dN(E)}{dE} = NE^{-\Gamma} \exp(-E/E_c), \quad (2.2)$$

where the e-folding energy, E_c , is about 40 keV (Boldt (1992)).

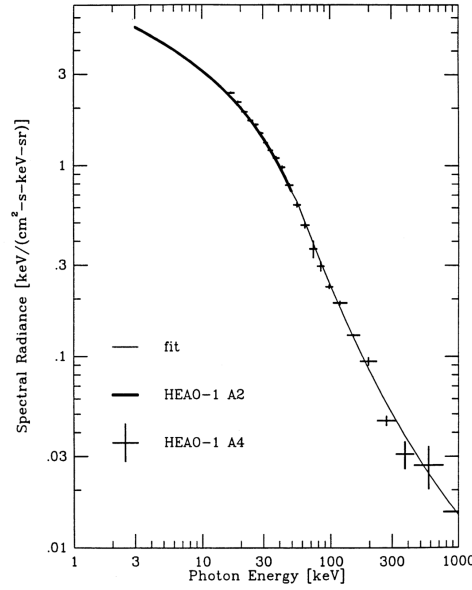


Fig. 2.4 X-ray background spectra from 3 keV to 1 MeV observed with the HEAO-1 observatory. Taken from Boldt (1992).

2.2.2 Resolving the CXB into Point Sources

Unresolved faint X-ray sources, if they exist, can contribute to a certain fraction of the X-ray background therefore, by observing with instruments with higher sensitivity and higher spatial resolution, we may be able to resolve these into individual sources. Many point source surveys have been conducted so far with this purpose (e.g. McCammon et al. (2002b)). The most recent, and the highest-sensitivity survey was conducted with the *Chandra* observatory toward the Chandra Deep Field (CDF). The flux limit of the survey was $\sim 1 \times 10^{-18} \text{ erg s}^{-1} \text{ cm}^{-2}$. In total, 1008 X-ray sources were detected in this field of view of 484 arcmin^2 , for the CDF-South (Luo et al. (2016)). Most of them are considered to be active galactic nucleus (AGNs) but the faint class contains galaxies. From the $\log N - \log S$ (the relation between the number X-ray sources (N) brighter than a given flux (S)) plot of the point sources, they concluded that $93 \pm 11\%$ of the CXB in the 2-10 keV band is already resolved into the point sources.

The average spectrum of bright AGNs in local universe has a power-law index of ~ 1.8 in 2-10 keV band, steeper than that of the CXB. This difference is explained by the existence of heavily absorbed AGNs, which have a significantly hard spectrum in 2-10 keV, and show a broad peak structure called a Compton bump at about 20 keV. By combination of un-absorbed and absorbed AGN spectra, the CXB spectrum can be explained successfully, e.g. see Gilli et al. (2007).

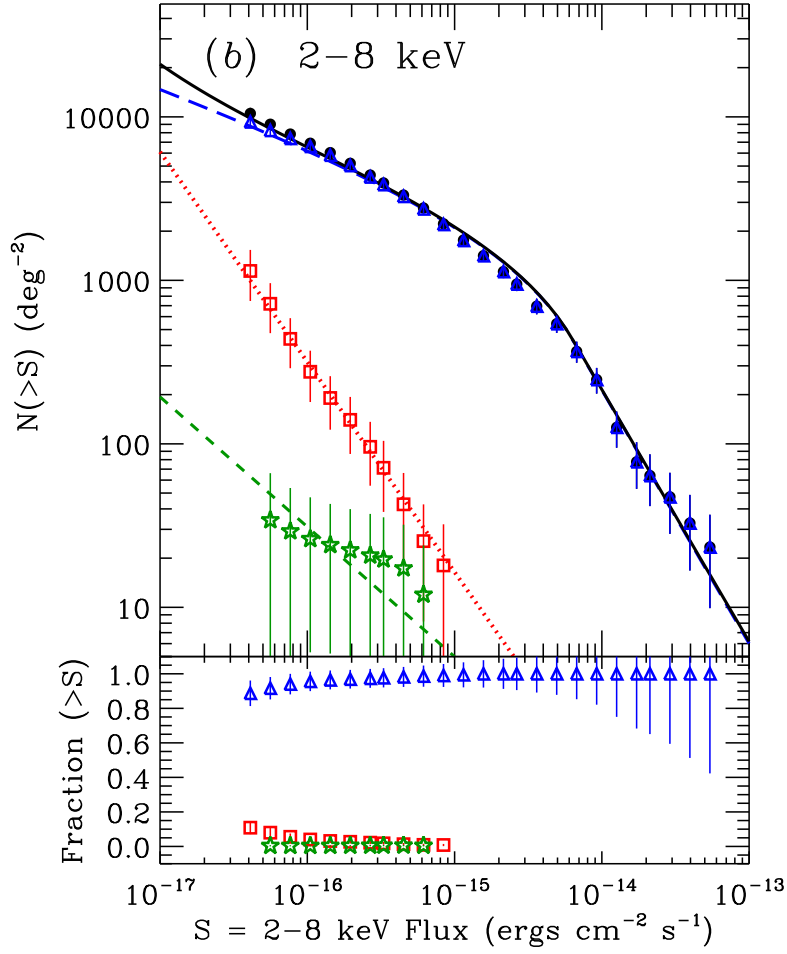


Fig. 2.5 $\log N - \log S$ plot of the CXB in the 2-8 keV band obtained with Chandra. Contribution of object types are shown with different colors and marks: AGN (blue triangles), galaxies (red rectangles), and stars (green stars) (Lehmer et al. (2012)).

2.3 Spectrum, Intensity, and the Origins of the SXDB

As shown in the previous section, about 90 % of the CXB in 2-10 keV has been resolved into individual point sources. On the other hand, McCammon et al. (2002b) suggested that the CXB contributes to the flux in the ROSAT R4 band about 38 %, derived from the comparison of the ROSAT flux and the X-ray spectrum obtained with the XQC X-ray microcalorimeter experiment. They also placed 42 % for the thermal origin from the OVII and OVIII emission lines. Although these lines are clearly resolved in the spectrum, those estimates contain large uncertainties, because a certain fraction of OVII emission line must arise from non-thermal process, SWCX, and we do not know the exact fraction yet.

In this section, we review the studies of the origins of thermal and SWCX induced X-rays in the SXDB. In the next section, we will review the studies of emission with unknown origins.

2.3.1 The SXDB in the 1/4 keV Band and the Local Bubble (LB)

The photo-electric absorption coefficient is proportional to $\sim E^{-7/2}$ when the X-ray photon energy E is much higher than the absorption edge energy of the absorbing atoms. Therefore the absorption coefficient is larger for softer X-ray photons. X-ray photons below 0.3 keV cannot travel through the Galactic neutral-hydrogen column density of $1 \times 10^{21} \text{ cm}^{-2}$ with the solar elemental composition.

The C-band (0.2-0.3 keV) intensity of the SXDB is plotted as a function of the total Galactic column density in the top panel of Fig.2.6. The C-band intensity decreases with increasing column density. However, the intensity ratio of the B-band (0.1 - 0.2 keV) to the C-band is constant (bottom panel of Fig.2.6). This is not consistent with the photo-electric absorption scenario (the broken line), suggesting that a large fraction of the SXDB is originated in something else. This is normally explained by the displacement model, in which the solar system is considered to be surrounded by a hot plasma and the line of sight length of the hot plasma is anti-correlated with the total column density of Galactic neutral medium. The region filled by the hot plasma is called the local bubble (LB).

Existence of unabsorbed emission is supported by shadowing observations. Fig.2.7 shows an example and for the molecular cloud MBM-12 located at the distance of about 100 pc. The X-ray intensities of three energy bands are plotted as a function of $100 \mu\text{m}$ far infrared intensity (I_{100}). It is known that I_{100} is well correlated with N_{H} ; $(N_{\text{H}}/10^{20} \text{ cm}^{-2}) = 1.4I_{100}(\text{MJy sr}^{-1}) + 0.15$. From the figure we find that a large fraction of the X-ray background in R45 and R67 bands comes from regions behind MBM-12, while that of R12 band come from the near side of MBM-12. Thus the depth of the local bubble must be smaller than 100 pc.

Existence of a cavity around the solar system is supported by observations in other wavelengths. Lallement et al. (2003) (Fig.2.8) used NaI absorption lines in spectra of ~ 900 stars within ~ 300 pc whose distance is accurately determined with the Hipparcos satellite. The differential absorption strength of a direction gives a density of neutral medium. They show that the solar system is inside a cavity with a 50-150 pc scale. Lallement et al. (2014) applied the same method to E(B-V) of those stars and obtained the similar results.

The potential problem of the LB is its high pressure which was already pointed out by Tanaka and Bleeker (1977). The interstellar pressure at the solar neighborhood can be estimated from the density profile of the interstellar medium (ISM) and the gravitational

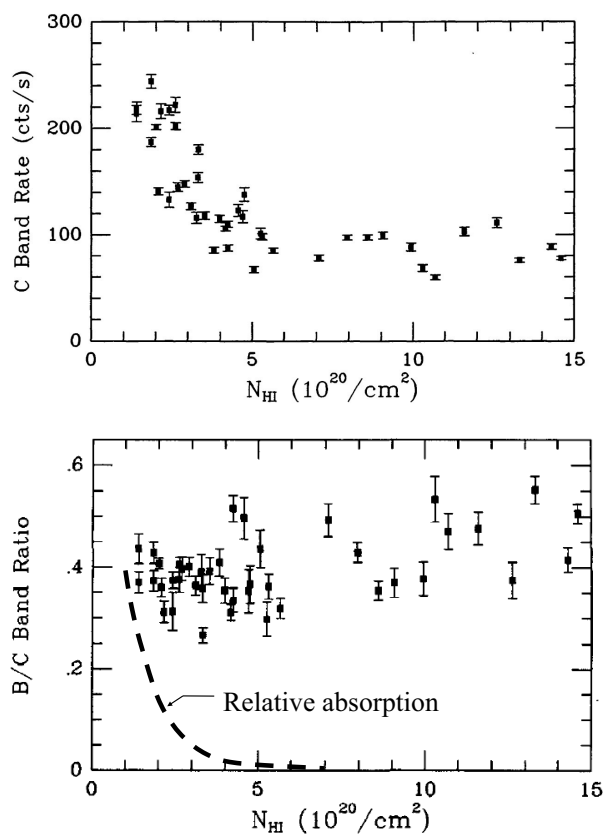


Fig. 2.6 Top: C band (~ 0.2 - 0.3 keV) counting rate obtained with the Wisconsin sounding rocket all sky survey plotted as a function of total Galactic Hydrogen column density of the direction (N_{H}). Bottom: B-band (~ 0.1 - 0.2 keV) to C-band count rate ratio plotted as a function of N_{H} . The ratio of the transmissions of N_{H} in B to C bands is plotted with a dashed line, which is very different from the observation. Thus, although the C band intensity shows anti-correlation with N_{H} , it can not be due to the Galactic absorption. Figures are taken from McCammon and Sanders (1990).

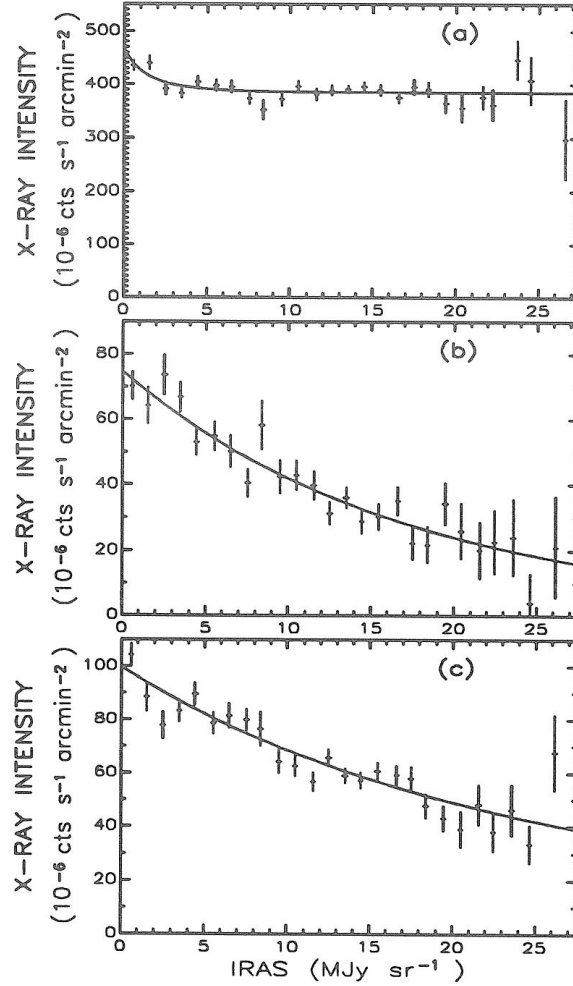


Fig. 2.7 ROSAT counting rates in the directions of the MBM-12 molecular cloud ($D \sim 100$ pc) plotted as functions of $100 \mu\text{m}$ far infrared intensity (I_{100}) (Snowden et al. (1993)). Three panels show different energy bands, ROSAT R12 (1/4 keV) band, R45 (3/4 keV band), and R67 (1.5 keV) band. The $100 \mu\text{m}$ intensity is known to show correlation with the total (atomic + molecule + dust) H column density of the direction; $(N_{\text{H}}/10^{20} \text{ cm}^{-2}) = 1.4I_{100}(\text{MJy sr}^{-1}) + 0.15$.

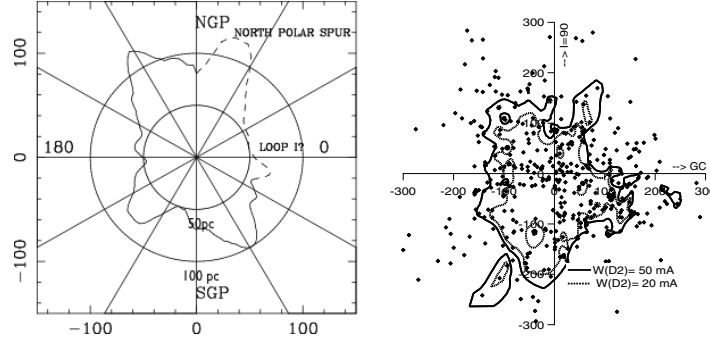


Fig. 2.8 Spatial extension of the LB estimated from the ROSAT 1/4 keV band observation (left) and spatial extension of local cavity estimated from for Na_I Fraunhofer D1 and D2 absorption lines of local ~ 900 stars whose distances were determined by the Hipparcos satellite. Figures are taken from Snowden et al. (1998) and Lallement et al. (2003).

potential of the Galaxy assuming hydrostatic equilibrium. In Fig.2.9 we show the pressure profile along the direction vertical to the Galactic plane, together with the pressure of the ISM. The total pressure is an order of magnitude higher than the ISM pressure. The rest of the pressure is considered to be supported by three pressure components; the magnetic field, the cosmic ray, and the bulk motion. The pressure of the LB does not fit in this picture because its pressure is estimated to be $p/k_B = 1.7 \times 10^4 \text{ cm}^{-3} \text{ K}$. Because of the high pressure, Tanaka and Bleeker (1977) argued that the LB was not in the pressure balance and expanding rapidly, and that the LB will flow out from the galactic plane.

In the next subsection we will discuss that a significant fraction the SXDB in 1/4 keV band must also arise from SWCX in the Heliosphere. Snowden et al. (2014) argued that after removing the contribution of the SWCX, which is calculated based on a certain emission model, from the SXDB spectrum, the pressure of the LB is estimated to be $p/k_B = 1.0 \times 10^4 \text{ cm}^{-3} \text{ K}$. They suggested that the LB can be in pressure balance if the supernova explosion created the LB sweeping both the magnetic field and the cold ISM outside the LB.

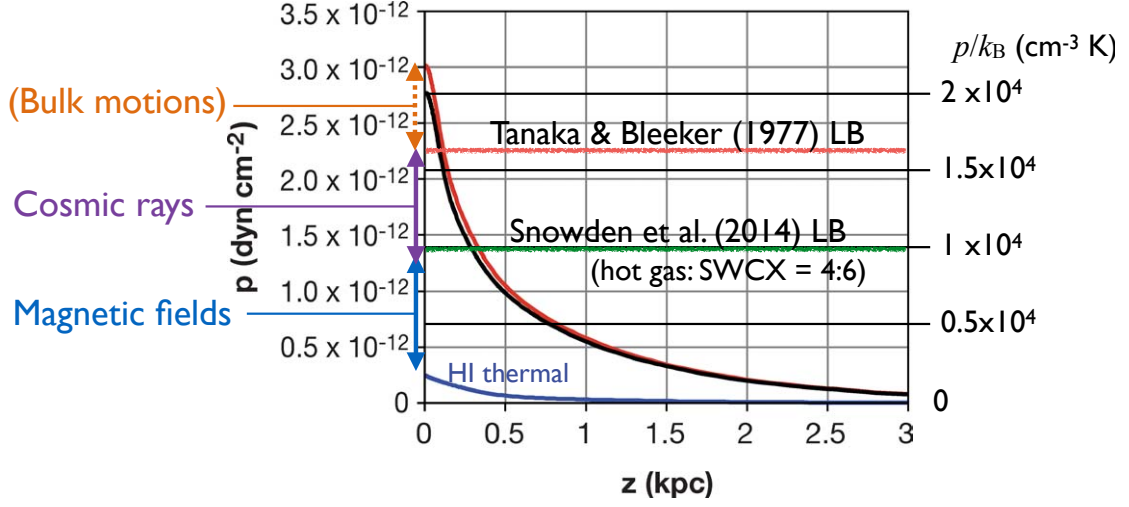
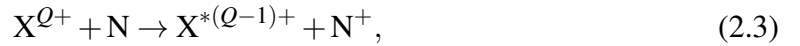


Fig. 2.9 ISM pressure as a function of vertical distance from the Galactic plane at the solar neighborhood. Original figure was taken from Cox (2005), and annotations are added. The two horizontal lines (orange and green) show the LB pressures from the literature. The total pressure at the mid plane is explained by a sum of four pressure components shown in the figure.

2.3.2 Heliospheric SWCX

The importance of charge exchange was recognized by the discovery of X-ray emission from the comet Hyakutake. The X-ray intensity of the comet cannot be explained by the reflection of the solar X-rays. The only explanation was the charge exchange processes between highly-charged ions in solar wind and the neutrals in the vicinities of the comet (CO and etc.). This charge exchange process is written as



where X^{Q+} , N , and $h\nu$ are an ion in the solar wind, neutral in the comet, and the X-ray photon emitted respectively. The asterisk, “*”, represents an excitation state. The SWCX emission arises not only from the vicinity of the comets, but also from the low-density neutral matter surrounding the Earth, named geocorona, and the neutrals in the interplanetary space. Emission from this process consists of only lines without continuum.

Usually the SWCX emission from geocorona (G-SWCX through out this thesis) shows time variations on relatively short timescale (from a few tens of minutes to a few hours)

correlating with the solar wind proton flux that is monitored near the earth. Thus, G-SWCX can be removed from the SXDB observational data (Fujimoto et al. (2007)).

Cox (1998) suggested the most of the X-ray background below 0.5 keV could be explained by the Heliospheric SWCX emission originated within ~ 100 AU from the Sun (called hereafter H-SWCX). An intensity of the charge exchange induced emission along the line of sight (LOS) from observers is expressed as

$$I = \frac{1}{4\pi} \int_0^\infty y_{if} N_{X^{Q+}}(l) v_{\text{rel}} \sigma_{(N, X^{Q+})} n_N(l) dl \quad \text{photons s}^{-1} \text{ cm}^{-2} \text{ Sr}^{-1}, \quad (2.5)$$

where $N_{X^{Q+}}$ and n_N are ion and neutral number densities, v_{rel} and $\sigma_{(N, X^{Q+})}$ are relative velocity and cross section of collision between the ions and neutral atoms, and y_{if} is the photon yield of the interesting transition of the state $i \rightarrow f$ respectively.² We use the unit of photons s⁻¹ cm⁻² Sr⁻¹ as line unit (L.U.) in this thesis. The solar wind travels roughly a quarter AU per day. Thus, the H-SWCX emission we observe is an integral of the solar wind conditions over the previous year, indicating that the time scale of the variation of the H-SWCX emission is an order of a year, much longer than that of the G-SWCX emission. Therefore, contamination from the H-SWCX emission is difficult to be identified and removed from observations of celestial sources.

Numerous efforts have been taken in the past decades for spectral modeling of the H-SWCX emission. Figure 2.10 shows the H-SWCX emission calculated by Koutroumpa et al. (2009). The bulk of the emission composed with various ion species below 0.4 keV. However, spectroscopic analyses in this energy band has not yet been done because of the lack of the sensitivity in CCDs onboard the currently operating missions: *Chandra* and *XMM-Newton* cannot measure this energy range because of their high/unstable background and a large spectral tail on the low energy side of the response. *Suzaku* showed an excellent performance in this energy range but it was quickly lost since contamination was accumulated onto the instrument. The O_{VII} K emission line is known to consist of triplet fine structure lines. If we can resolve those triplets, we can infer the origin of the line from the ratio of the triplets, since the SWCX line should have a higher forbidden to resonant line ratio. However, with the CCD energy resolution, there is no way to distinguish the origin except for time variations. Yoshitake et al. (2013) analyzed the annual *Suzaku* observations of the Lockman hole direction from 2006 to 2011, and found that the O_{VII} intensity in 2010 and 2011 was significantly larger than that of 2006-2009 (Fig.2.11). They argued that the increase is associated with the increase of solar activity indicated by the sunspot number. At least the increased part of the O_{VII} intensity likely comes from the Heliospheric SWCX.

²Note that the energy dependence of the charge exchange reaction is ignored for simplification.

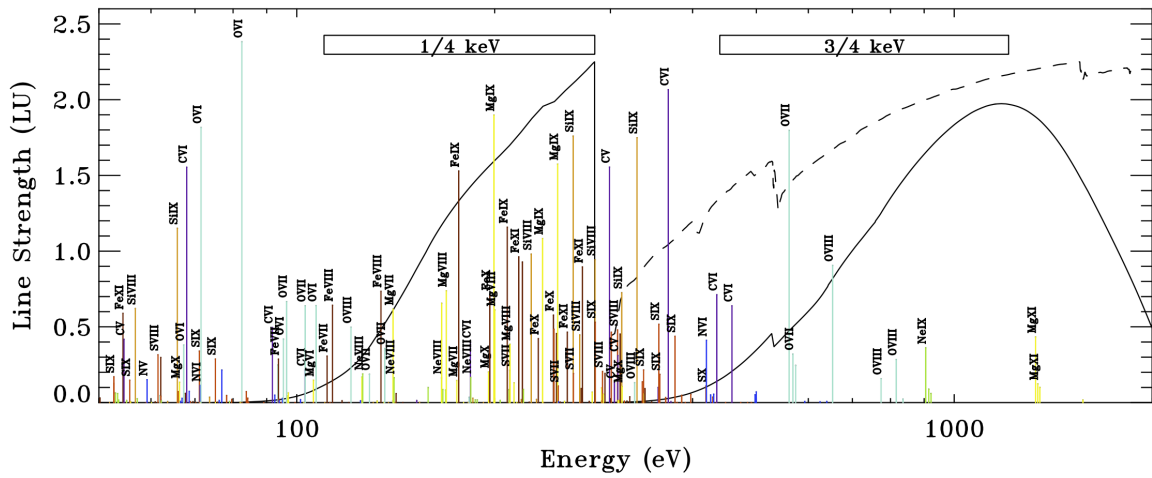


Fig. 2.10 The spectrum of SWCX emission calculated by Koutroumpa et al. (2009) (Figure is taken from Kuntz (2019)). This spectrum was compiled from various theoretical calculations of cross sections and using carefully selected solar wind abundances. However, note that there are still significant uncertainties left in line intensities and ratios. The bulk of the emission is in the 1/4 keV band and is composed of many lines from various species and ionization states. The 3/4 keV band is, on the other hand, contributed by a few lines.

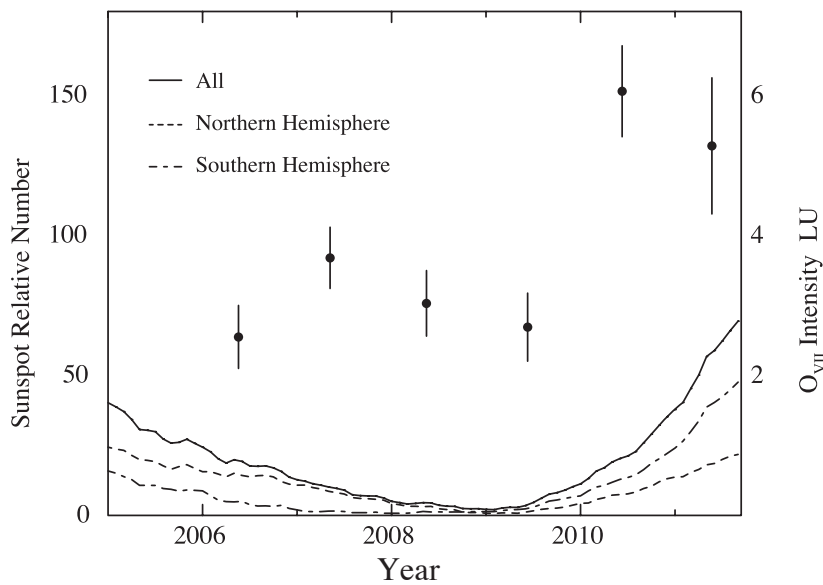


Fig. 2.11 Long-term variation of the O_{VII} intensity toward the Lckman hole direction obtained with the Suzaku observation and the Sun spot numbers. Taken from Yoshitake et al. (2013).

2.3.3 Hot Gas in the Halo of our Galaxy

Shadowing observations, by using absorbing interstellar clouds which blocks X-rays from distant sources, suggest that a significant fraction of ROSAT R45 band comes from 100 pc or more distant places and subject to the absorption of the neutral ISM.

Yoshino et al. (2009) analyzed the *Suzaku* observations of 14 high-latitude blank-sky directions performed near the solar minimum period and found correlations between the O_{VII} and O_{VIII} intensities:

$$O_{VII} \text{ intensity} = 0.5 \times (O_{VIII} \text{ intensity} - 2 [\text{LU}]) \quad (2.6)$$

They discussed that the offset intensity of O_{VII} arises from the Heliospheric SWCX and the LB, while the excess O_{VII} (2–7 LU) is emission from more distant parts of the galaxy. If we assume collisional ionization equilibrium plasma, the temperature is estimated from the O_{VII} to O_{VIII} ratio to be $kT = 0.2$ keV (corresponding to $\log T = 6.37$).

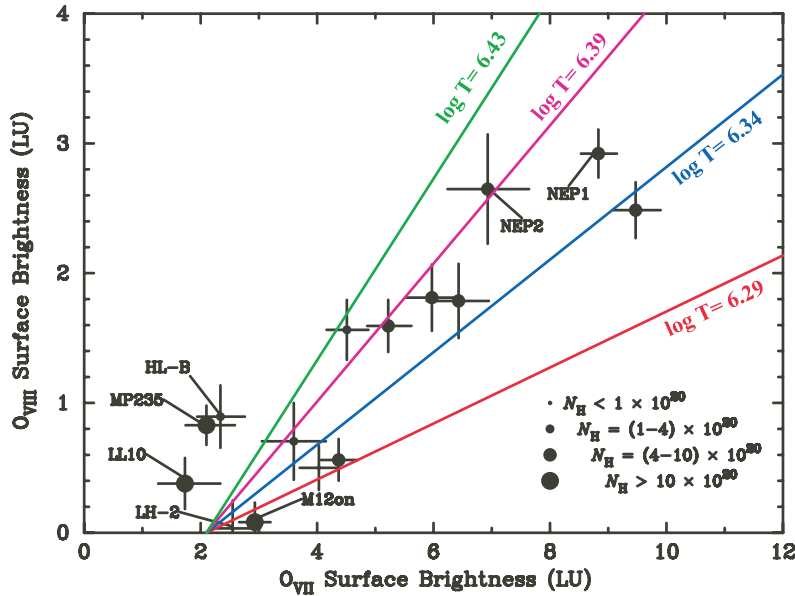


Fig. 2.12 O_{VII} and O_{VIII} surface brightnesses relation obtained for 14 high-latitude directions observed with *Suzaku* near the solar minimum (Yoshino et al. (2009)).

From combined analyses of the absorption lines and emission lines of approximately same directions, we can constrain the line of sight length of the plasma since absorption is proportioned to ZnL while emission is proportioned to Zn^2L , where Z is a vertical distance from galactic plane, n is the plasma density and L is the path length. Yao et al. (2009) used *Chandra* grating spectrum of the X-ray binary source in LMC, LMC X-3 for absorption and

Suzaku CCD spectrum about from LMC X-3 for emission. They introduced a gradient in density and temperature along the line of sight to explain their spectral fit and obtained

$$n = n_0 e^{-\frac{z}{h_n}}, T = T_0 e^{-\frac{z}{h_T}}, \quad (2.7)$$

where n_0 and T_0 are the density and temperature on the plane $Z = 0$, h_n and h_T are the density and temperature scale heights, respectively. They obtained scale heights of 1-5 kpc, suggesting that the hot gas is in the halo of our Galaxy. Hagihara et al. (2011) and Sakai et al. (2014) applied the same method to the directions of two Blazars, PKS 2155-304 and Mkn 421 and obtained the similar results.

Chapter 3

Instrument

3.1 The *Suzaku* X-ray Observatory

Following the *Hakucho*, *Tenma*, *Ginga* and *ASCA* X-ray satellite missions, *Suzaku* was launched as the fifth Japanese X-ray observatory by a Japanese M-V rocket from the JAXA Uchinoura space center on July 10, 2005 (Mitsuda et al. (2007)). It was developed by the Institute of Space and Astronautical Science (ISAS, belongs to the Japan Aerospace Exploration Agency, JAXA) in close collaborations with the National Aeronautics and Space Administration's Goddard Space Flight Center (NASA/GSFC) and many other collaborators across the world. *Suzaku* was put into a near-circular orbit with an apogee of 568 km, inclination of 31.9 degrees and an orbital period of about 96 minutes (Fig. 3.1). The *Suzaku* satellite was protected by the geomagnetic field in this low orbit, therefore its instrumental background is lower and more stable than that of XMM-Newton and *Chandra*, that were put in long elliptical orbits. Figure 3.2 shows the overview of the *Suzaku* satellite. The total mass of the spacecraft is about 1700 kg. The length, after deployment of the extensible optical bench (EOB) that was performed in orbit, along to the telescope axis is 6.5 m. *Suzaku* completed its scientific mission due to difficulty of maintaining sufficient power supply on August 26, 2015, but exceeded its target observation life time of about two years. After about 50000 charge/discharge cycles, batteries were degraded as they were supposed to be and JAXA concluded that it was difficult to continue its scientific observations.

In the following sections, we describe minimal information about the *Suzaku* instruments relevant to this thesis. The full *Suzaku* technical description is available at

https://heasarc.gsfc.nasa.gov/docs/astroe/prop_tools/suzaku_td/suzaku_td.html.

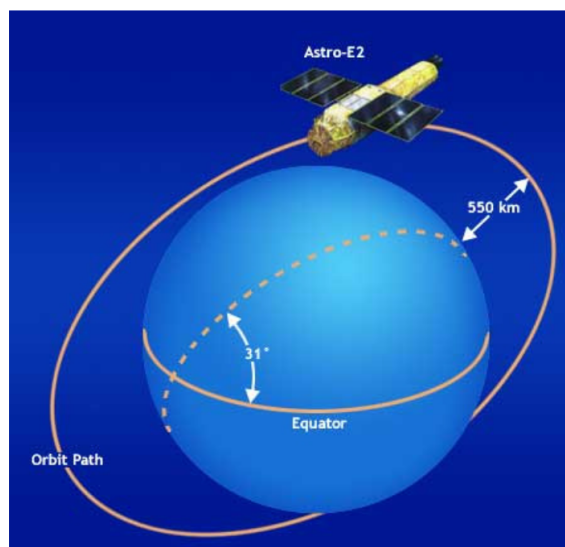


Fig. 3.1 The 96 minute *Suzaku* orbit.

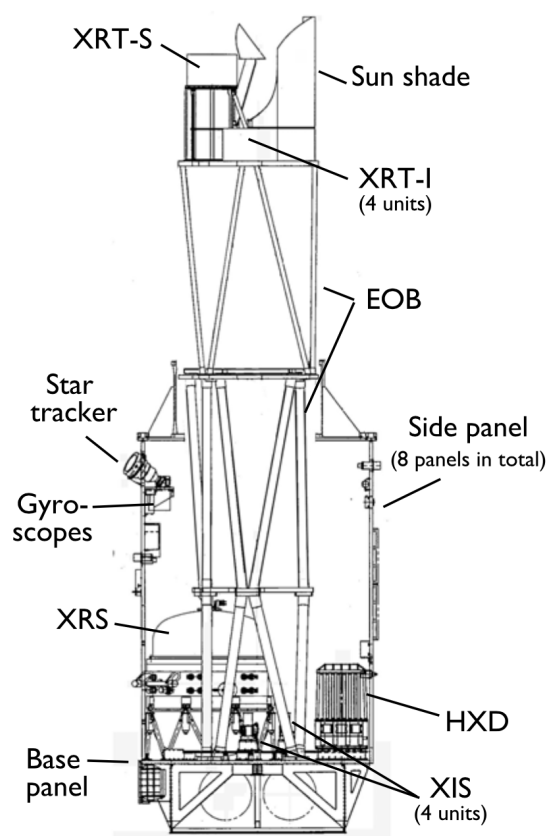


Fig. 3.2 Side view of *Suzaku* with the internal structures after the EOB deployment. Taken from Mitsuda et al. (2007).

3.2 The X-ray Imaging Spectrometer

3.2.1 Basics

The X-ray Imaging Spectrometer (XIS, Koyama et al. (2007)) is one of the three science instruments on-board *Suzaku*. The XIS was developed under the collaboration between MIT, ISAS, Osaka University and Kyoto University. The XIS successfully observed the first light on 11 August 2006, about a month after the launch. The XIS instrument consists of four X-ray charge-coupled devices (CCD), XIS0, XIS1, XIS2 and XIS3. The XIS1 CCD detector is shown in Fig. 3.3. The sensors are kept at -90°C all the time in order to suppress noises related to the dark current.

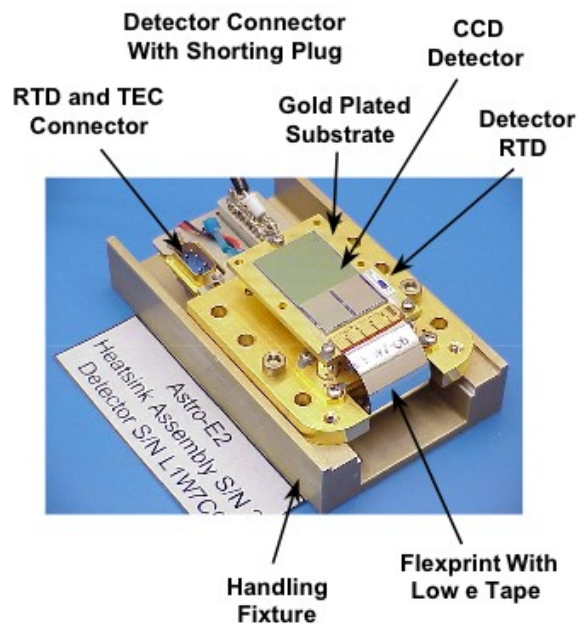


Fig. 3.3 The XIS1 CCD detector put onto a heat sink.

Each XIS sensor is placed on the focal plane of the co-aligned X-ray Telescope (XRT, Serlemitsos et al. (2007)) whose angular resolution is about $2'$ defined as a half power diameter (HPD). The field of view is $17'8 \times 17'8$ square field determined by the XIS CCD exposure area (25 mm squared) consisting of 1024×1024 pixels. A cross sectional view of the instrument is presented in Fig. 3.4. The optical blocking filter (OBF) made of a thin polyimide ($\text{C}_{22}\text{H}_{10}\text{N}_2\text{O}_4$) film with Al coating on both sides is located at 20 mm above the CCD detection surface for each sensor. The XIS1 is equipped with a thinned backside-illuminated (BI) device which enables substantially improved sensitivity at energies below 2 keV, compared to the front-side illuminated (FI) chips for the XIS0, 2 and 3.

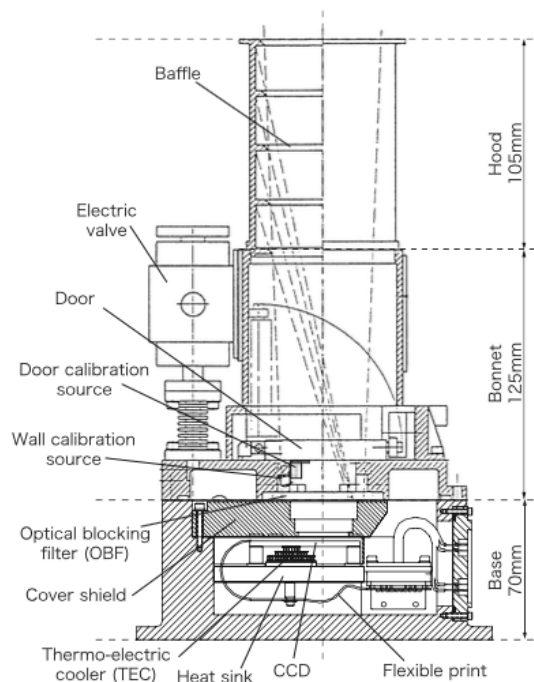


Fig. 3.4 Cross sectional view of the XIS instrument.

Fig. 3.5 shows schematics of the XIS sensors from the top. Each CCD chips is composed of four segments. Segment A, B, C and D which are connected to readout nodes individually. For inflight detector calibrations, two ^{55}Fe X-ray sources, which emit strong Mn $K\alpha$ (5.9 keV) and Mn $K\beta$ (6.5 keV), illuminate corners located at the far side of the readout nodes of the segments A and D. The XIS detectors had been damaged due to a micro-meteorite hit on orbit. The entire XIS2 and a part of the XIS0 were lost on November 9 2006 and June 23 2009 respectively. Although no major impact in scientific capability has been confirmed by the XIS calibration team, some light-leaking holes on the OBF were also detected in the XIS1 and XIS3 on December 18, 2009. An overview of capabilities of the XIS instruments and typical error budgets to be taken into account are given in Table 3.1 and 3.2 respectively.

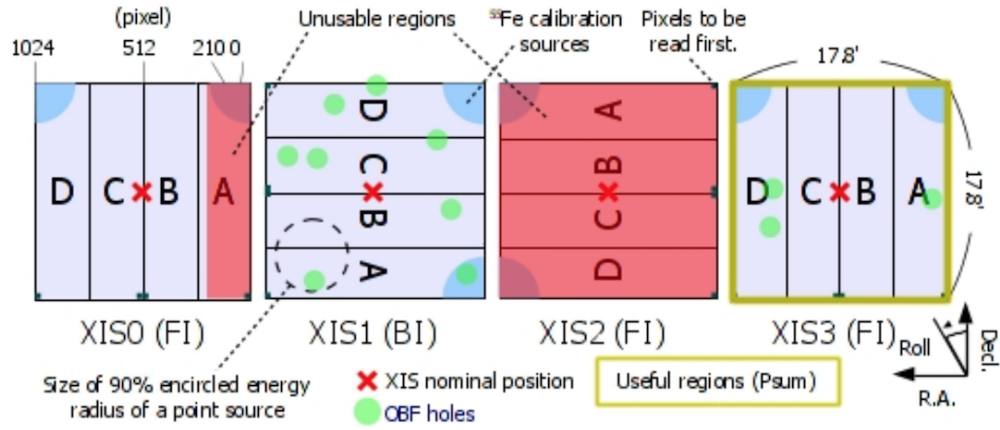


Fig. 3.5 Schematic of top view of the XIS instruments.

Table 3.1 Overview of *Suzaku* capabilities related to the XIS instruments.

S/C	Orbit apogee	568 km
	Orbital period	96 minutes
	Observing efficiency	~45 %
XRT	Focal length	4.75 m
	Field of view	17' at 1.5 keV 13' at 8 keV
	Plate scale	0.724 arcmin/mm
	Effective area	440 cm ² at 1.5 keV 250 cm ² at 8 keV
	Angular resolution	2' (HPD)
XIS	Field of view	17.8' × 17.8'
	Bandpass	0.2–12 keV
	Pixel grid	1024 × 1024
	Pixel size	24 μm × 24 μm
	Energy resolution	~130 eV at 6 keV
	Effective area	340 cm ² (FI), 390 cm ² (BI) at 1.5 keV 150 cm ² (FI), 100 cm ² (BI) at 8 keV
	Time resolution	8 s (Normal mode)

Table 3.2 Error Budgets of Scientific Instrument Calibrations, given by the XIS team.

	Calibration Item	Oct 2008	Requirement	Goal
XRT-I/XIS	On-axis effective area	$\sim 2\%$	5%	5%
	Vignetting	$\sim 10\%$	5%	2%
	On-axis EEF	$\sim 3\%$	5%	1%
	Off-axis EEF	$\sim 3\%$	20%	2%
	Optical axis position in XIS	$\sim 0.5'$	$< 0.2'$	$< 0.2'$
	Energy scale	max(0.2%, 5 eV)	0.1 %	0.1 %
	Energy resolution at 5.9 keV	1 %	1%	
	Contamination column density	$\sim 10^{18} \text{cm}^{-2}$	N/A	N/A
	OBF integrity	unbroken	broken/unbroken	broken/unbroken

3.2.2 Energy Gain and Resolution

Suzaku XIS CCD sensors have a Gaussian-like peak response function for monochromatic energy, with a very small low energy tail compared to the X-ray CCD instruments carried on Chandra and XMM-Newton. Fig. 3.6 shows comparison of simulated spectra for SNR E0102-72.3 with *Suzaku* (top left), *Chandra* (top right) and *XMM-Newton* (bottom) response functions. *Suzaku* can resolve many spectral peaks, whereas the other observatories cannot, showing *Suzaku* is suitable to observe a spectrum with emission lines such as the H-SWCX emissions. Fig. 3.7 shows the detector response to characteristic X-rays from a boric oxide target for the BI and FI XIS sensors (tested on the ground) (Bautz et al. (2004)). FWHM below 500 eV is 50-60 eV, which is the best energy resolution achieved among the X-ray CCD sensors developed for the astronomical observations. The BI sensor also shows significantly higher quantum efficiency than the FI sensor below 600 eV, suitable for the SXDB observation including the 1/4 keV band.

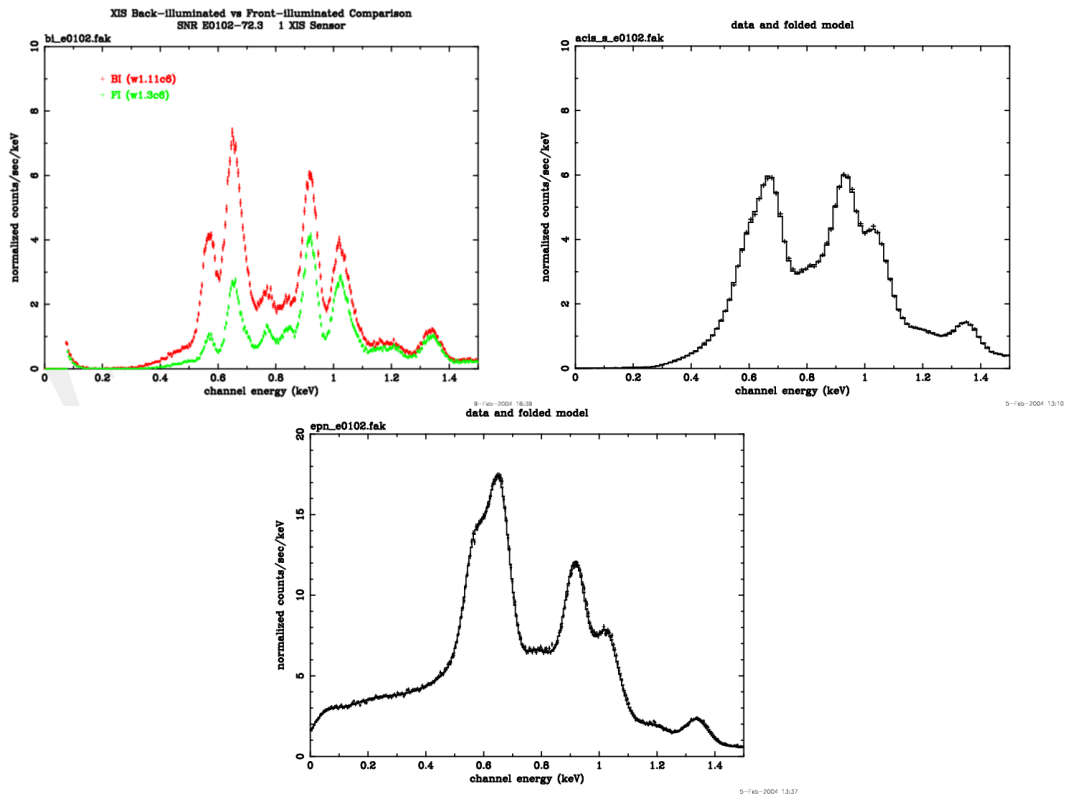


Fig. 3.6 Comparison of simulated spectra for SNR E0102-72.3 with *Suzaku* (top left), *Chandra* (top right) and *XMM-Newton* (bottom) response functions.

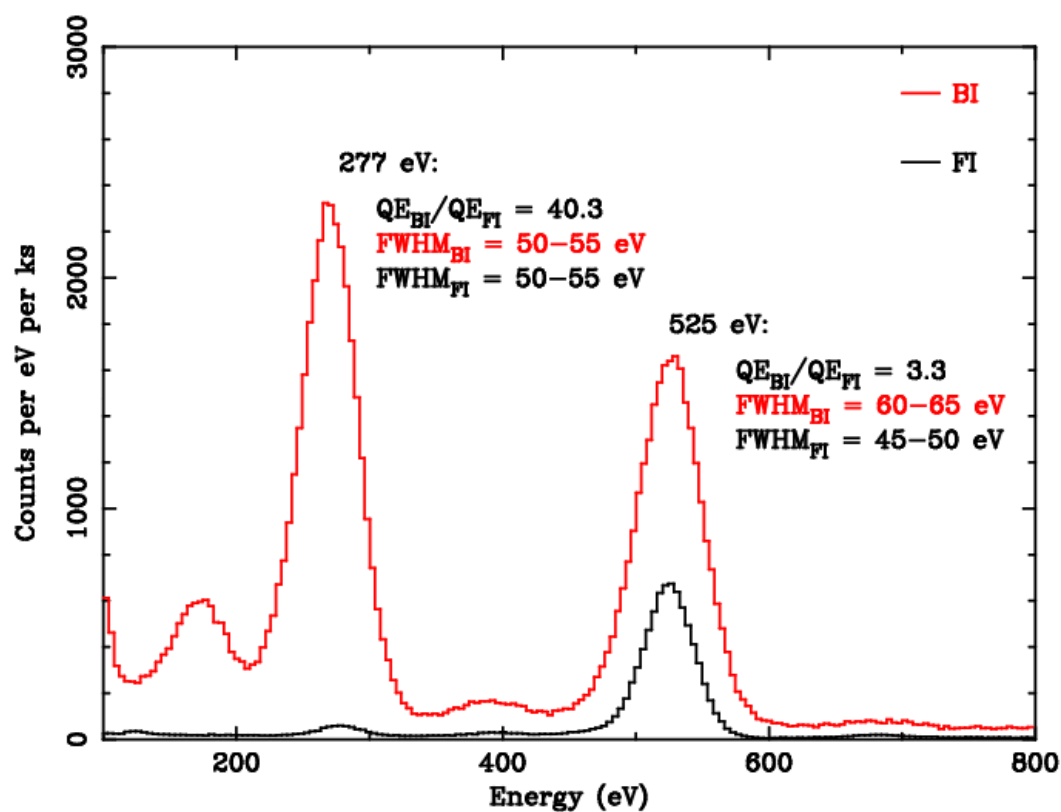


Fig. 3.7 Response of the back-illuminated (BI; red) and front-illuminated (FI; black) XIS sensors to characteristic X-rays from a boric oxide target (Bautz et al. (2004)). Note that the BI device also detects boron-K emission, indicating that it can measure the energy range as low as 180 eV.

3.2.3 Non X-ray Background

The XIS instruments have low background mainly due to *Suzaku*'s low orbit and the instrumental design. The non X-ray background (NXB) consists of several sources. The most dominant one is events created by ionization losses of charged cosmic ray particles. Fluorescence X-rays from materials used in the spacecraft such as Al K_{α} (1.486 keV), Si K_{α} (1.740 keV), Au M_{α} (2.123 keV) and so on are also considered to be the NXB. Flickering pixels also generate the NXB but the influence is negligible for the early observations, however it can be significant especially below 0.4 keV for observations performed after 2007.

3.3 Degradation of the Low Energy Quantum Efficiency

The quantum efficiency (QE) below 1 keV had been significantly degraded over the *Suzaku* operation period due to accumulation of contaminant material(s) onto the OBF for each sensor. The main contamination source is considered to be anti vibration rubber, that supposed to protect the Inertial Reference Unit (IRU) from impacts and vibrations during launch. It is believed that DEHP (diethylhexyl phthalate ($C_{24}H_{38}O_4$), which is a common form of phthalate ester and one of the most common outgas in the satellite) was leaked and evaporated from the IRU to the interior of the spacecraft. The OBF was cooler than other parts of the satellite, thus the contamination was accumulated onto it.

It is known that the contaminant consists of several different materials such as H, C, N and O. The time dependence of the column density for each element had been monitored regularly by observing several calibration objects and contamination growth curves are provided as shown in Fig. 3.8. The chemical composition measured phenomenologically is not consistent to the DEHP and varies in time. The spatial dependence of the thickness across the field of view had been also monitored by looking at the bright-side earth. These monitoring results are included in calibration files provided by the XIS calibration team.

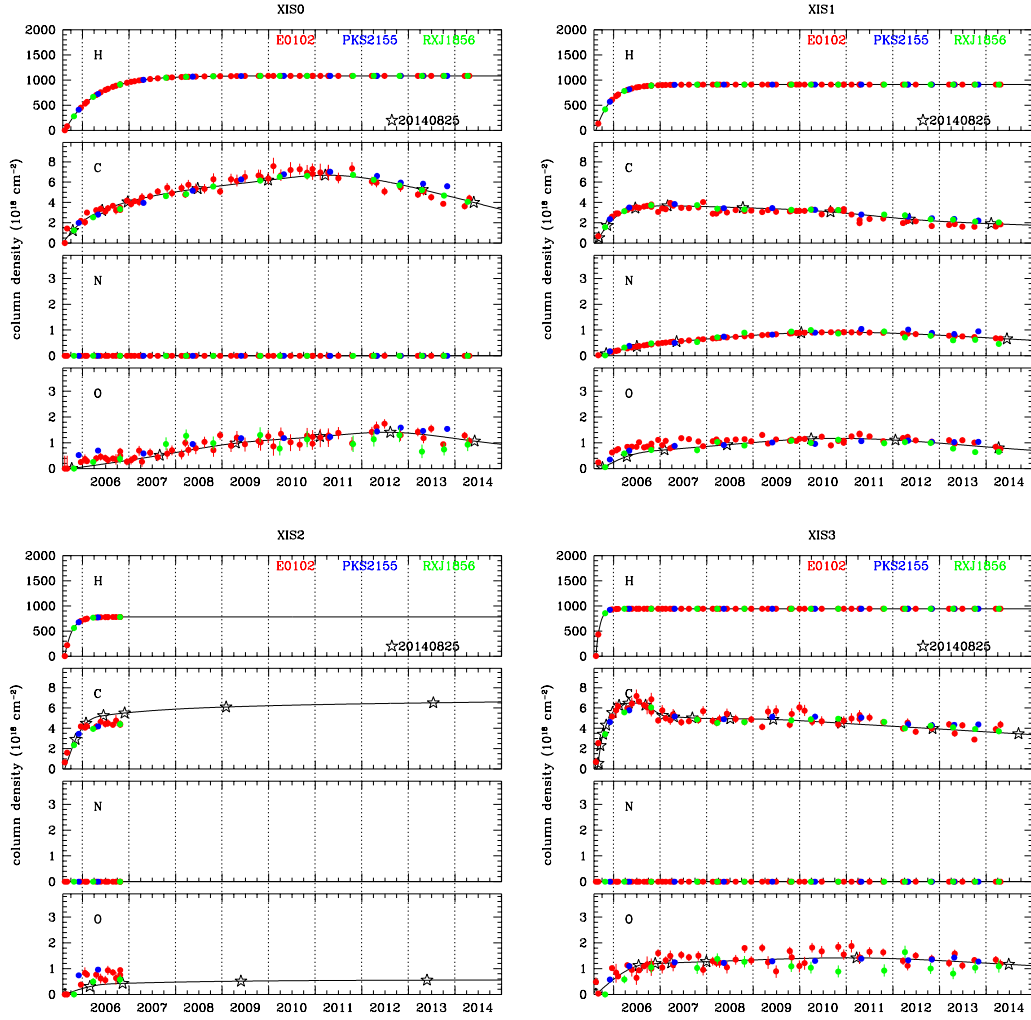


Fig. 3.8 Time dependence of the column density for each element for each detector. The dots show the estimated column densities based on observations of a line-dominated supernova remnant (E0102.2-7219, red), a blazer (PKS2155-304, blue) and a super-soft isolated neutron star (RXJ1856.5-3754, green). The solid black lines are the contamination growth curves modeled with phenomenological functions of time. The stars shows column densities predicted by using the current contamination file (released on August 25th, 2014).

Chapter 4

Revising the Quantum Efficiency Calibration Model for the XIS1 Instrument

4.1 Purpose of Analysis

Quantum efficiencies (QE) below 1 keV of the XIS had been rapidly degraded especially in the early phase of the *Suzaku* in-orbit operations to the contamination accumulated on the optical blocking filters (OBF). *Suzaku* had observed celestial calibration objects regularly to monitor the amount of contamination. As a result, time variability of the QE is well reproduced in the energy band above 0.3 keV. Below the carbon edge at 0.284 keV, however, not much attention has been paid because an observed count rate could not be explained by the combination of absorptions of typical contaminant elements such as hydrogen, carbon, nitrogen and oxygen, while maintaining consistency with other energy bands.

The purpose of this chapter is to reconstruct an empirical QE calibration model to be able to analyze observational data quantitatively including the 1/4 keV band.

Throughout this thesis, we used only data taken by the *Suzaku* back-illuminated (BI) XIS1 instrument, which is more sensitive to soft X-rays than the front-illuminated (FI) XIS sensors. All the data used in this thesis were taken with the XIS1 default observation mode: the normal clocking mode, the 3×3 and 5×5 editing modes, and no window option. All observational data are publicly available from archives.

4.2 RX J1856.5-3754 as a soft X-ray calibrator

RXJ 1856.5-3754 (hereafter RXJ1856) is an isolated neutron star located at 123 pc away from us (Walter et al. (2010)), that was first confirmed through the observation in the soft X-ray band with the Position Sensitive Proportional Counter (PSPC) onboard ROSAT (Neuhäuser et al. (1996)). An X-ray spectrum from RXJ1856 is characterized by a blackbody thermal radiation from the surface of the star, of which temperature is approximately $kT^\infty \simeq 63$ eV, where kT^∞ is the apparent blackbody temperature in which gravitational redshift is not corrected. RXJ1856 has been observed many times with various X-ray instruments. This is because not only for scientific motivations to study atmosphere and the internal structure of neutron stars, but also it has been an ideal target for calibration purposes especially at low energy side 0.2-1 keV, owing to its brightness of $\simeq 1.5 \times 10^{-11} \text{ erg s}^{-1} \text{ cm}^{-2}$ (see Fig. 4.1, taken from Burwitz et al. (2003)). The flux in the optical band is seven times brighter than an extrapolation of the best-fit single blackbody radiation model determined in the X-ray band. In order to solve this discrepancy, a two-temperature blackbody radiation model ($kT \sim 63$ eV and $kT \sim 32$ eV) was introduced (Pons et al. (2002) and Beuermann et al. (2006)). Table 4.1 shows the best fit parameters they derived, which have been referred for cross calibrations for instruments onboard *XMM-Newton*, *Chandra* and *Suzaku* in the 0.2-1.0 keV band.

Table 4.1 The best fit parameters to the RXJ1856 spectrum with the two-temperature blackbody radiation model determined by Beuermann et al. (2006).

Parameter	Value \pm Error
kT_1 (eV)	62.83 ± 0.41
kT_2 (eV)	32.26 ± 0.72
R_1/d (km/pc)	0.0378 ± 0.0003
R_2/d (km/pc)	0.1371 ± 0.0010
N_{HI} (10^{20} cm^2)	1.1 ± 0.03

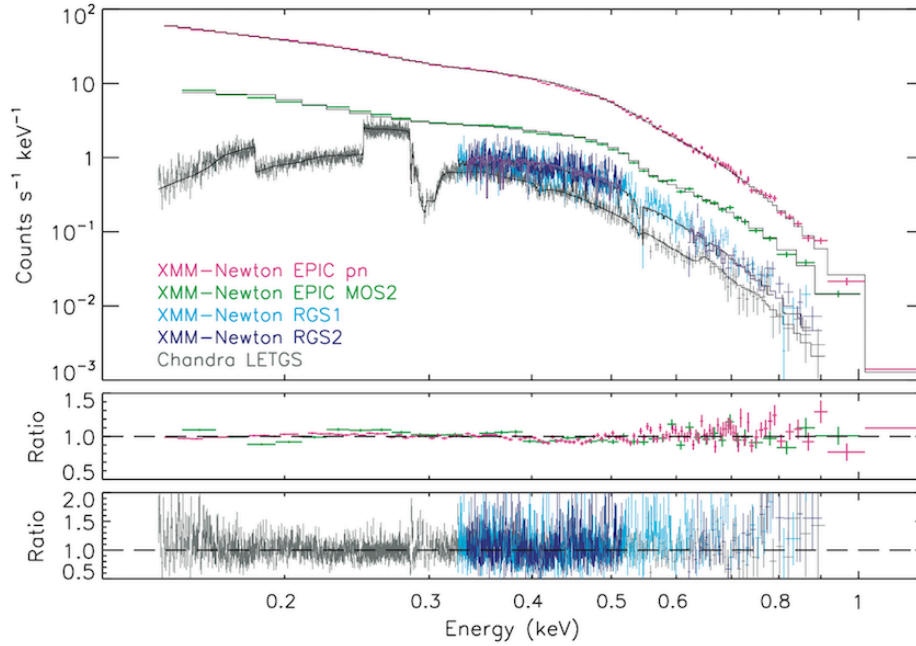


Fig. 4.1 The top panel shows the countrate spectra of RX J1856 obtained with XMM-Newton and Chandra with the best single blackbody model fit to each instrument. The bottom two panels show the ratio between the data and the model for both the CCD detectors and the high resolution grating instruments.

4.3 Observation and Data Reduction

4.3.1 Observational Data Set

Suzaku observed RXJ1856 twice a year from its launch year 2005 until 2014. Most of the observations were performed with a standard observation mode with the same pointing direction $(\alpha, \delta) = (284.150, -37.910)$ within $\sim 30''$. However, there are two exceptional observations in 2010 and 2013. The first one (observation ID 104022020) was performed with an offset in pointing. The second one was carried out with a 1/4 window option. We did not include these data in our sample because they did not fit as samples for homogeneous analysis. An observation list with abbreviations for referring in this chapter is given in Table 4.2. Fig. 4.2 shows an example of images in different energy bands taken by the XIS1. It is worth mentioning that the source is clearly detected in the 100-150 eV band, implying that one could perform spectral analysis or at least obtain the counting rate even below 0.2 keV, if the detector responses are properly calibrated.

Table 4.2 Suzaku RXJ1856 observation log. The nominal exposure is the exposure time left after the standard data processing. The usable exposure means the exposure time after further data screening applied.

Abbreviation	Obs. ID	Start Date yyyy-mm-dd	Nominal Exposure ksec	Usable Exposure ksec	RA deg.	Dec deg.	Roll angle deg.
RX05b	100041010	2005-10-24	76.3	23.8	284.150	-37.910	269.426
RX06a	100041020	2006-03-23	79.2	72.0	284.143	-37.910	84.013
RX06b	101009010	2006-10-20	40.8	13.8	284.149	-37.908	254.295
RX07b	102014010	2007-10-15	41.3	36.0	284.148	-37.908	271.935
RX08a	102015010	2008-03-22	50.7	36.5	284.144	-37.910	89.704
RX08b	103006010	2008-10-20	43.0	24.1	284.150	-37.908	280.509
RX09b	104022010	2009-10-23	43.5	30.5	284.148	-37.909	277.829
RX10a2	104022030	2010-03-26	42.4	30.3	284.142	-37.907	77.586
RX10b	105008010	2010-10-27	40.1	26.5	284.149	-37.917	271.239
RX11b	106009010	2011-10-22	39.3	9.7	284.149	-37.915	269.059
RX12a	107007010	2012-04-02	42.1	27.7	284.144	-37.900	88.502
RX12b	107007020	2012-10-20	44.0	17.2	284.149	-37.909	269.000
RX13a	108007010	2013-04-15	40.7	14.1	284.144	-37.909	89.816
RX14a	109008010	2014-04-08	40.0	25.0	284.144	-37.911	88.700
RX14b	109008020	2014-10-23	40.0	8.5	284.149	-37.909	269.169

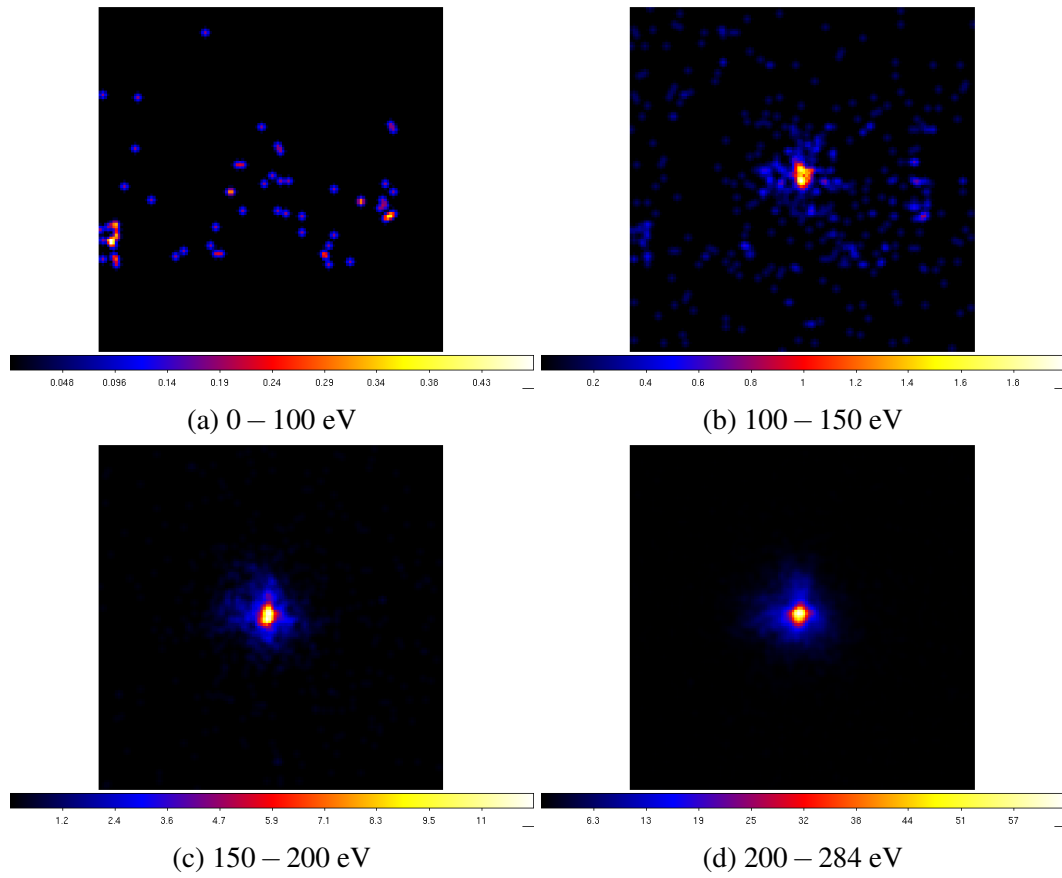


Fig. 4.2 An example of RXJ1856 images of RX05b in different energy bands taken by the XIS1 . The energy ranges are (a) 0-100 eV, (b) 100-150 eV, (c) 150-200 eV and (d) 200-284 eV. The source is clearly detected that above 100 eV.

4.3.2 Data Screening

We processed *Suzaku* XIS1 data using the HEASoft¹ software package version 6.22.1 provided by NASA High Energy Astrophysics Science Archive Research Center (HEASARC). For the XIS1 sensor and XRT calibrations, we applied the latest calibration files available to date, released on 7 June, 2016 and 30 June, 2011 respectively.

We first ran the *aepipeline* script² with the recommended screening criteria³ as the standard data processing to produce calibrated and screened XIS1 events files. We combined the event files that were recorded in the 3×3 and 5×5 modes, and extracted the data taken when the geomagnetic cut-off rigidity (COR2) exceeded 8 GV in order to reduce the non-X-ray background (NXB) (Tawa et al. (2008)).

Secondly, we investigated influence of contamination from solar X-rays scattered off the Earth's atmosphere. An indication of the contamination can be probed with the prominent oxygen fluorescent line ($O_I K\alpha$, 0.525 keV) (Sekiya et al. (2014)). We checked a counting rate in the 0.45-0.6 keV band as a function of the day earth elevation angle, which is defined as the angle between *Suzaku*'s line of sight and the limb of the sunlit Earth, and compared with an averaged counting rate observed when *Suzaku* revolved around the night earth side. Fig. 4.3 shows the comparison result for LH07 as an example. We defined an acceptance threshold as Δ/σ less than 2, where Δ and σ are a ratio of the counting rates and a calculated statistical error respectively. This corresponds to the $DYELV > 60$ degrees in this case.

Thirdly, we removed contamination from the geocoronal SWCX emission by following a manner presented by Fujimoto et al. (2007), Yoshino et al. (2009) and Yoshitake et al. (2013). We used data from *ACE* or *Wind* satellite for monitoring the solar wind proton flux during each observation. We checked correlation between the solar wind proton flux and the X-ray counting rate in the 0.45-0.6 keV band. We filtered out a time zone where the correlation was detected.

Finally, We excluded events detected on pixels identified as flickering pixels at any duration during the satellite life by applying a noisy pixel map provided by the XIS calibration team⁴. In the standard processing of the XIS data, hot pixels and flickering pixels are removed by the *sisclean*⁵ tool. Hot pixels are defined as pixels that always output pulse heights larger than the hot-pixel threshold even without input signals. The XIS instruments can detect hot pixels on-board easily by comparing the initial and updated dark levels of the

¹<https://heasarc.gsfc.nasa.gov/docs/software/heasoft/>

²<https://heasarc.gsfc.nasa.gov/ftools/caldb/help/aepipeline.html>

³Detailed parameters are described in Chapter 6 of the *Suzaku* Data Reduction Guide (<https://heasarc.gsfc.nasa.gov/docs/suzaku/analysis/abc/>)

⁴<https://heasarc.gsfc.nasa.gov/docs/suzaku/analysis/xisnxbnew.html>

⁵<https://heasarc.gsfc.nasa.gov/docs/software/ftools/headas/sisclean.html>

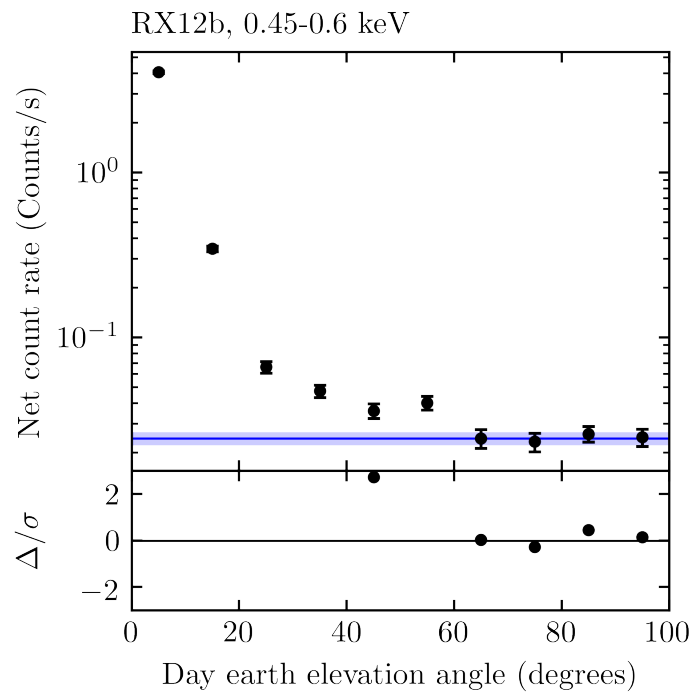


Fig. 4.3 The count rate for LH07 in the 0.45-0.6 keV as a function of the day earth elevation angle. the observed counting rate (black dots) was compared with an averaged counting rate observed during *Suzaku* moved around the night earth side, where there is no contamination from the solar scattered X-rays. In this case, We used data acquired when the elevation angle was more than 60 degrees.

sensors. However, outputs from some pixels are larger than the threshold intermittently and such pixels are called flickering pixels. These pixels are difficult to identify only with the observational data. The signals from those pixels are the potential sources of the noise especially on low energy side. We applied the noisy pixel map not only for the data, but also for the NXB, ARF and XRB that are presented in the following sections. Subsequent to the data filtering, we extracted X-ray events from the circular region within a 5' radius.

4.4 Non X-ray Background

We estimated a NXB spectrum for each observation by using the `xisnxbgen` tool (Tawa et al. (2008)), that produces the NXB spectrum from night-Earth observations corresponding to ± 150 days from the target observation date with the same COR distributions as the SXRb observations.

4.5 Detector Response Function

For each observation, we produced a Redistribution Matrix File (RMF) for conversion from an energy spectrum to pulse invariant (PI), and Auxiliary Response File (ARF; this file describes energy dependence of X-ray detection efficiency taking into account the telescope effective area and the detector quantum efficiency (QE) degradation) for the spectral fitting, by using the *Suzaku* FTOOLS software `xismfgen` and `xissimarfgen` respectively (Ishisaki et al. (2007)). We created these files in the energy range of 0.1-14 keV but note that `xissimarfgen` creates an ARF file only above 0.2 keV with the default settings. This is because in the QE file, a transmission factor for each contaminant material such as H, C, N and O is only available above 0.2 keV, while information such as an effective area of the XRT is available from 0.07 keV. We modified the transmission factors in the QE file in order to extend a lower limit to 0.1 keV. We assumed a point source for the emission source that is required to create the ARF file.

4.6 X-ray background

The X-ray background spectrum is obtained from the entire CCD area, excluding a 6' circular region around the source. In order to compensate a vignetting effect due to the XRT, we calculated conversion factors as a function of energy, by taking a ratio of the effective areas for the source and background regions. Fig. 4.4 shows the data, NXB and

non-corrected/corrected XRB for RX05b. The NXB is almost negligible in the entire energy band below 2 keV and the XRB becomes dominant above 0.8 keV. The count rate for each energy band is summarized in Table 4.3. We analyzed data in 0.17-0.8 keV band.

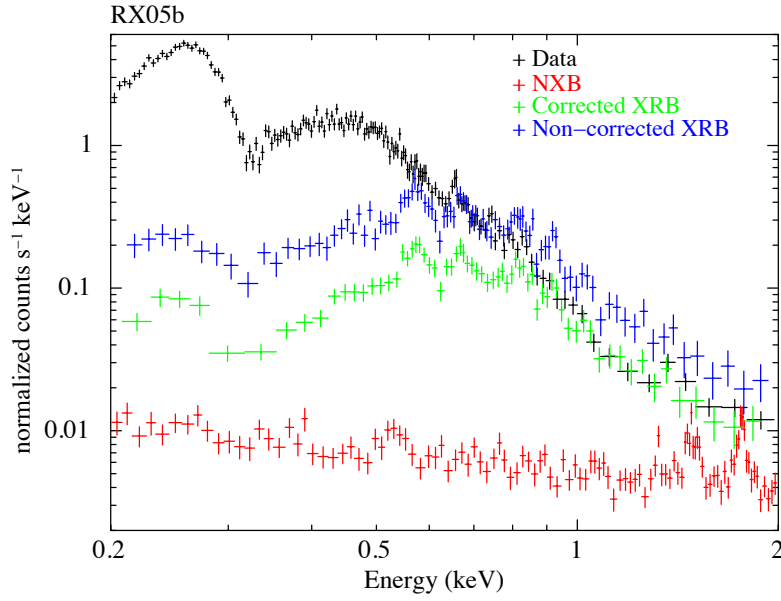


Fig. 4.4 Comparison of the data (black, X-ray and non X-ray background is not subtracted), NXB (red), non-corrected XRB (blue) and corrected XRB (green, see text) spectra.

Table 4.3 X-ray counting rate for each energy band for the observation RX05b.

E-band keV	Data cts/s	XRB cts/s	NXB cts/s	Source cts/s
0.1 – 0.2	$6.3_{-0.2}^{+0.2} \times 10^{-2}$	$6.5_{-1.0}^{+1.0} \times 10^{-3}$	$2.90_{-0.09}^{+0.09} \times 10^{-3}$	$5.3_{-0.2}^{+0.2} \times 10^{-2}$
0.2 – 0.3	$3.79_{-0.04}^{+0.04} \times 10^{-1}$	$6.5_{-0.4}^{+0.4} \times 10^{-3}$	$1.03_{-0.05}^{+0.05} \times 10^{-3}$	$3.72_{-0.04}^{+0.04} \times 10^{-1}$
0.3 – 0.4	$1.11_{-0.02}^{+0.02} \times 10^{-1}$	$4.0_{-0.3}^{+0.3} \times 10^{-3}$	$8.3_{-0.5}^{+0.5} \times 10^{-4}$	$1.07_{-0.02}^{+0.02} \times 10^{-1}$
0.4 – 0.5	$1.38_{-0.02}^{+0.02} \times 10^{-1}$	$8.2_{-0.4}^{+0.4} \times 10^{-3}$	$6.4_{-0.4}^{+0.4} \times 10^{-4}$	$1.28_{-0.02}^{+0.02} \times 10^{-1}$
0.5 – 0.6	$8.6_{-0.2}^{+0.2} \times 10^{-2}$	$1.47_{-0.06}^{+0.06} \times 10^{-2}$	$7.7_{-0.5}^{+0.5} \times 10^{-4}$	$7.0_{-0.2}^{+0.2} \times 10^{-2}$
0.6 – 0.7	$4.1_{-0.1}^{+0.1} \times 10^{-2}$	$1.38_{-0.06}^{+0.06} \times 10^{-2}$	$6.1_{-0.4}^{+0.4} \times 10^{-4}$	$2.7_{-0.1}^{+0.1} \times 10^{-2}$
0.7 – 0.8	$2.5_{-0.1}^{+0.1} \times 10^{-2}$	$1.18_{-0.06}^{+0.06} \times 10^{-2}$	$6.2_{-0.4}^{+0.4} \times 10^{-4}$	$1.3_{-0.1}^{+0.1} \times 10^{-2}$
0.8 – 0.9	$1.56_{-0.08}^{+0.08} \times 10^{-2}$	$1.07_{-0.06}^{+0.06} \times 10^{-2}$	$5.5_{-0.4}^{+0.4} \times 10^{-4}$	$4.3_{-1}^{+1} \times 10^{-3}$
0.9 – 1.0	$8.3_{-0.6}^{+0.6} \times 10^{-3}$	$7.1_{-0.5}^{+0.5} \times 10^{-3}$	$4.6_{-0.4}^{+0.4} \times 10^{-4}$	$8_{-8}^{+8} \times 10^{-4}$

4.7 Spectral model

We basically followed Beuermann et al. (2006) for spectral modeling of RXJ0658. We here briefly summarize their model. Detailed parameter values and a spectral shape as a function of energy are given in Table 4.4 and Fig. 4.5 respectively. This model consists of two blackbody components absorbed by interstellar matters. We applied the best fit values they derived for the temperature and source radius for the two blackbody components. In treating interstellar photoelectric absorption, we used the Tuebingen-Boulder ISM absorption model. This model calculates the cross section for X-ray absorption by the ISM as the sum of the cross sections for X-ray absorption due to the gas-phase ISM, the grain-phase ISM, and the molecules in the ISM. We employed the protostar abundances of Lodders (2003) as representative of cosmic abundances for the absorption model, except for carbon as they described in their paper. This is because a carbon abundance in the ISM is considered to be larger than in protostar (Clayton (2003); Zubko et al. (2004)). We also adopted the assumption for the grain size distribution which follows a MRN grain model (Mathis et al. (1977); Clayton (2003)) with a cutoff at a maximum grain radius of $0.5 \mu\text{m}$.

We used this model in the energy range of 0.17-0.8 keV as it is validated by Beuermann et al. (2006). Therefore our spectral fit is also limited by this energy range. We also used a gain offset function in XSPEC. Since we used below carbon K edge, a typical gain uncertainty of -5 eV was clearly detected.

Table 4.4 Parameter details of the spectral model as a reference. The spectral model is expressed as $tbvarabs(bbodyrad + bbodyrad)$ in XSPEC.

Component	Parameter	Unit	Value
<i>tbvarabs</i>	equivalent hydrogen column	10^{22} atoms cm^2	0.011
	abundance of carbon ¹		1.111
	molecular hydrogen column	10^{22} atoms cm^2	0
	grain density	g cm^3	1.0
	power-law index of grain sizes ²		3.5
	grain minimum size	μm	0.025
	grain maximum size	μm	0.5
	grain depletion fractions of carbon		0.6
<i>bbodyrad</i>	temperature	keV	0.06283
	norm	R_{km}^2/D_{10}^2 ³	142884
<i>bbodyrad</i>	temperature	keV	0.03226
	norm	R_{km}^2/D_{10}^2	1879640

¹ The protosolar abundances of Lodders (2003) is assumed as representative of cosmic abundances in this model, except for carbon.

² An index for the grain size distribution assumed a simplified grain model proposed in Mathis et al. (1977) (see text).

³ R_{km} is the source radius in km and D_{10} is the distance of the source in units of 10 kpc.

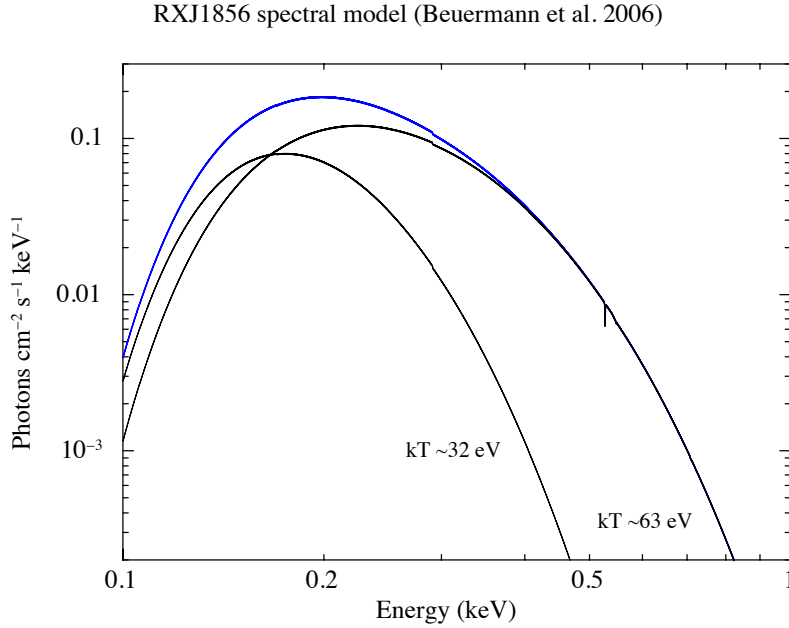


Fig. 4.5 Spectral model best estimated in Beuermann et al. (2006).

4.8 Spectral Analysis

We first compared an observed spectrum with the spectral model for each observation in order to evaluate the current status of the QE calibration especially in the 1/4 keV band. Fig. 4.6 shows the comparison results. In general, the data and model are in good agreement above 0.3 keV in most of the observations (except RX08b). However, the data systematically exceed the model by a factor of 2-4 below 0.3 keV for all observations. We note that this discrepancy cannot be explained by the characteristics of the detector itself. As we described the details in Chapter 3, one of the advantages of the XIS sensor is a good energy resolution with almost no energy tail on the low energy side. Uncertainties of the X-ray and non X-ray background are typically 10 % level, that are also negligible because a signal to background ratio is about 90 in the 1/4 keV band (see Table 4.3).

The current contamination model utilized to calculate the QE consists of 4 elements, namely hydrogen, carbon, nitrogen and oxygen. On the top left of Fig. 4.7, a transmission factor for each element is displayed (the column density for each element is assumed an approximate value in the current contamination model). In the 1/4 keV band, the absorption by hydrogen dominates the other elements because the hydrogen column density is abnormally high by a factor of 1000 than the others. Moreover, this hydrogen column density is fixed in

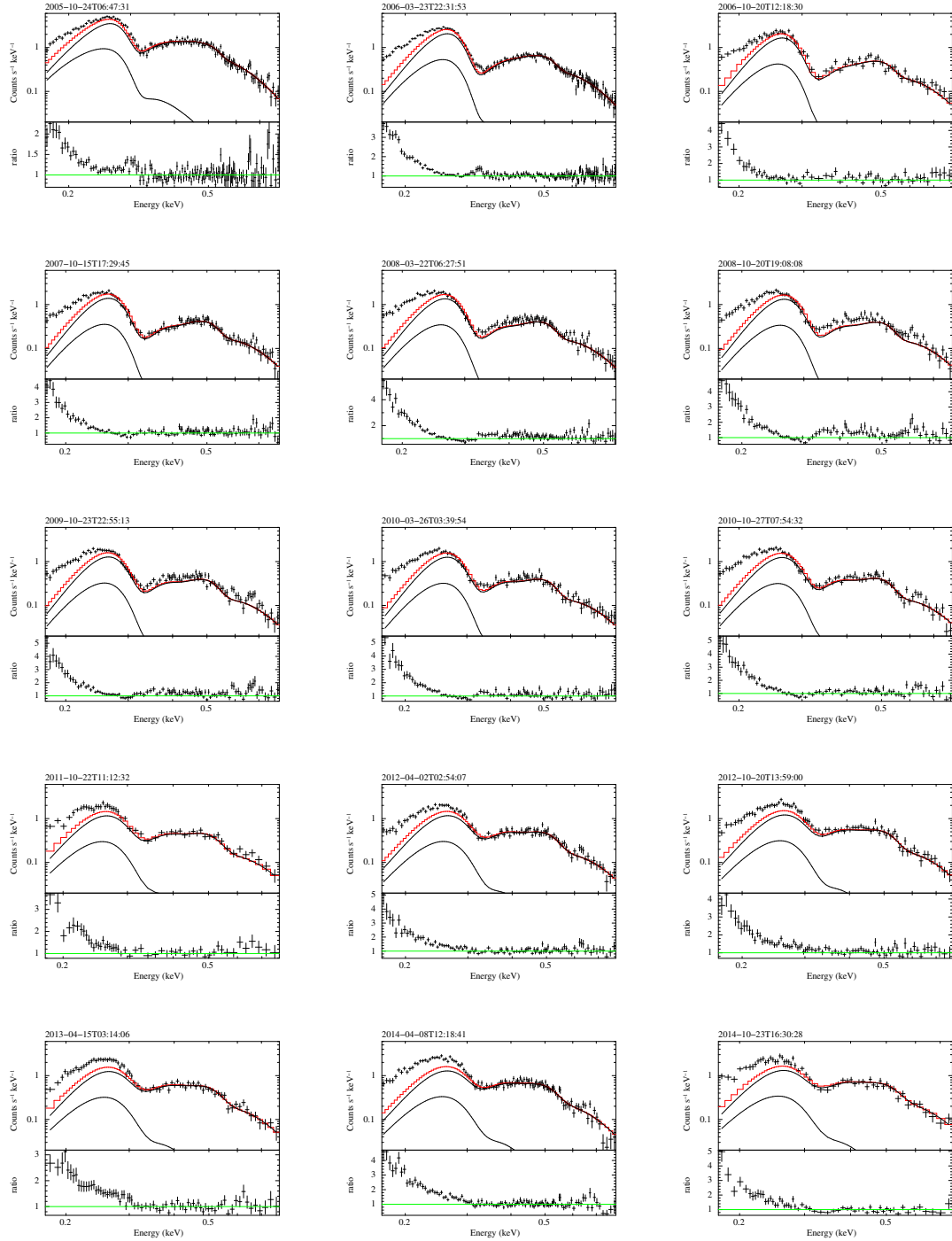


Fig. 4.6 Comparison of the observed spectra and folded model in the energy range of 0.17 - 0.8 keV. Note that spectral fitting was not performed for any observation.

most of the Suzaku observation period, while the other elements are treated as free parameters in spectral fitting for the QE calibration. We also found that any combination of H, C, N and O column densities could not explain the excessing data in the 1/4 keV band, while the data are well reproduced above 0.3 keV. This strongly indicates that the existence of other contaminant element(s).

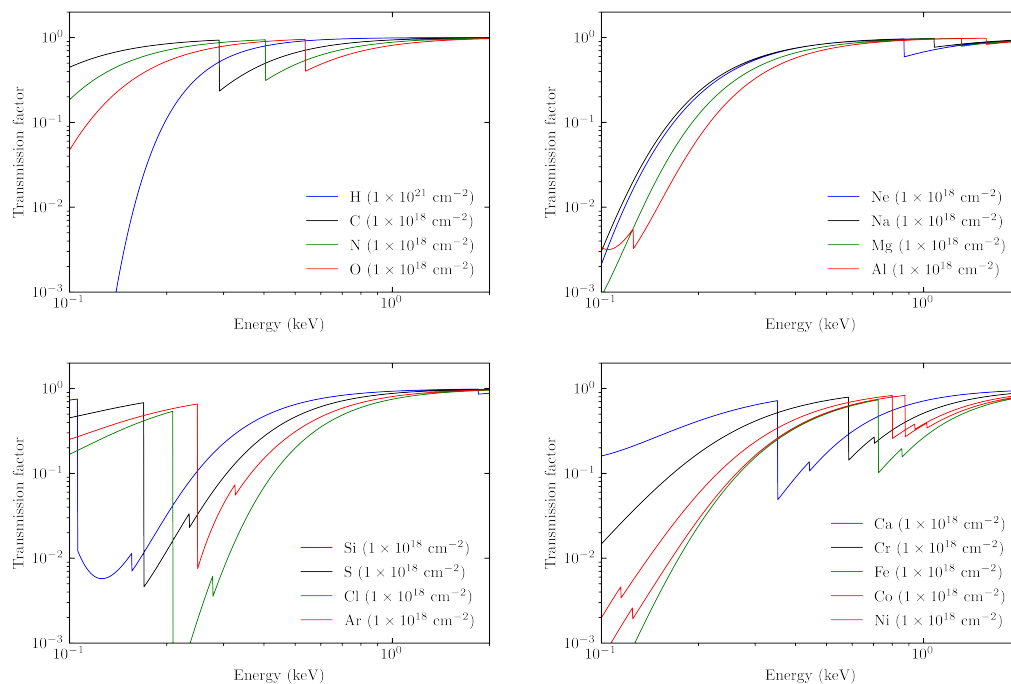


Fig. 4.7 Transmission factors assuming the column densities of $1 \times 10^{18} \text{ cm}^{-2}$ for various elements. The top left plot shows a transmission factor for H, C, N and O assuming an approximate column density obtained from the current contamination model (note that the Hydrogen column density is a factor of 1000 higher than the other elements).

We then tried to fit the 1/4 keV response to data by replacing hydrogen to various elements without assumptions of possible contaminant materials. We notice that hydrogen must be replaced by a new element because we could not solve the degeneracy of the parameters in spectral fitting. We prepared a detector response for each observation without taking into account the contamination and performed spectral fitting with the spectral model described in Table 4.4, multiplying a photoelectric absorption model *varabs*⁶. The column densities for the elements selected as a combination was treated as free parameters. It is known that there is an uncertainty of up to ~ 10 eV in the XIS absolute energy gain calibration at the low energy side. Figure 4.8 shows spectral fit results for RX09b, replacing H to He, Na, Al, Si, S, Cl and Ar. we found that the sulfur L edge absorption (indicated with the black solid line on the bottom left plot in Fig. 4.8 greatly eliminates residual at the 1/4 keV band and the contamination model consisting of carbon, nitrogen, oxygen and sulfur best reproduces the data in the 0.17-0.8 keV band. We performed further spectral fitting to the all data with the CNOS absorption model. Spectral fit results are presented in Table 4.5 and Fig. 4.9. The 1/4 keV discrepancy disappeared in all the data while maintaining a good reproducibility in the 0.3-0.8 keV range.

⁶<https://heasarc.gsfc.nasa.gov/xanadu/xspec/manual/node261.html>

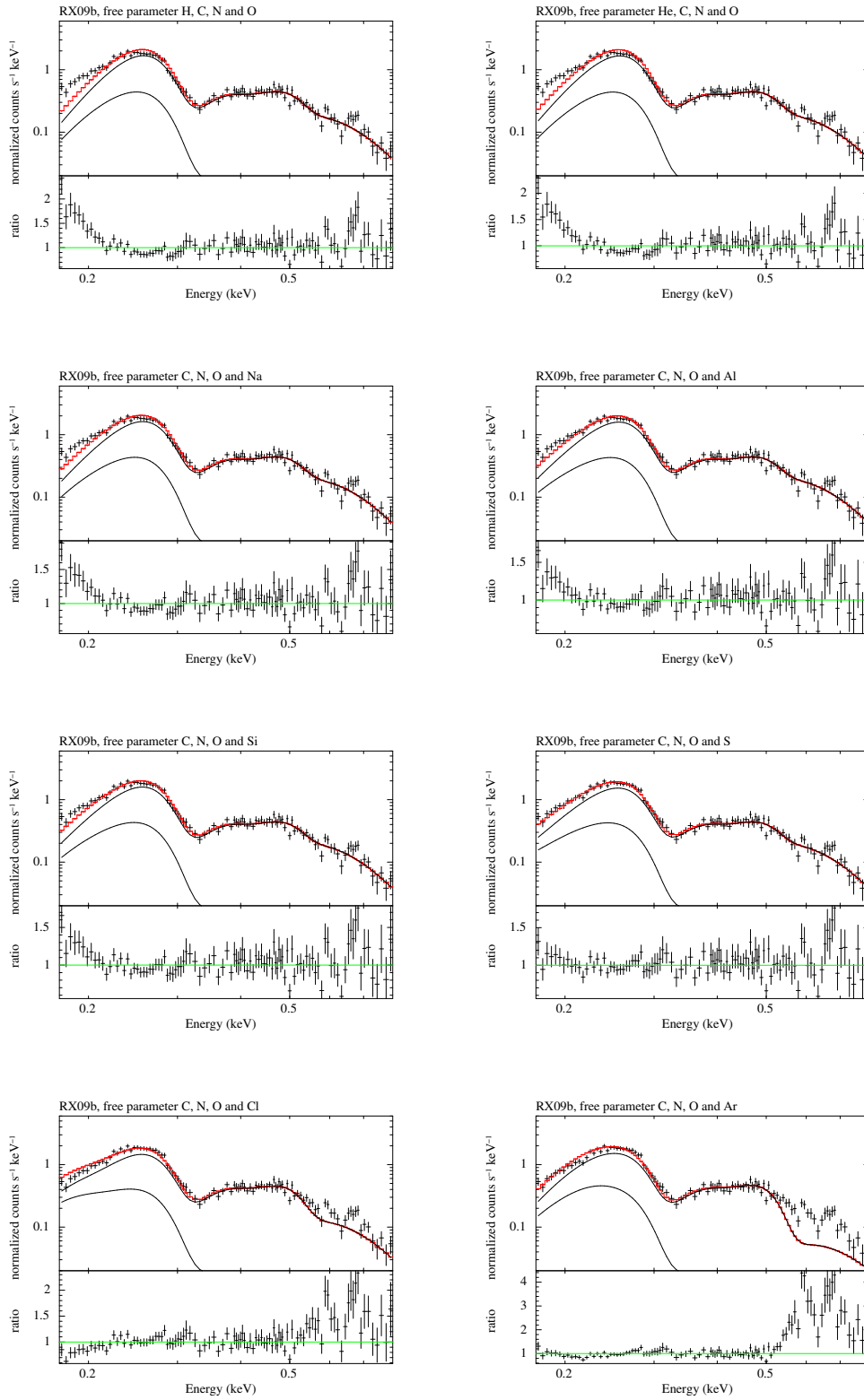


Fig. 4.8 RX09b spectral fit results, by replacing H to He, Na, Al, Si, S, Cl and Ar while maintaining carbon, nitrogen and oxygen. The column densities of 4 elements were treated as free parameters when fitting the spectrum.

Table 4.5 Spectral fit results with the CNOS contamination model.

	$AETIME^7$	Column density				Offset	$\chi^2/\text{d.o.f}$
	sec	Carbon 10^{18} cm^{-2}	Nitrogen 10^{18} cm^{-2}	Oxygen 10^{18} cm^{-2}	Sulfur 10^{18} cm^{-2}	eV	
RX05b	183555192	$1.44^{+0.03}_{-0.03}$	0 (fixed)	0 (fixed)	$0.134^{+0.004}_{-0.004}$	3	165.6/139
RX06a	196468411	$2.78^{+0.04}_{-0.04}$	$0.21^{+0.05}_{-0.05}$	$0.35^{+0.06}_{-0.06}$	$0.262^{+0.05}_{-0.06}$	-1	236.3/157
RX06b	214714693	$3.0^{+0.1}_{-0.1}$	$0.5^{+0.1}_{-0.1}$	$0.3^{+0.3}_{-0.2}$	$0.33^{+0.01}_{-0.01}$	-1	95.7/65
RX07b	245786913	$3.36^{+0.09}_{-0.09}$	$0.36^{+0.09}_{-0.09}$	$0.5^{+0.1}_{-0.1}$	$0.336^{+0.009}_{-0.009}$	-4	106.8/104
RX08a	259482517	$2.96^{+0.08}_{-0.08}$	$0.43^{+0.08}_{-0.08}$	$0.5^{+0.1}_{-0.1}$	$0.325^{+0.009}_{-0.009}$	-7	125.2/112
RX08b	277849347	$2.65^{+0.09}_{-0.08}$	$0.54^{+0.09}_{-0.09}$	$0.3^{+0.1}_{-0.1}$	$0.36^{+0.01}_{-0.01}$	-7	92.9/86
RX09b	309653808	$2.61^{+0.08}_{-0.07}$	$0.78^{+0.09}_{-0.09}$	$0.5^{+0.1}_{-0.1}$	$0.33^{+0.01}_{-0.01}$	-5	119.4/100
RX10a2	322893574	$2.74^{+0.08}_{-0.08}$	$0.76^{+0.09}_{-0.09}$	$0.8^{+0.1}_{-0.1}$	$0.30^{+0.01}_{-0.01}$	-7	106.2/93
RX10b	341481347	$2.73^{+0.09}_{-0.08}$	$0.61^{+0.09}_{-0.09}$	$0.8^{+0.1}_{-0.1}$	$0.30^{+0.02}_{-0.02}$	-9	94.4/86
RX11b	372600901	$2.4^{+0.1}_{-0.1}$	$0.7^{+0.2}_{-0.2}$	$0.4^{+0.2}_{-0.2}$	$0.30^{+0.02}_{-0.02}$	-3	38.5/49
RX12a	386651344	$2.42^{+0.08}_{-0.08}$	$0.56^{+0.09}_{-0.09}$	$0.8^{+0.1}_{-0.1}$	$0.27^{+0.01}_{-0.01}$	-2	107.4/98
RX12b	404059092	$2.05^{+0.09}_{-0.08}$	$0.6^{+0.1}_{-0.1}$	$0.8^{+0.2}_{-0.2}$	$0.24^{+0.01}_{-0.01}$	-1	70.5/80
RX13a	419313415	$2.16^{+0.10}_{-0.09}$	$0.6^{+0.1}_{-0.1}$	$0.8^{+0.2}_{-0.2}$	$0.22^{+0.02}_{-0.02}$	0	55.9/72
RX14a	450277384	$2.10^{+0.07}_{-0.07}$	$0.34^{+0.08}_{-0.08}$	$0.9^{+0.1}_{-0.1}$	$0.18^{+0.01}_{-0.01}$	-4	133.9/117
RX14b	467399952	$2.1^{+0.1}_{-0.1}$	$0.4^{+0.1}_{-0.1}$	$0.7^{+0.2}_{-0.2}$	$0.22^{+0.02}_{-0.02}$	-4	56.6/54

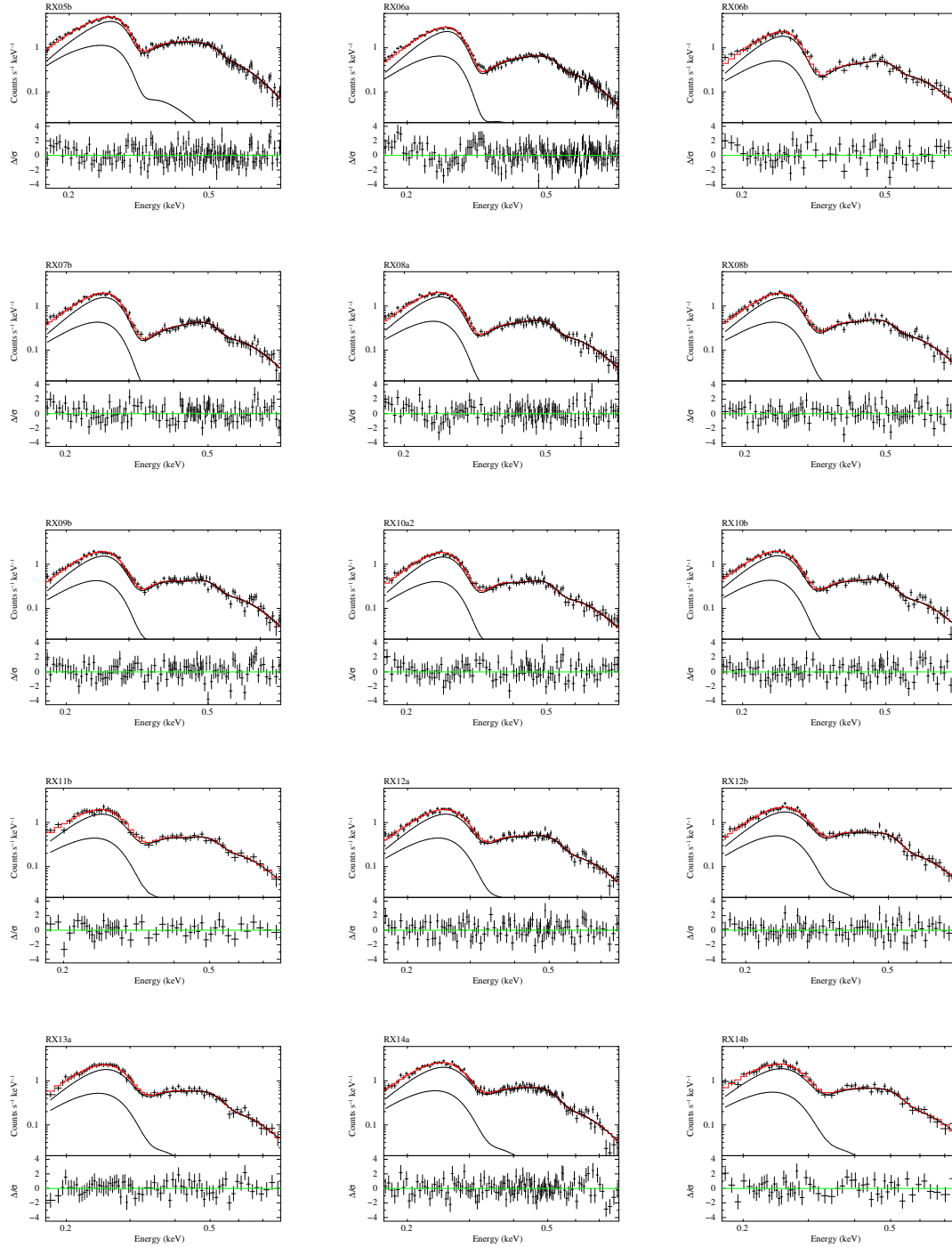


Fig. 4.9 Spectral fit results with the CNOS contamination model. The best fit parameters are shown in Table 4.5.

4.9 Revising Contamination Growth Model

We fitted the column densities listed in Table 4.5 for each element with an empirical model as a function of time. Time was defined as $AETIME^8$ for technical conveniences in model fitting. The fitting curves and best fit parameters are presented in Table 4.6. Fig. 4.10 shows the column densities derived from the observations along with the best fit curves and their errors corresponding to the 1σ interval. In general, the best fit curve for each element is in good agreement with the observed column densities over time, despite simplicity of the models compared to the current growth models (Fig. 4.11). For sulfur and carbon, variations of the column densities over time are similar to each other. It is known that the low energy effective area was rapidly decreased in the beginning of the observation period and then saturated or even slightly recovered over time. Therefore, the trend of variations in sulfur and carbon is somewhat understandable qualitatively. On the other hand, nitrogen and oxygen column densities behaves differently from the other two. It might indicate a limit of our analysis method and/or *Suzaku* had multiple contamination sources, which might be evaporated in a different time scale even. In any case, our primally goal of this analysis is to improve reproducibility of the 1/4 keV flux over time phenomenologically. The origin and materials of the contamination is beyond the scope of this thesis. Nevertheless, we emphasize that sulfur is not an unreasonable element as a contamination source. As we mentioned in Chapter 3, it is thought that the main contamination source is IRU rubber. This rubber was made of neoprene type rubber (private communication), that is normally produced with the polymerization reaction with sulfur. There might be a possibility that sulfur which has not been used in the polymerization reaction was detached from the rubber surface and accumulated onto the OBF together with DEHP.

We finally present the accuracy of the new QE calibration curve. Fig. 4.13 and 4.13 show the difference between the observed and predicted count rate in unit of percentage as a function of time from 2005 till 2014. The systematic uncertainty at 1/4 keV band is about 10 %, while keeping the same accuracy in the other energy band.

⁸Absolute time on the Astro-E2 satellite in unit of second originated at 00:00:00 January 1st, 2000 (UTC)

Table 4.6 Fitting curve models and best fit parameters for each element.

Element	Fitting curve	Best fit parameters		
		a	b	c
Sulfur	$a(1 - \exp(-b(\frac{t}{t_0} - 1)))\exp(-c(\frac{t}{t_0} - 1))$	0.49	8.17	0.53
Carbon	$a(1 - \exp(-b(\frac{t}{t_0} - 1)))\exp(-c(\frac{t}{t_0} - 1))$	3.51	14.62	0.36
Nitrogen	$a(\frac{t}{t_0} - 1)^2 + b(\frac{t}{t_0} - 1)$	-0.89	1.61	
Oxygen	$a(1 - \exp(-b(\frac{t}{t_0} - 1)))$	0.78	1.80	

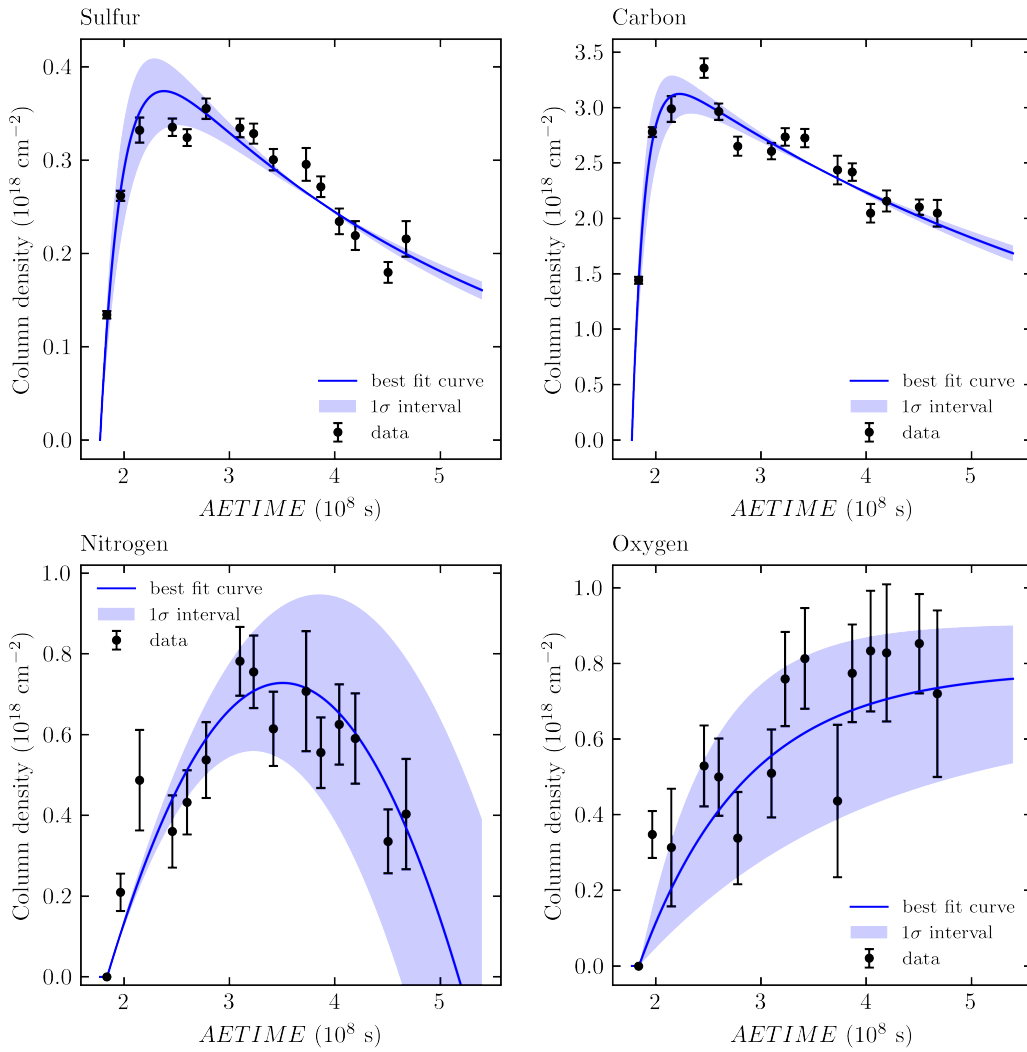


Fig. 4.10 Contamination growth curves for C, N, O and S. The details for the fitting functions are presented in Table 4.6.

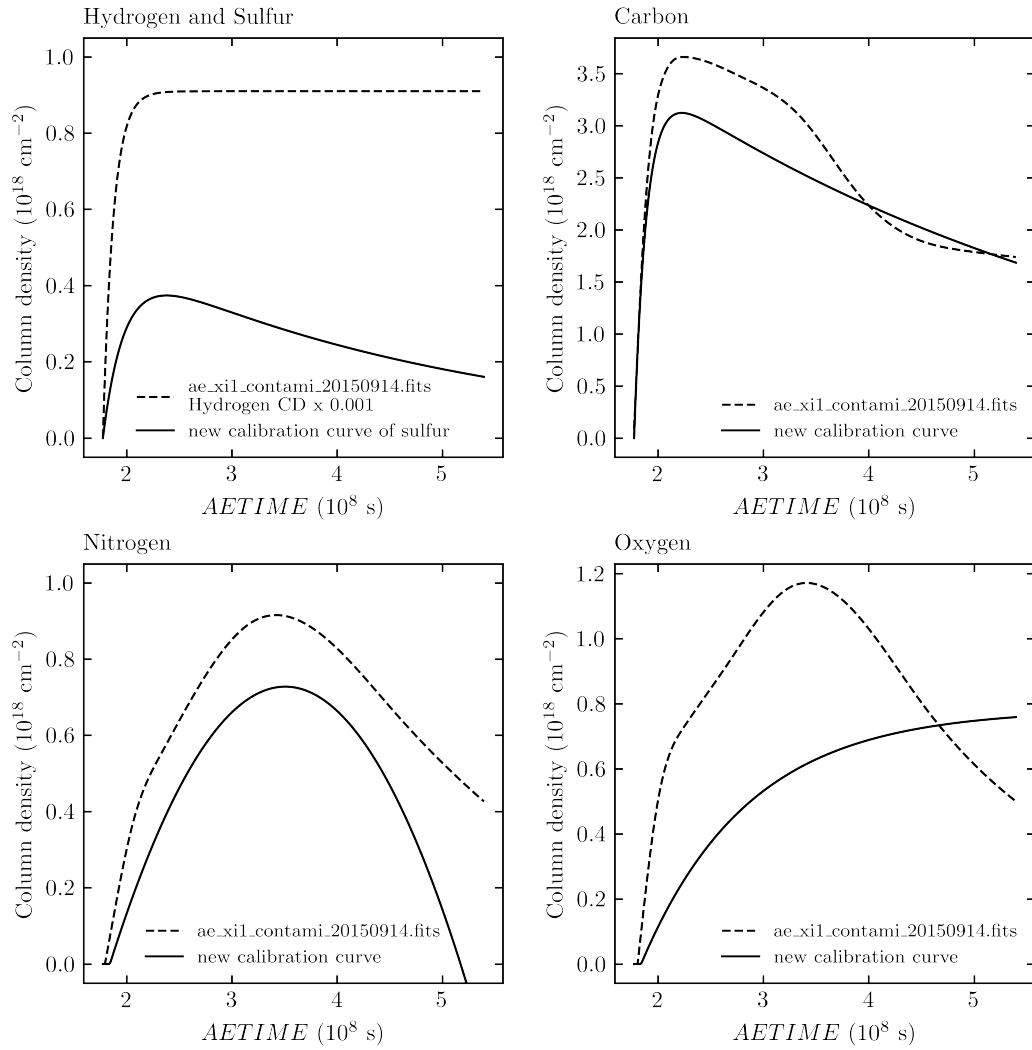


Fig. 4.11 Comparison of the current HCNO and new CNOS contamination models.

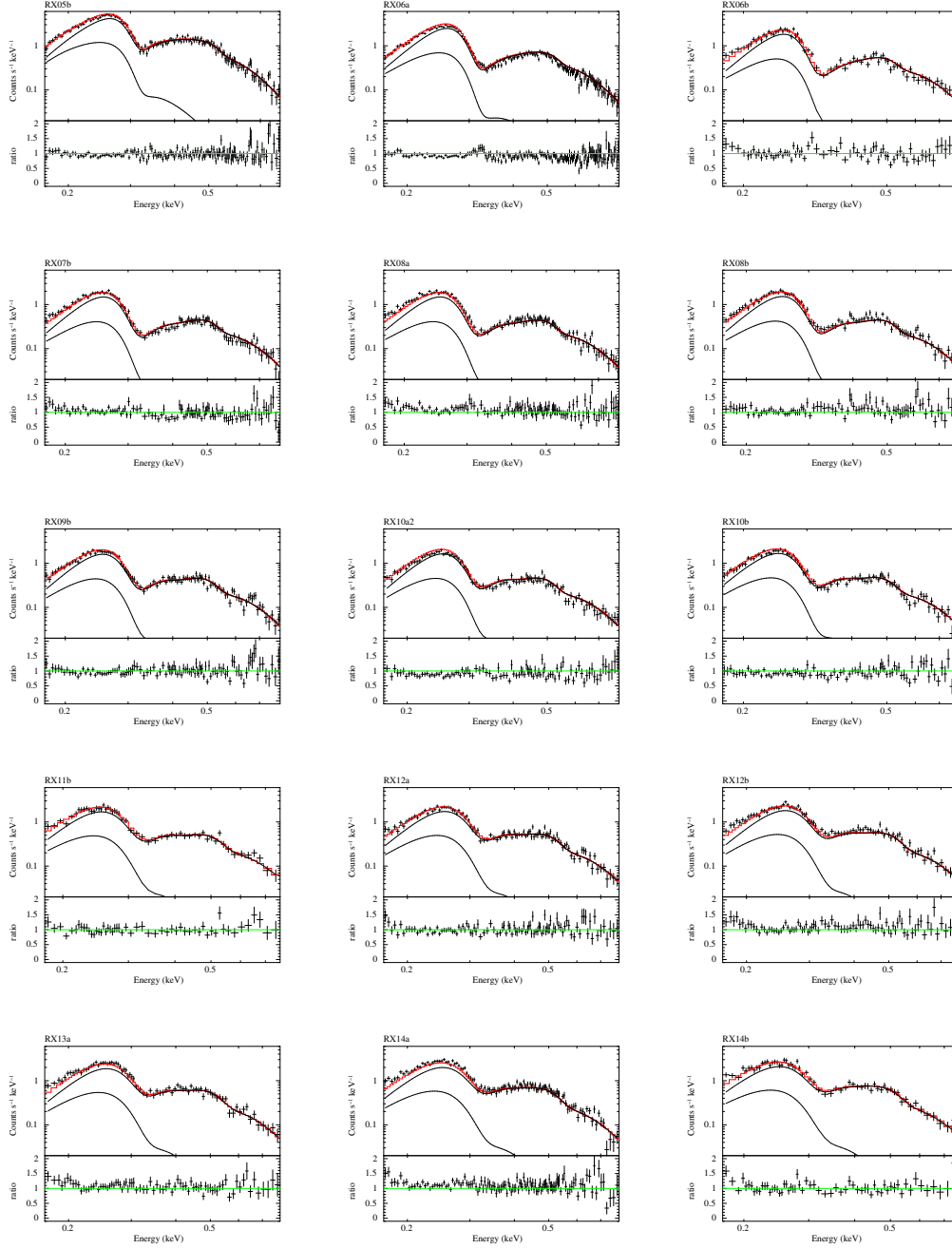


Fig. 4.12 Calibration results with the new contamination growth curves.

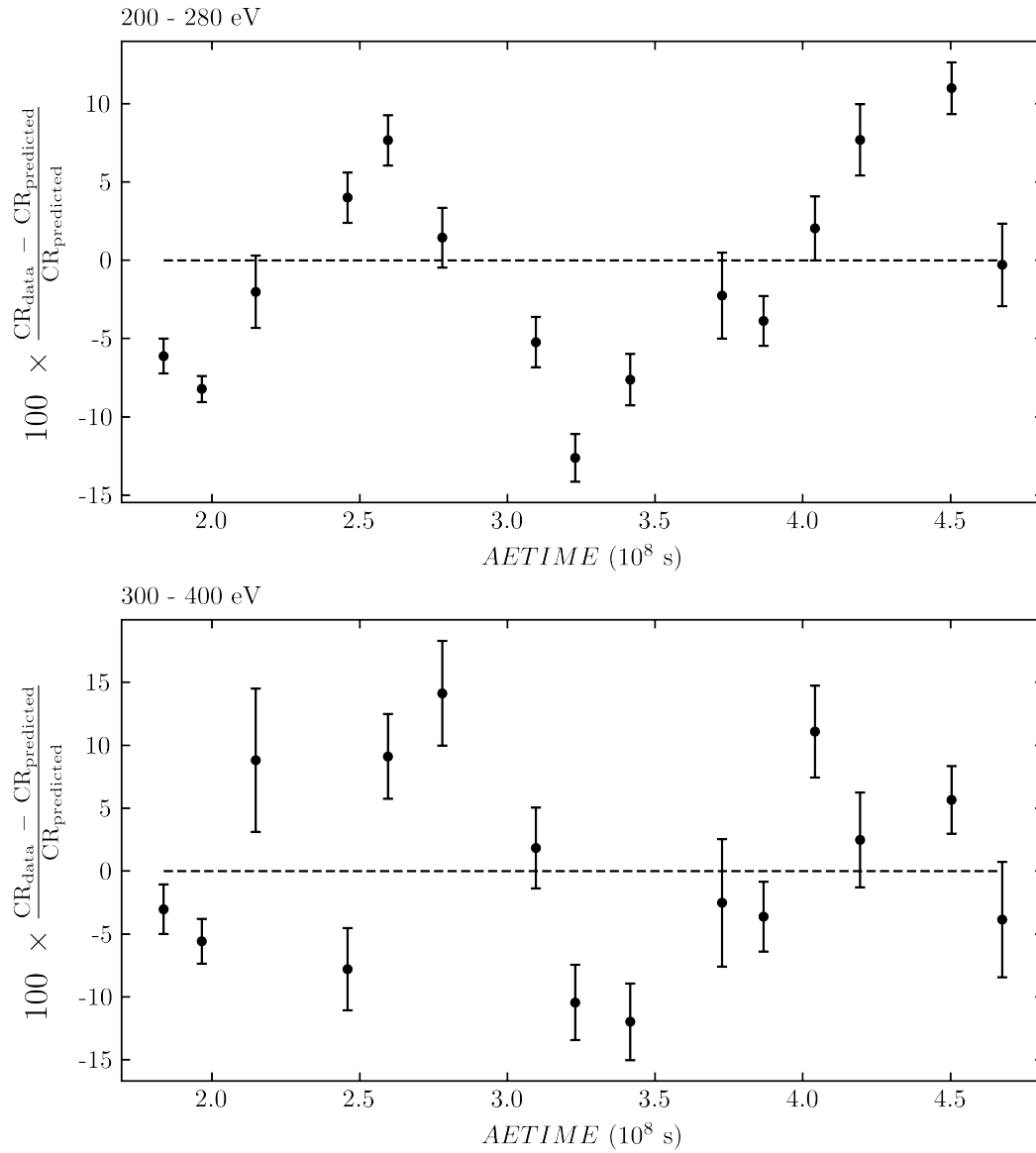


Fig. 4.13 Calibration uncertainties that has to be taken into account in the 200-280 eV (top) and 300-400 eV (bottom) energy ranges, from 2005 to 2014.

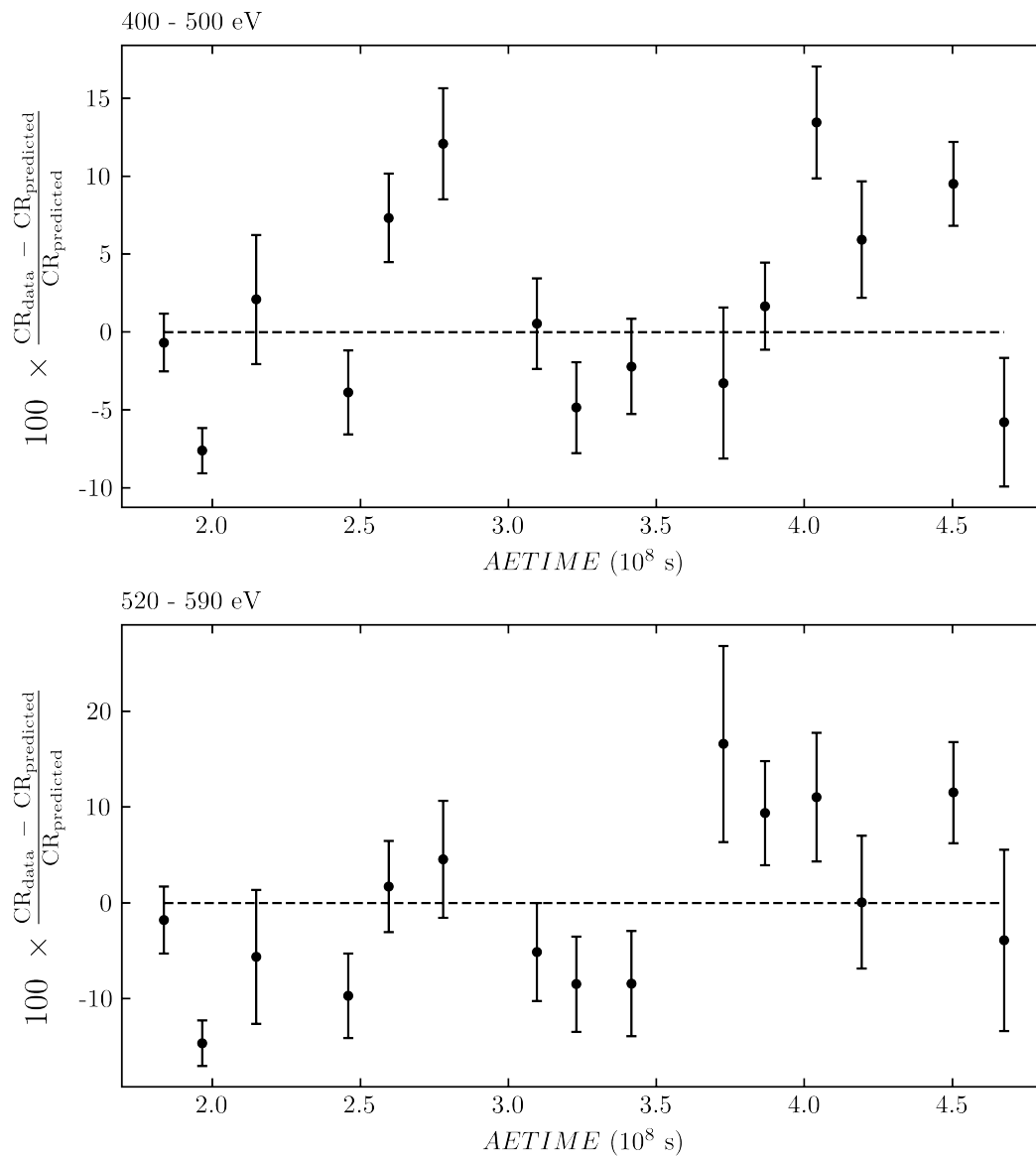


Fig. 4.14 Calibration uncertainties that has to be taken into account in the 400-500 eV (top) and 520-590 eV (bottom) energy ranges, from 2005 to 2014.

4.10 Discussion

To check our CNOS contamination model is applicable not only to RXJ1856 but also to other observations, we analyzed 1E0102-72.3 (hereafter E0102), known as one of the standard calibration sources in the 0.5-1.5 keV band. E0102 is a supernova remnant (SNR) having a relatively simple spectrum compared to a typical SNR spectrum. Strong, well-separated lines in the energy band from 0.5 to 1.5 keV make this source a useful calibration target for CCD instruments with moderate spectral resolution (e.g. Plucinsky, Paul P. et al. (2017)).

Suzaku observed E0102 74 times during the life of the mission. We selected 4 observations performed on December 17, 2005, April 10, 2007, April 23, 2009 and June 29, 2011. The exposure left after the data screening (with the same manner presented in Chapter 4) is ~ 25 ks for each observation. For spectral modeling, we refer the IACHEC (International Astronomical Consortium for High Energy Calibration) standard model presented in Plucinsky, Paul P. et al. (2017). We created response files with both HCNO and CNOS contamination models and compared folded spectra and the data. In both cases, the model for each year was simply folded through the response and no additional fitting was performed, in order to reveal differences between the contamination models rather than shortcomings of the IACHEC models.

The result is given in Fig. 4.15. In general, Residuals with CNOS model are more consistent with time compared to HCNO. The largest difference was around the oxygen K edge in 2007–2011. The CNOS model predicts $\sim 30\%$ higher count rate than the HCNO model. This actually improves the fit in E0102 around the O_{VII} emission line (e.g. in 2009), which has been a problem for a while (see Plucinsky, Paul P. et al. (2017)). We also checked an influence by the sulfur K edge around 2.5 keV and confirmed that differences between the HCNO and CNOS model are within statistical error and calibration uncertainty ($\pm 2\%$) over duration of mission.

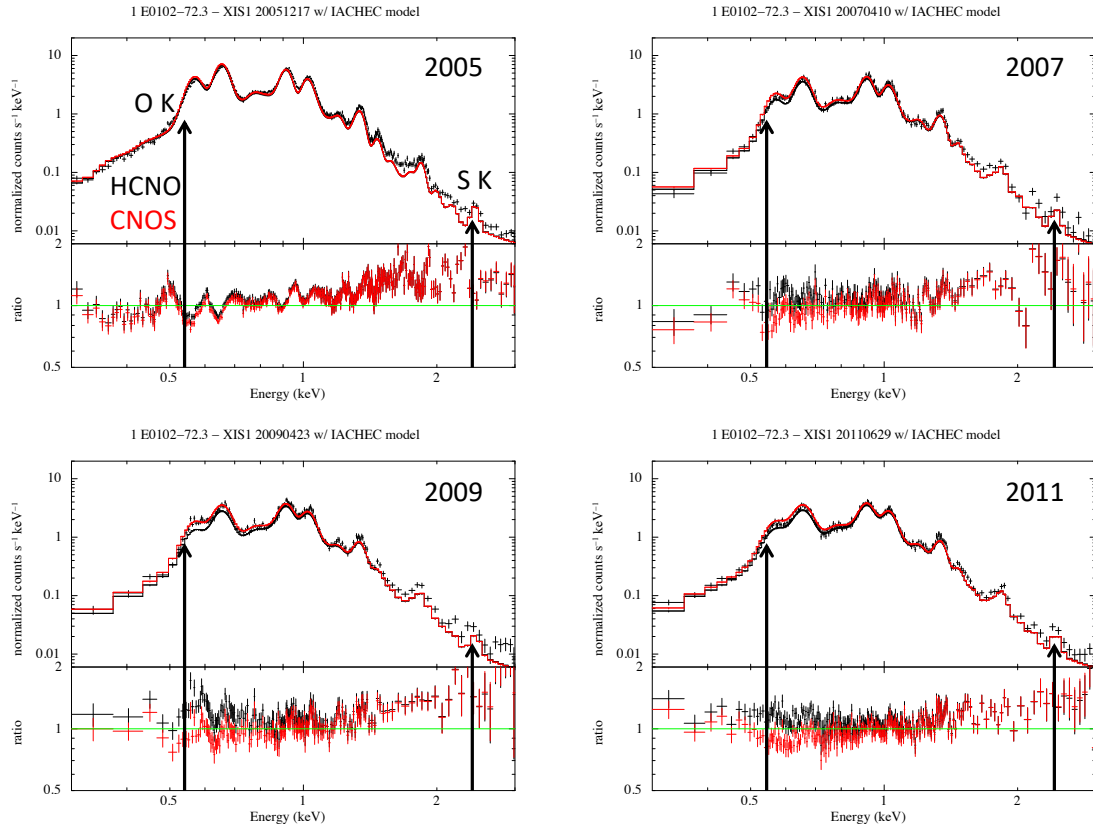


Fig. 4.15 Residual differences between the HCNO (black) and CNOS (red) contamination models with the E0102 spectra observed in 2005, 2007, 2009 and 2011. A systematic residue above ~ 1.5 keV for each data is because spectral fit is not performed, in order to reveal differences between the contamination models.

Chapter 5

Spectral Analysis of the Soft X-ray Diffuse Background in 0.2-2.0 keV

5.1 Purpose of Analysis

In order to deepen our understandings of the SXDB, we perform spectral analyses with *Suzaku* for the SXDB spectrum including the 1/4 keV band for the first time by using the calibration results shown in the preceding chapter. Since the SXDB is not a bright source and its surface brightness changes within a time scale of a year due to the H-SWCX emission, the keys for this analysis are long observational time and stationary observations over years. *Suzaku* observed the Lockman Hole field, known as a blank field without bright sources, regularly once a year from 2006 to 2014. This is the only ideal data set available to date for our purpose.

5.2 Observations and Data Reduction

Suzaku annually observed the Lockman Hole located at $(\alpha, \delta)/(l, b) = (162.94, 57.25)/(149.71, 53.21)$ from 2006 to 2014 for a calibration purpose of the Hard X-ray Detector (HXD). The Lockman Hole is known as a clear window that enables to observe distant objects, thanks to its very low absorbing hydrogen column density of $N_H = (5.6 - 5.8) \times 10^{19} \text{ cm}^2$ (Dickey and Lockman (1990), Hasinger et al. (1993) and Kalberla et al. (2005)). By using the *Suzaku* Lockman Hole data from 2006 to 2011, Yoshitake et al. (2013) analyzed time variability of the O_{VII} emission line at 570 eV and found that the intensities observed in 2010 and 2011 are enhanced compared to those of observed in 2006-2009. They suggested that this is due to the difference of characteristics of the H-SWCX emission related to the solar minimum and the maximum phases in Solar Cycle 24 (Fig. 5.1).

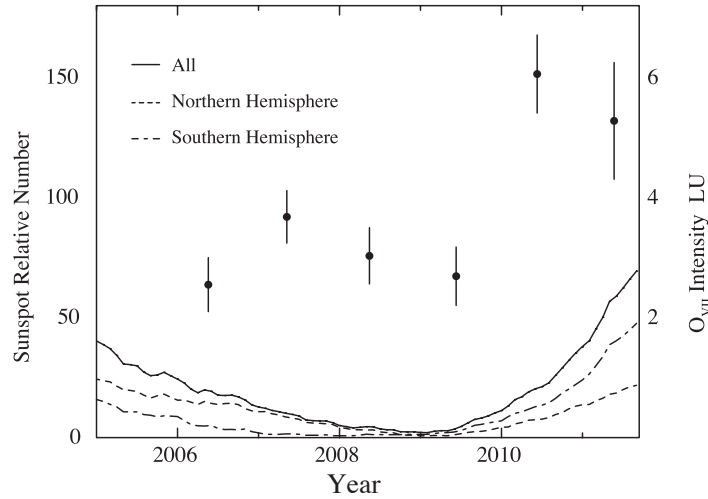


Fig. 5.1 A trend of the O_{VII} line intensities toward the Lockman Hole observed from 2006 till 2011. Dots with error bars (1σ) show O_{VII} intensities and lines indicate the relative sun spot number (Yoshitake et al. (2013)).

We used the whole CCD area, except two circular regions of diameters 3' and 4' in order to exclude point sources located at $(\alpha, \delta) = (162.811, 57.271)$ and $(\alpha, \delta) = (163.006, 57.176)$. We followed the data screening procedure described in Chapter 4. Only the difference was how we create ARF files. We applied our contamination growth curves (shown in Fig. 4.10) to calculate the QE for each observation. An uniform source of radius 20' was assumed for the ARF calculation because the SXDB emission is considered to be uniform in the *Suzaku* XIS1 field of view of $18' \times 18'$. We notice that an unusual bright region was found in the 0.1-0.2 keV band image in LH09 (shown in Fig. 5.2). This is not due to light leaking through the holes on the OBF because none of their locations correspond to this bright spot. This could be due to a failure of updating the dark level correction, although the exact cause is

unknown. The effect on the 1/4 keV flux due to this bright spot is considerably high about 20 %. This bright spot is located at the middle of the segment A on the CCD chip and the other area of this segment was also contaminated. We excluded the data from the segment A for LH09 in order to be on the safe side.

Unfortunately, the observational data for the last two years were highly contaminated by the solar scattered X-rays. We did not include them to our samples because we could obtain almost no exposure time after data screening. Our data set consists of the ones analyzed by Yoshitake et al. (2013) and one additional observation carried out in 2012. A summary of the observations is given in Table 5.1.

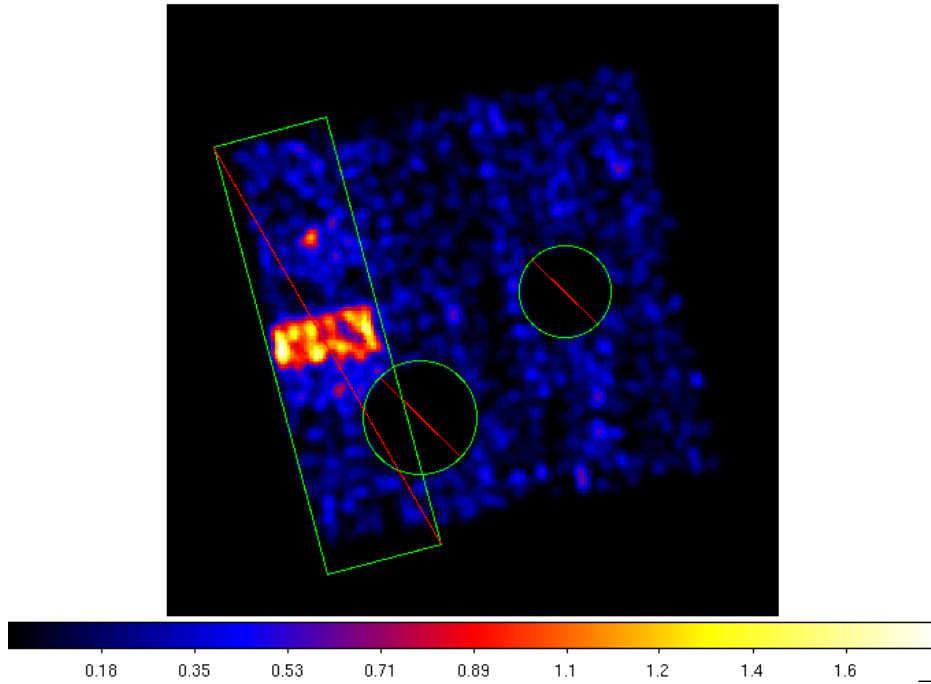


Fig. 5.2 An X-ray image in the 0.1-0.2 keV band for LH09. The vignetting effect is not corrected and the NXB is not subtracted. The areas enclosed by the solid green rectangle and circles was excluded from the data analysis. Point sources (indicated with the two circular regions) are removed from the image. An unusual bright region was detected in the middle of the most left column, or the segment A (indicated as the green rectangular box).

Table 5.1 *Suzaku* Observation log of the Lockman hole from 2006 until 2012. The nominal exposure is the exposure time left after the standard data processing. The usable exposure means the exposure time left after further data screening applied.

Abbreviation	Obs. ID	Start Date yyyy-mm-dd	Nominal Exposure ksec	Usable Exposure ksec	RA deg.	DEC deg.	Roll angle deg.
LH06	101002010	2006-05-17	80.4	25.4	162.937	57.256	281.872
LH07	102018010	2007-05-03	96.1	70.1	162.937	57.258	319.511
LH08	103009010	2008-05-18	83.4	58.3	162.937	57.255	281.530
LH09	104002010	2009-06-12	92.8	74.4	162.938	57.255	281.530
LH10	105003010	2010-06-11	80.0	48.6	162.937	57.251	279.887
LH11	106001010	2011-05-04	42.3	16.6	162.920	57.251	305.984
LH12	107001010	2012-05-05	36.0	16.1	162.920	57.255	318.695

We merged the data taken from 2006 to 2009 as LH06-09, and from 2010 to 2012 as LH10-12 by using the *mathpha* tool in order to increase photon statistics. We also merged the NXB for each group. The RMF and ARF for each data were multiplied to create so-called a response file by using the *marfrmf* tool. Then, the response files for each group were summed up, taking into account a weight which was determined as a ratio of the counting rate for each data in the 0.2-1 keV band. Figure 5.3 shows the data and NXB plot for each period. The NXB becomes dominant below ~ 0.12 keV and above ~ 5 keV. The signal-to-noise ratio in the energy range of 0.17-0.284 keV was 87 and 39 for LH06-09 and LH10-12 respectively. Fig. 5.4 shows the effective areas calculated for LH06-09 and LH10-12. The ratio of the area is also indicated with a solid blue line, showing that the difference is about $\sim 10\%$ in our target energy range of 0.17-2.0 keV.

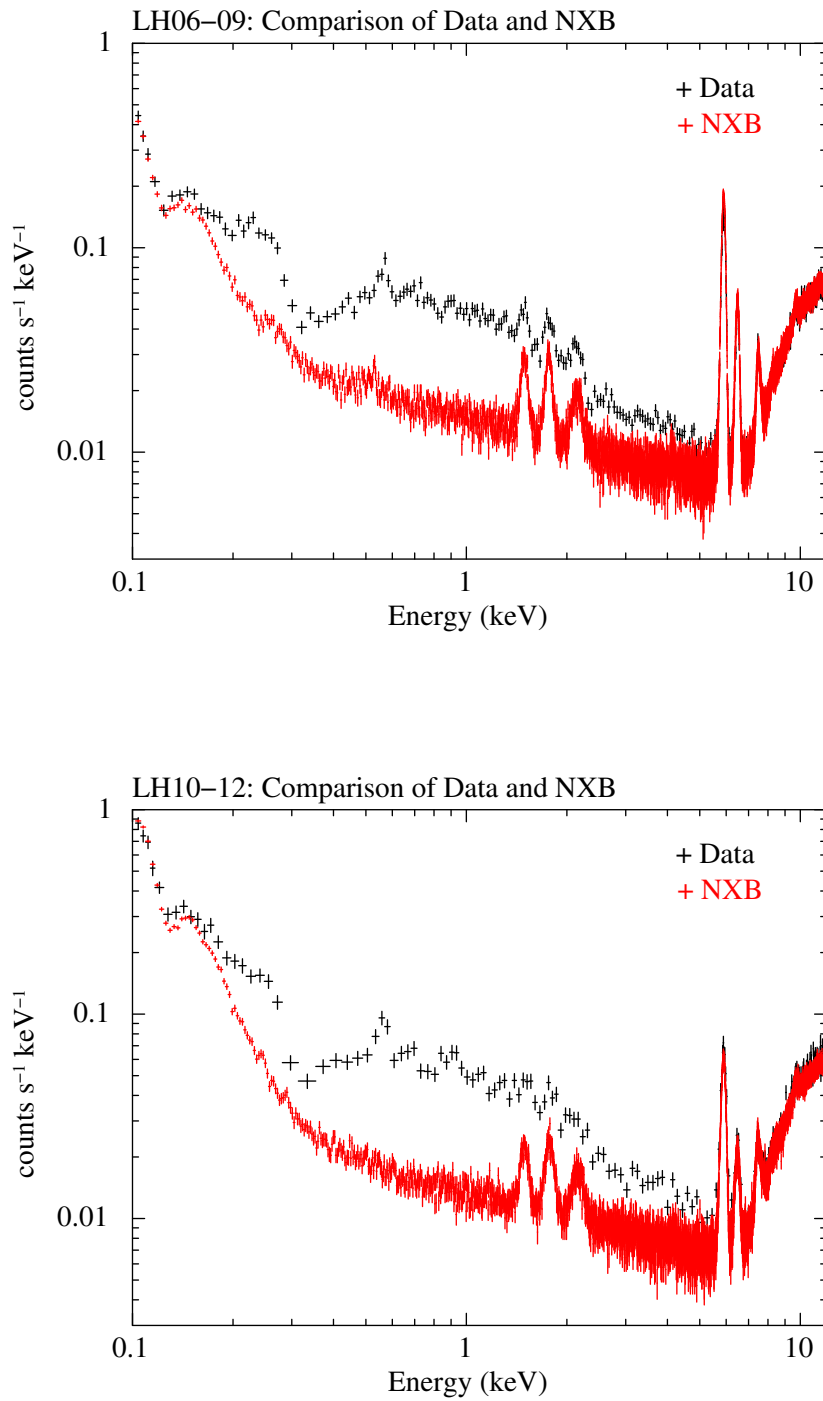


Fig. 5.3 Comparison of the processed data and NXB for LH06-09 (top) and LH10-12 (bottom). The NXB becomes dominant above ~ 5 keV. The signal-to-noise ratio at the 1/4 keV band (defined as the energy range of 0.17-0.284 keV) is 87 and 39 for LH06-09 and LH10-12, respectively.

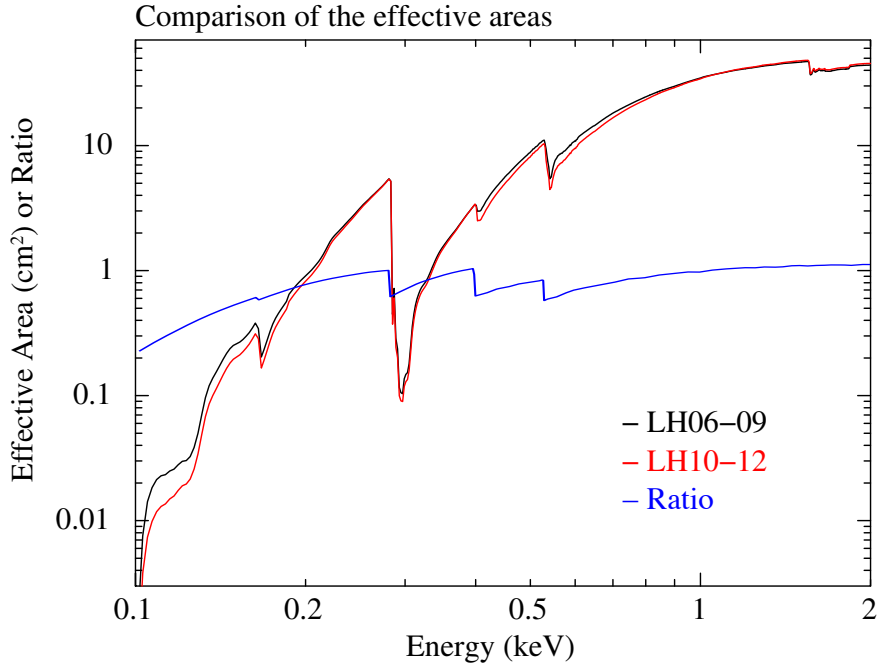


Fig. 5.4 Comparison of the effective areas from 0.1 to 2 keV for LH06-09 (black) and LH10-12 (red). The effective area for each spectrum was calculated based on the new contamination transmission developed in Chapter 4.

Figure 5.5 shows the NXB subtracted spectrum for each observational period (top panel) and the ratio of the spectra (shown on the panel in the middle). It is clear from the plot that the LH10-12 spectrum is enhanced by 20-60 % below ~ 1 keV compared to the LH06-09 spectrum. This cannot be explained by uncertainty in estimation of the effective area, because reproducibility of the effective area from 2005 to 2014 is within 10 % as presented in Chapter 4. Moreover, it seems that the enhancement especially at ~ 0.25 , $0.34-0.5$, ~ 0.56 , ~ 0.65 and ~ 0.9 keV are corresponding to some peaks predicted from a folded model by the XIS1 response based on the H-SWCX model (given by Koutroumpa et al. (2009), the model is plotted on the bottom panel in Fig. 5.5). This already indicates that at least the LH10-12 spectrum is "contaminated" with the H-SWCX emission over a wide range from 0.2 keV to 1 keV.

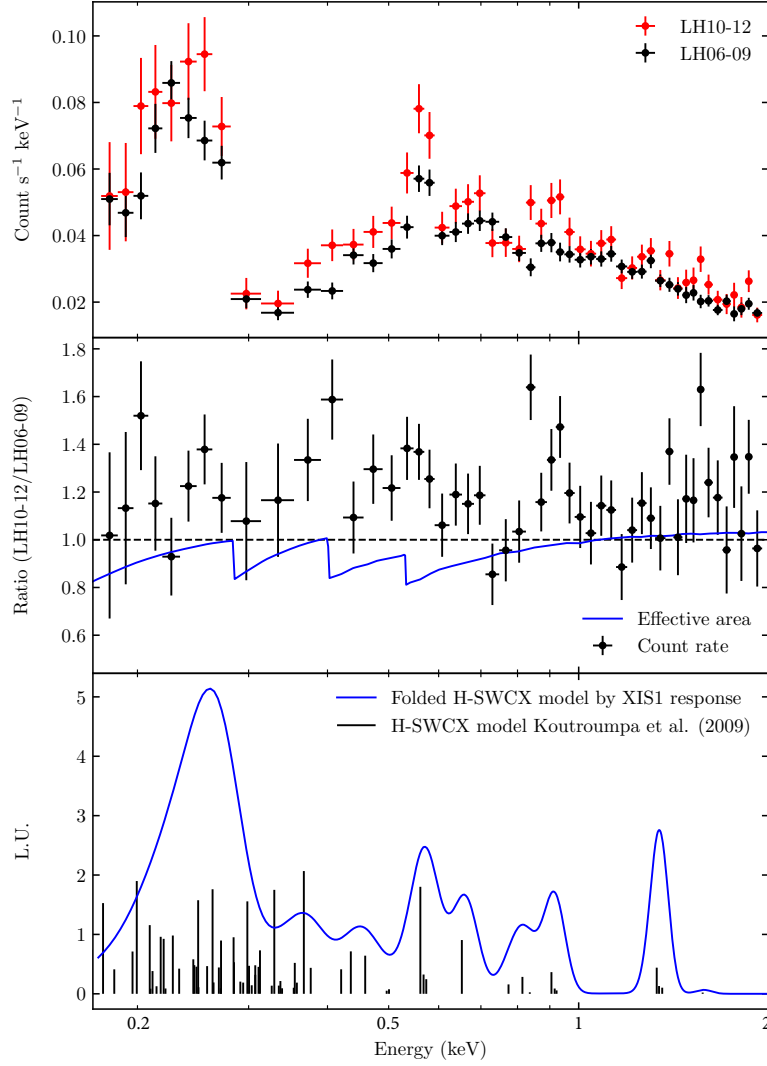


Fig. 5.5 Top panel: NXB subtracted spectra of LH06-09 (black) and LH10-12 (red). The energy bin size was determined to meet the minimum photon count of 150 cts for the LH10-12 data (before subtracting the NXB spectrum), Middle: Ratio of the spectra. The observed photon count rate in LH10-12 was simply divided by the one observed in LH06-09 for each bin. The plotted errors were calculated taking into account the error propagation. The ratio of the effective areas is also indicated with a blue solid line. Bottom: H-SWCX model predicted by Koutroumpa et al. (2009) (indicated with 103 black vertical lines) and the folded model by the XIS1 response (indicated with a blue solid line). The intensity is shown in units of LU (photons cm⁻² s⁻¹ sr⁻¹).

5.3 Spectral Modeling

In order to study the SXDB spectrum toward the Lockman Hole field, we considered 4 emission components, the CXB, Galactic halo, LB and H-SWCX. A description for each emission model is given as follows.

5.3.1 Extragalactic Component: CXB

The emission of the CXB is represented by double broken power-laws. Their photon indices are fixed at $\Gamma_1 = 1.96$ and $\Gamma_2 = 1.54$ below the folding energy at 1.2 keV, and $\Gamma_{1,2} = 1.4$ above it. Following Smith et al. (2007), the normalization of the broken power-law component with the photon index of $\Gamma_2 = 1.54$ is fixed at $5.7 \text{ photons s}^{-1} \text{ cm}^{-2} \text{ keV}^{-1} \text{ Sr}^{-1} @ 1 \text{ keV}$. The other one is a free parameter to adjust the field-to-field fluctuations of the brightness of the CXB. The CXB should be absorbed by the Galactic neutrals. We used phabs absorption model (Balucinska1992) with $N_H = 5.8 \times 10^{19} \text{ cm}^2$ (Kalberla et al. (2005)).

5.3.2 Galactic Component: Hot Galactic Halo

We modeled the halo emission with a single-temperature *APEC* thermal plasma model¹ assuming collisional ionization equilibrium (CIE) with AtomDB² ver. 3.0.8. The temperature and normalization were free parameters. The halo component is considered to be absorbed by the Galactic neutrals. We used the same absorption model described in the subsection of the CXB modeling.

5.3.3 Local Component 1: Hot Gas in the LB

The LB emission was modeled with an *APEC* thermal plasma model same as the Galactic halo model. The temperature and normalization were free parameters. Historically, a thermal plasma model with a temperature of 0.1 keV has often been used to model the LB + H-SWCX emission. In this thesis, we explicitly separate these two components to study the origin of the SXDB especially in the 1/4 keV band.

5.3.4 Local Component 2: H-SWCX Line Emissions

Calculating an accurate and complete emission model for the H-SWCX spectrum has been long considered. However for examples, due to the difficulty of cross section calculations and

¹<https://heasarc.gsfc.nasa.gov/xanadu/xspec/manual/node134.html>

²<http://atomdb.org>

the vast number of ions and energy levels, it is still difficult to build such a completed model. Nevertheless, there is one approximate model based on the AtomDB Charge Exchange code (ACX; see Smith et al. (2014)) is available in *XSPEC*. The ACX model tracks the emission resulting from radiative decays of the ions using detailed calculations of the ionic structure (e.g. Fig. 5.6, showing for the He-like case). When an electron is exchanged onto a highly excited level of an ion, the electron decays towards the ground state radiating photons at each step. The relative strengths of emission lines from different ions are controlled via an ionization temperature parameter assuming CIE. This temperature was treated as a free parameter in the fitting. We used the nominal and favored setting for the H-SWCX emission, i.e., `swcx=1` and `model=8` (meaning that captured electrons are distributed between the two nearest n shells to the most-probable shell, and that the separable distribution is used for the l levels; see Smith et al. (2014) and a model description³ for more details).

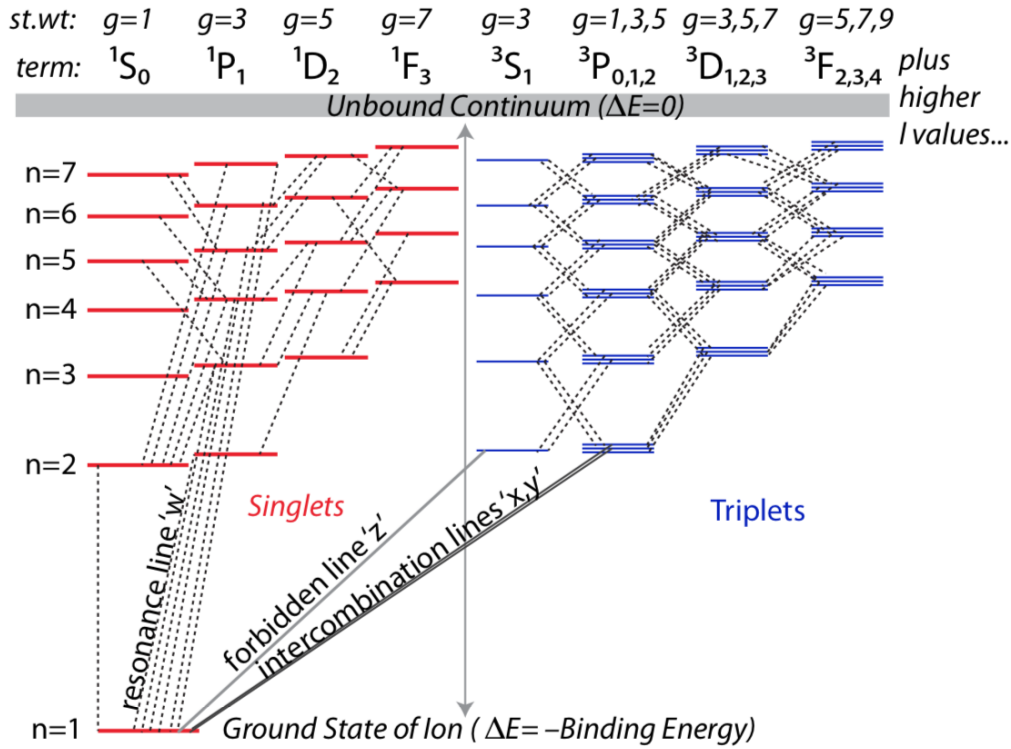


Fig. 5.6 Schematic Grotrian diagram for a helium-like ion with selected radiative (downward) transitions. Taken from Smith et al. (2014).

Figure 5.7 shows the ACX model in the 0.17-1 keV band with the temperature of 0.05 (red), 0.1 (green), 0.15 (blue) and 0.2 keV (cyan), folded with the *Suzaku* XIS1 response. For

³http://www.atomdb.org/CX/acx_manual.pdf

comparison, the APEC thermal plasma model with the temperature of 0.1 keV (magenta) is also plotted as a typical LB model. The flux for each model is adjusted to be roughly matched each other around the O_{VII} emission line. The ACX models with the temperature from 0.15 to 0.2 keV is considered to be a typical H-SWCX spectrum and in this case, the ACX model predicts about 20 times smaller flux at the 1/4 keV band, compared to the LB model. On the other hand, the ACX models with the temperature of 0.05 and 0.1 keV predict more flux in the 1/4 keV band. However in these spectra, the flux in 0.3-0.5 keV (contributed by C_{VI} $Ly\alpha$, C_{VI} $Ly\beta$, γ , δ and N_{VI} $K\alpha$ f, i, r lines) becomes significant than O_{VII} line, which looks very different from the H-SWCX spectrum that has been studied so far.

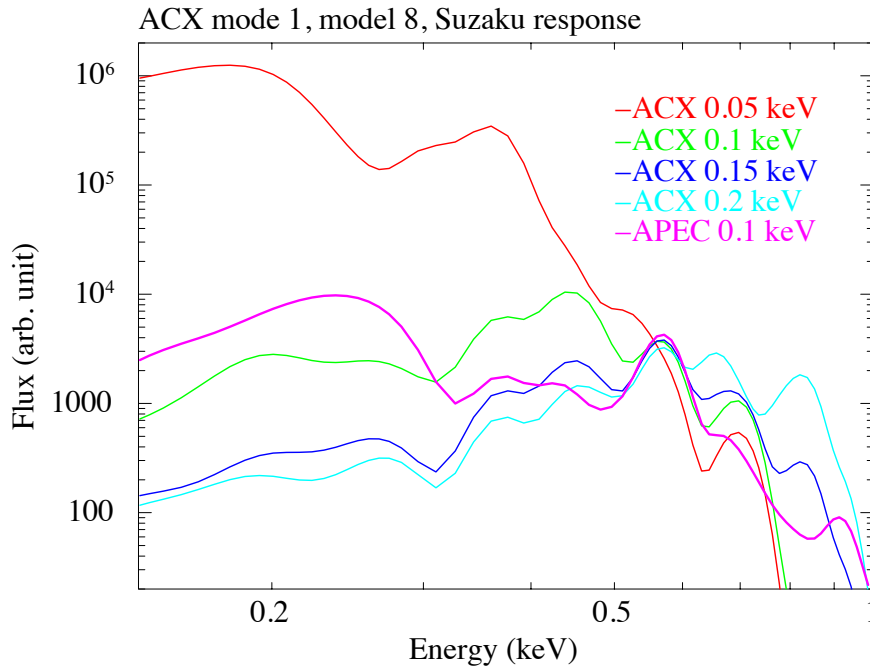


Fig. 5.7 Temperature dependence of the ACX model in the 0.17-1 keV band. The APEC model with the temperature of 0.1 keV is also plotted (magenta) for comparison. The flux is for each model is adjusted to be roughly matched each other around the O_{VII} emission line.

5.4 Spectral Analysis Results

5.4.1 Investigation of the Origin of the Local Emission

As we mentioned in the earlier subsection, it is obvious that the H-SWCX emission contributes at least to the LH10-12 spectrum, in comparison with the LH06-09 spectrum (see Fig. 5.5). Therefore, our interest here is the origin of the local emission in the LH06-09 spectrum. The LH06-09 spectrum presented in Fig. 5.5 shows a significant flux at the 1/4 keV band, already suggesting that the emission from the LB seems to be dominant as the local emission component rather than the H-SWCX emission (see the model comparison in Fig. 5.7).

we analyzed the LH06-09 spectrum with the SXDB spectral model consisting of the CXB, hot ISM and LB. The spectral fit result and the spectrum along with the best fit parameter are presented in Table 5.2 and Fig. 5.9, respectively. In general, fit is acceptable enough with $\chi^2/\text{d.o.f} = 97.1/87$, showing no more spectral component is required to explain the observed spectrum. The confidence contour of the LB vs. ISM temperature is given in Fig. 5.8. The temperature of the LB and ISM are determined as 0.093 (0.06 - 0.13) keV and 0.18 (0.14 - 0.24) keV, respectively. These values naturally fit into the picture of the SXDB emerged from studies that have been done in the past, presumptively indicating the H-SWCX emission does not contribute so much to the SXDB spectrum when the Solar activity is minimum, at least towards the Lockman Hole field.

Table 5.2 Spectral fit result of the LH06-09 spectrum with the LB model.

LB		Galactic Halo				CXB			Gain		$\chi^2/\text{d.o.f}$
kT	norm.	N_H	kT	norm.	N_H	Γ_1	norm ₁	Γ_2	norm ₂	offset	
keV	(1)	(10^{20} cm^2)	(keV)	(1)	(10^{20} cm^2)		(2)		(2)	(eV)	
$0.093^{+0.02}_{-0.03}$	$10.4^{+14.0}_{-3.3}$	0.58^f	$0.18^{+0.03}_{-0.03}$	$4.9^{+3.9}_{-1.1}$	0.58^f	1.96^f	$3.8^{+0.2}_{-0.3}$	1.54^f	5.7^f	-7^{+2}_{-2}	97.1/87

Note Errors quoted in this table are the 90 % confidence intervals.

^f Fixed parameter.

(¹) The emission measure integrated over the line of sight, $(1/4\pi) \int n_e n_H ds$ in the unit of $10^{14} \text{ cm}^{-5} \text{ Sr}^{-1}$.

(²) photons $\text{s}^{-1} \text{ cm}^{-2} \text{ keV}^{-1} \text{ Sr}^{-1}$ @ 1 keV.

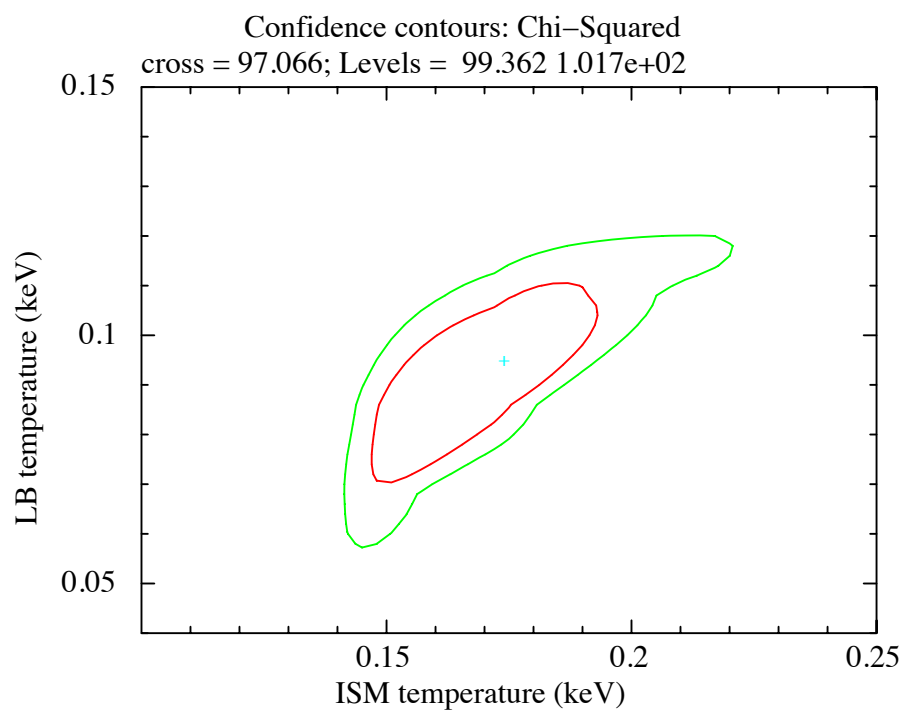


Fig. 5.8 68 % (red) and 90 % (green) confidence contours of the LB temperature vs. the ISM temperature for the LB SXDB model given in Table 5.2.

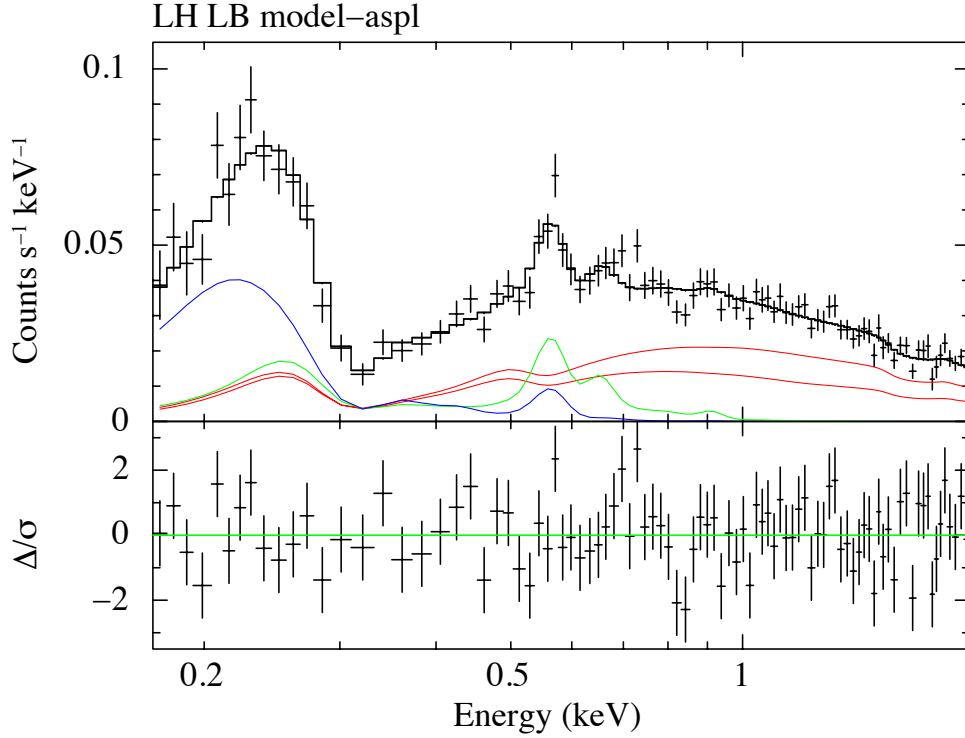


Fig. 5.9 Spectral fit result of the LH06-09 spectrum. Top panel: The NXB subtracted data is shown as the black crossed points and best fit curve folded by the detector response is indicated with a black solid line. The LB, galactic halo and CXB components with the best fit parameters (Table 5.2) are indicated with blue, green and red solid lines respectively. Bottom panel: Residual plot defined as the data minus best fit model.

Next, we evaluated the likely contribution of the H-SWCX emission to the LH06-09 spectrum, by replacing the LB model to the ACX model. The spectral fit result and the spectrum along with the best fit parameter are presented in Table 5.3 and Fig. 5.10, respectively. Fit is marginally acceptable with $\chi^2/\text{d.o.f} = 107.9/87$. However, the temperature of the ACX model is very low ~ 0.02 (< 0.05) keV and its flux only contributes very little to the spectrum at the 1/4 keV band. The ISM temperature of 0.125 (0.118-0.131) keV seems also very low as the Galactic halo component. Therefore, it is difficult to consider that this spectral model represents nature of the SXDB. We also performed spectral fit while fixing the ISM temperature at 0.177 keV (which was obtained from the fit with the LB model), forcing the ACX model to produce as much emission as possible especially at the 1/4 keV

band. However, the result presented in Fig. 5.11 clearly shows that the ACX model cannot explain the 1/4 keV emission.

Table 5.3 Spectral fit result of the LH06-09 spectrum with the ACX model.

ACX		Galactic Halo				CXB				Gain	$\chi^2/\text{d.o.f}$
kT	norm.	N_H	kT	norm.	N_H	Γ_1	norm ₁	Γ_2	norm ₂	offset	
keV	(1)	(10^{20} cm^2)	(keV)	(2)	(10^{20} cm^2)		(3)		(3)	(eV)	
0.02(< 0.05)	$0.15^{+11}_{-0.13}$	0.58^f	$0.125^{+0.006}_{-0.007}$	$11.9^{+1.1}_{-1.5}$	0.58^f	1.96^f	$3.8^{+0.2}_{-0.3}$	1.54^f	5.7^f	-7^{+2}_{-2}	107.9/87

Note Errors quoted in this table are the 90 % confidence intervals.

^f Fixed parameter.

(1) This parameter is just a scaling factor and no physical meaning.

(2) The emission measure integrated over the line of sight, $(1/4\pi) \int n_e n_H ds$ in the unit of $10^{14} \text{ cm}^{-5} \text{ Sr}^{-1}$.

(3) photons $\text{s}^{-1} \text{ cm}^{-2} \text{ keV}^{-1} \text{ Sr}^{-1}$ @ 1 keV.

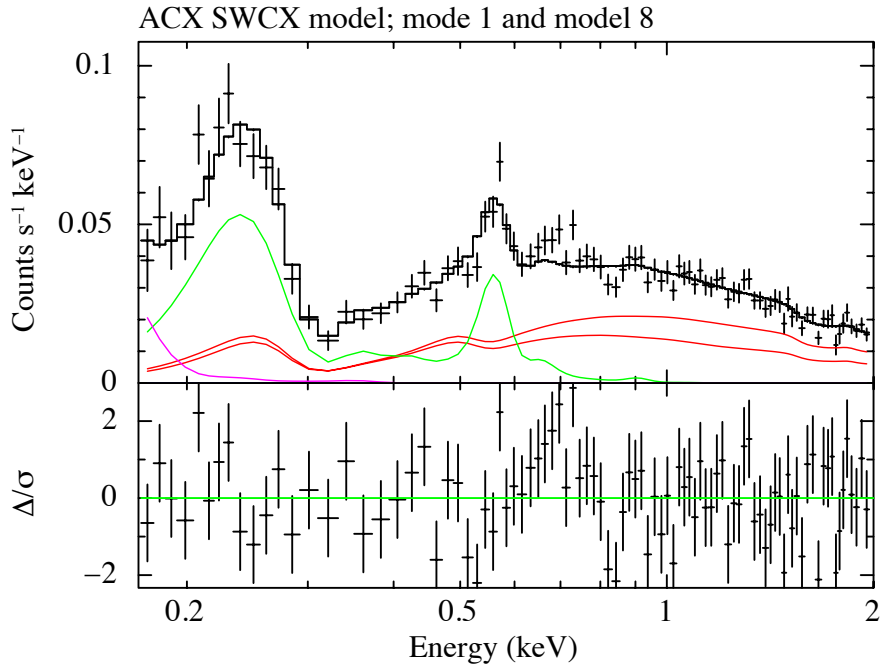


Fig. 5.10 Spectral fit result of the LH06-09 spectrum. Top panel: The NXB subtracted data is shown as the black crossed points and the best fit curve folded by the detector response is indicated with a black solid line. The H-SWCX (ACX model), Galactic halo and CXB components with the best fit parameters (Table 5.3) are indicated with magenta, green and red solid lines, respectively. Bottom panel: Residual plot defined as the data minus best fit model.

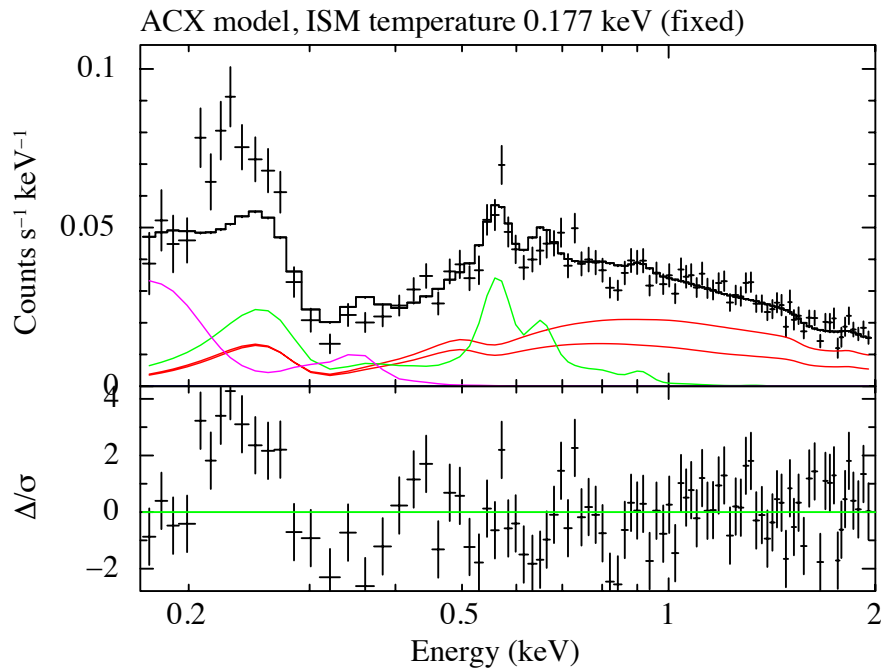


Fig. 5.11 Same as Fig. 5.10 but the ISM temperature is fixed at the best fit values of 0.177 keV obtained from the spectral fit with the LB model (presented in Table 5.2). The temperature of the ACX model is a free parameter.

In short summary, the SXDB spectrum including the 1/4 keV band, observed in the solar minimum period toward the Lockman Hole field, is well reproduced by the emission model consisting of the LB, hot ISM and CXB. We also employed the ACX model instead of the LB and found that the LB model cannot be replaced by the ACX model, indicating the local emission of the observed spectrum is dominated by the LB. Otherwise, the ACX model should be totally wrong.

5.4.2 Characterization of the excess emission in the LH10-12 spectrum

The systematic brightening below 1 keV in the LH10-12 spectrum relative to the LH 06-09 spectrum is considered to be influenced by the H-SWCX emission. In this subsection, we perform spectral fit to the enhanced spectrum and characterize properties of the H-SWCX emission.

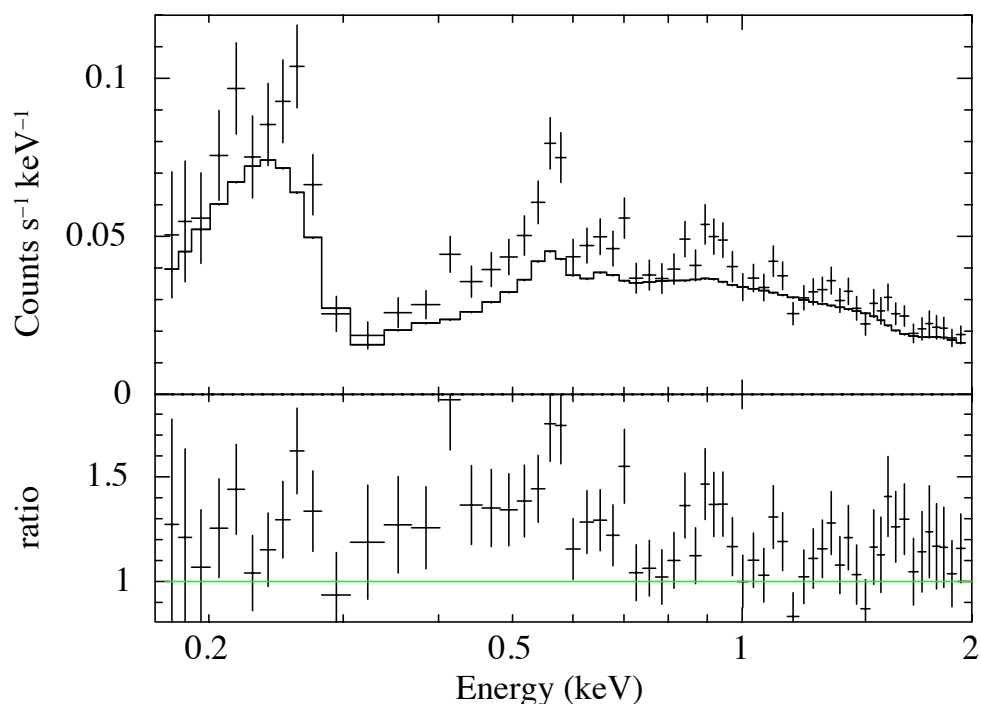


Fig. 5.12 The LH10-12 spectrum along with the base model (Table 5.2) folded by the XIS1 response for LH10-12. A clear enhancement can be seen below 1 keV.

Figure 5.12 shows the LH10-12 spectrum along with the LB SXDB model. In order to perform spectral fit to the residual spectrum subtracted the model, we used the LB SXDB model as a "baseline" model (all parameters are fixed at the best fit values) and added the ACX model. Figure 5.13 shows a fit result with the ACX model (the temperature and normalization are free parameters). The red solid line indicates the best fit model with the temperature of 0.17 (0.16-0.18) keV ($\chi^2/\text{d.o.f} = 86.4/60$). The model well reproduces the enhanced spectrum in 0.3-0.7 keV. However, systematic residues remain especially at the 1/4 keV band and around 0.9 keV. Furthermore, we added another ACX model to explain these residues but fit did not improve and one of the two ACX components was poorly constrained. These results probably imply a limitation of the ACX model. The ACX model may have to be used with caution when characterizing the SWCX induced emission.

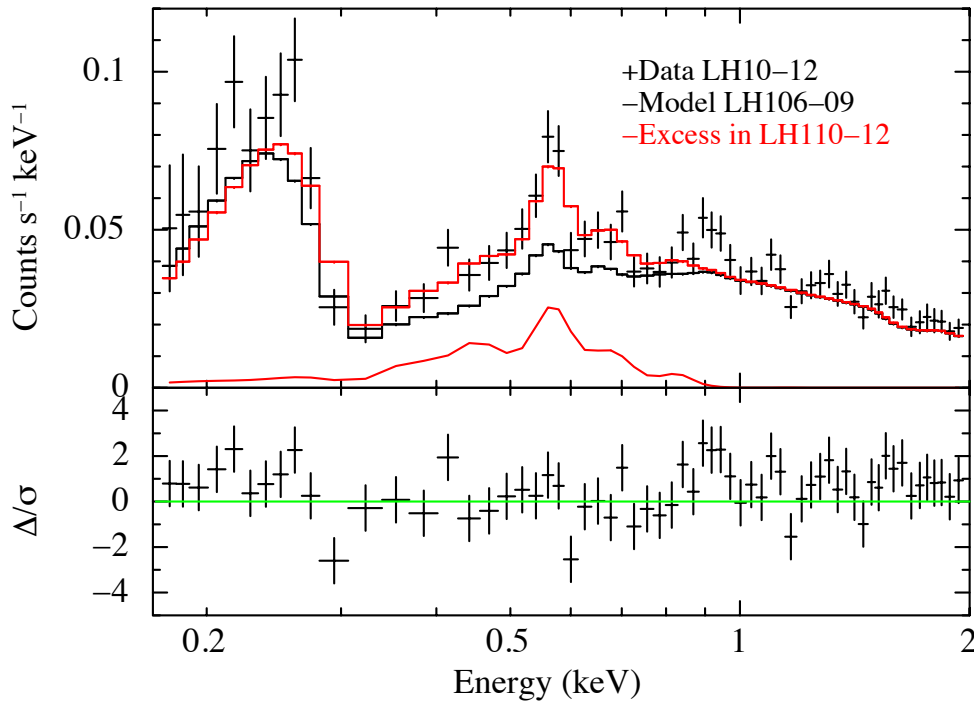


Fig. 5.13 The SWCX-contributed spectrum along with the ACX model (solid red line). The black solid line indicates the LB model derived from the LH06-09 spectrum.

Since there is no alternative H-SWCX model is available in public, we decided to investigate an emission spectrum using the theoretical calculation result presented in Koutroumpa et al. (2009) (see 2.10 given in the review chapter.). This spectrum is derived from various theoretical calculations on cross sections with carefully selected abundances for the slow solar wind. This is convenient for us because it is considered that the slow wind dominated the fast solar wind in the whole sky in the solar maximum period⁴.

We read 103 emission lines in 0.17-2 keV from Fig. 2.10. As it is shown in Fig. 5.5, the spectrum consisting of superposition of the 103 zero-width Gaussian lines can be reproduced with representative peaks under the *Suzamu* limited spectral resolutions.. To determine the energy and intensity for these lines, we performed observation simulations with this model. A simulation result assuming a typical exposure time of 200 ksec is given in Fig. 5.14. The mock spectrum is well reproduced with 9 zero-width Gaussian lines. We determined the central energies as 219.3, 267.3, 362.3 449.9 566.8, 658.7, 805.6, 911.6 and 1340.1 eV, based on the simulations of 1000 times. The simulation results are summarized in Appendix B.1.

We performed spectral fit with this this Gaussian model to examine the enhanced spectrum in more details. The central energies were fixed while their intensities were free parameters. The spectral fit result is presented in Table 5.4 and the spectrum along with the best fit model is given in Fig. 5.16. The spectral fit is acceptable with $\chi^2/\text{d.o.f} = 57.3/53$ and the excess emission is reproduced better than the ACX model. Especially Ne_{IX} K α at 911.6 eV well explains the enhancement around 900 eV, which cannot be reproduced with the ACX model. Moreover, there is a good agreement in the intensity between the model and observation. Figure 5.16 shows comparison of the line intensities between the model and observation. The intensities are normalized by the ones for O_{VII} K α . The Gaussian model predicts significantly higher intensities below 0.4 keV and Mg_{XI} K α at 1.34 keV, in contrast to the fit result with the ACX model. It seems that the both models have uncertainties in the line intensities from heavier ions such as Si, S, Mg and Fe. However, it is worth mentioning that in general there is a good agreement between the observation and Koutroumpa et al. (2009) for the lines from C, N, O and Ne located in 0.4-1 keV. This agreement between the model and observation might indicate that the observed spectrum is the H-SWCX emission itself, not a certain fraction of the H-SWCX, indirectly implying that the H-SWCX contribution to the LH06-09 spectrum is minimal. We will discuss on contribution from the heavier ions in 5.6.2.

⁴Note that in Koutroumpa et al. (2009), they do not calculate the H-SWCX spectrum for the fast solar wind, which seems to dominate the slow solar wind toward the Lockman Hole direction in the solar minimum period.

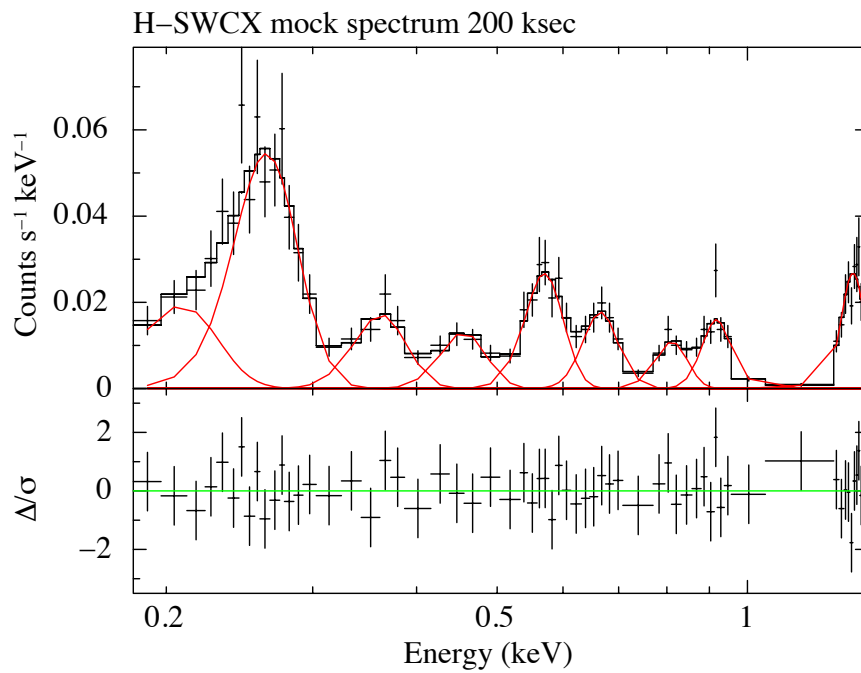


Fig. 5.14 A typical spectral fit result to the mock spectrum produced from the 103 H-SWCX induced emission lines taken from Koutroumpa et al. (2009). The solid red lines indicate the Gaussian models whose width were fixed at zero but the line center energies and normalizations were free. 9 Gaussian lines well reproduced the mock spectrum created by assuming the typical exposure time of 200 ksec.

Table 5.4 Spectral fit result with the simulated Gaussian model based on the H-SWCX emission lines calculated by Koutroumpa et al. (2009). The predicted emission lines for the 219, 267 and 362 eV give an idea of what sort of ions contribute to those lines.

Predicted emission lines	H-SWCX Gaussian Model		Observation
	Central Energy (eV)	Intensity (L.U.)	Intensity (L.U.)
Si _{VIII,IX,X} , Mg _{VIII,IX,X} , Fe _{IX,X,XI}	219.3	9.6	4.5 (< 9.4)
Si _{VIII,IX,X} , Mg _{VIII,IX,X} , Fe _{IX,X,XI}	267.3	5.2	$2.3^{+1.5}_{-1.2}$
Si _{IX} , S _{IX} , C _{VI} Ly α	362.3	5.2	1.8 (< 3.8)
C _{VI} Ly β , γ , δ , N _{VI} K α f, i, r	449.0	1.9	$2.1^{+0.9}_{-0.9}$
O _{VII} K α f, i, r	566.8	2.5	$2.9^{+0.7}_{-0.7}$
O _{VIII} Ly α , O _{VII} K β , γ , ϵ	658.7	0.9	$0.66^{+0.33}_{-0.34}$
O _{VIII} Ly γ	805.6	0.41	0.16 < 0.3
Ne _{IX} K α	911.6	0.51	$0.47^{+0.17}_{-0.16}$
Mg _{XI} K α	1340.1	0.63	0.1 (< 0.2)
Gain offset (eV)			-7^{+4}_{-5}
$\chi^2/\text{d.o.f}$			57.3/53

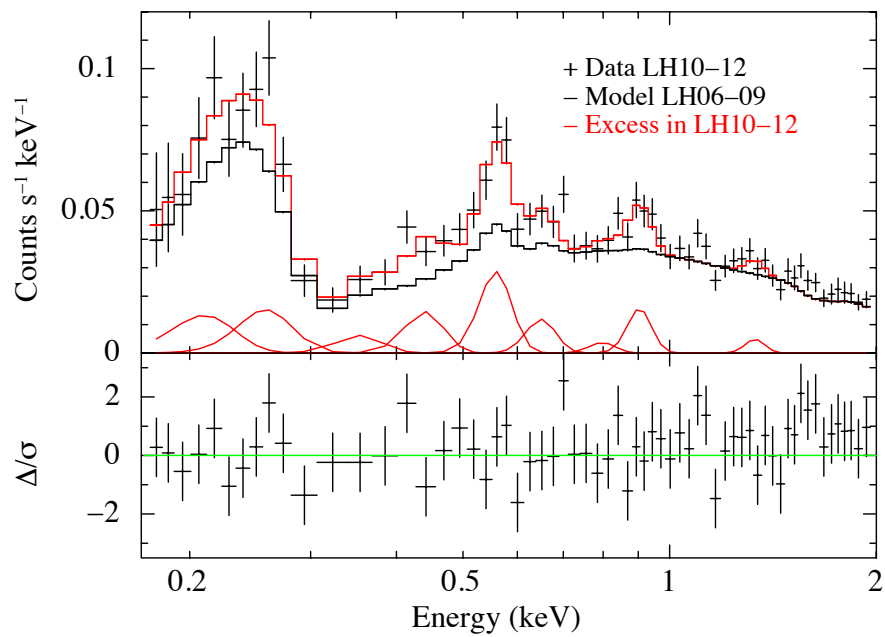


Fig. 5.15 Spectral fit to the SWCX-contributed emission with the Gaussian line model described in Table 5.4. The black solid line indicates the LB model derived from the LH06-09 spectrum.

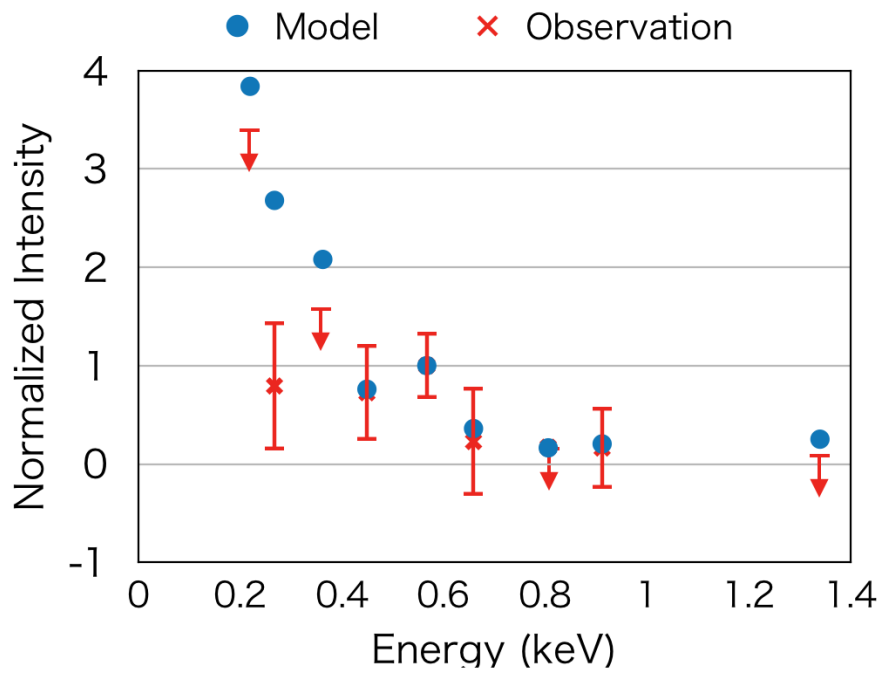


Fig. 5.16 Comparison of the intensity for each emission line between the observation and the Gaussian H-SWCX model. The intensities are normalized by the ones for O_{VII} $K\alpha$ located at 567 eV. The error bars indicate 90 % statistical error range (The error for the O_{VII} $K\alpha$ is propagated to calculate the errors for line ratios).

5.5 Systematic Errors

We investigated systematic uncertainties possibly affecting the physical parameters derived from the spectral analyses. Table 5.5 shows a list of the uncertainties we checked. For each uncertainty, changes in the LB temperature and normalization are given as the most sensitive parameters to the systematics. Basically, all the systematic errors we considered fell within 90 % statistical errors presented in Table 5.2. The reproducibilities for the response below 1 keV and NXB are fairly considered to be $\pm 10\%$ and $\pm 5\%$, respectively. For the neutral column density toward the Lockman Hole field, we estimated the uncertainty to be $\pm 10\%$, derived from fluctuation in the Galactic HI (available from Leiden/Argentine/Bonn LAB Survey, Kalberla et al. (2005)) across a 1 square degree sky area centered on the Lockman Hole field. The CXB spectral shape below 1.2 keV is a subject to be considered, because more fainter point-like sources have been detected since Smith et al. (2007) in the Chandra deep observation campaign and these new sources can affect the slope of the CXB spectrum especially on the low energy side. We used the latest faint point source catalogue presented in Luo et al. (2016) and accumulated spectra which are defined as the soft-hard band ratios as a function of the full-band flux. We estimated the soft band slope of 2.3 instead of 1.96 with the break energy of 1.2 keV as an upper limit. In order to check uncertainty related to the abundance table, we tested two different solar abundance tables given by Anders and Grevesse (1989) and Lodders (2003).

Table 5.5 Summary of the systematic uncertainties investigated for the temperature and normalization obtained with spectral fit to the LH06-09 spectrum.

Systematic uncertainty		LB best fit parameters	
		Temperature (keV)	Normalization (1)
Response below 1 keV	+10 %	0.099	9.2
	−10 %	0.086	11.6
NXB	+5 %	0.100	9.1
	−5 %	0.095	11.2
H _I absorption column density	+10 %	0.098	10.5
	−10 %	0.097	10.4
CXB index below 1.2 keV	2.3	0.101	8.7
Abundance table	Anders and Grevesse (1989)	0.101	9.2
	Lodders (2003)	0.096	9.6

⁽¹⁾ The emission measure integrated over the line of sight, $(1/4\pi) \int n_e n_H ds$ in the unit of $10^{14} \text{ cm}^{-5} \text{ Sr}^{-1}$.

5.6 Discussion

5.6.1 Possible H-SWCX detection at ~ 0.7 keV

It might be just an artificial structure, the residual plot presented in Fig. 5.9 seems to suggest possible existence of a line-like emission component. We performed spectral fit by adding a Gaussian line with a natural width of zero to the LB SXDB model. The result is summarized in Table 5.6 and the orange thick line presented in Fig. 5.17 shows the Gaussian model. Fit is improved with $\chi^2/\text{d.o.f} = 89.2/85$ compared to the LB SXDB model. The central energy and intensity of the line are determined as 0.716 (0.686-0.746) keV and 0.27 (0.1-0.44) LU, respectively.

This emission line could be explained by the SWCX induced emission corresponding to $\text{O}_{\text{VII}} \text{K}_\gamma$ (0.698 keV), $\text{O}_{\text{VII}} \text{K}_\delta$ (0.713 keV) and $\text{O}_{\text{VII}} \text{K}_\epsilon$ (0.721 keV) lines. However, these lines are predicted to be very weak compared to the $\text{O}_{\text{VII}} \text{K}$ line (triplet). Koutroumpa et al. (2009) suggested there is no contribution from these lines to the H-SWCX emission (see the bottom panel in Fig. 5.5). The ACX model does predict lines around 0.7 keV and the total intensity from those lines is about one fourth of the $\text{O}_{\text{VII}} \text{K}$ triplet line (see Fig. 5.7). However, this seems to be quite overestimated regarding Henley and Shelton (2015). They performed X-ray shadowing measurements toward 6 different line-of-sights to test several foreground emission models and found that only the ACX model is inconsistent from the others, mainly due to issues on spectral fit caused by the strong lines around 0.7 keV. We quote Cumbee et al. (2014) for more quantitative discussion. They attempted to account for an anomalously enhanced X-ray flux around 0.7 keV observed in the rim of the Cygnus Loop, by introducing the charge exchange induced lines. They estimated that the sum of the intensities of $\text{O}_{\text{VII}} \text{K}_\gamma$, $\text{O}_{\text{VII}} \text{K}_\delta$ and $\text{O}_{\text{VII}} \text{K}_\epsilon$ lines are more than 30 times lower compared to the one from the $\text{O}_{\text{VII}} \text{K}$ triplet line. We measured about 0.3 LU for the 0.7 keV line, resulting 9 LU is required for the $\text{O}_{\text{VII}} \text{K}$ triplet line which is not realistic considering the LH06-09 spectrum fit results. We note that the relative intensity observed by Cumbee et al. (2014) can be different from the one for the H-SWCX emission. However, taken together with the discussions above, most probably the 0.7 keV line-like emission is not originated in the SWCX mechanism.

Table 5.6 Spectral fit result of the LH06-09 spectrum with the LB model.

LB		Galactic Halo				CXB				Line		Gain	$\chi^2/\text{d.o.f}$
kT	norm.	N_H	kT	norm.	N_H	Γ_1	norm ₁	Γ_2	norm ₂	E_c	I	offset	
(keV)	(1)	(10^{20} cm^2)	(keV)	(1)	(10^{20} cm^2)		(2)		(2)	(keV)	(L.U.)	(eV)	
$0.085^{+0.03}_{-0.03}$	$10.4^{+14.0}_{-3.3}$	0.58^f	$0.16^{+0.03}_{-0.03}$	$6.6^{+3.2}_{-1.3}$	0.58^f	1.96^f	$3.5^{+0.2}_{-0.3}$	1.54^f	5.7^f	$0.716^{+0.03}_{-0.03}$	$0.27^{+0.17}_{-0.17}$	-7^{+2}_{-2}	89.2/85

Note Errors quoted in this table are the 90 % confidence intervals.

^f Fixed parameter.

(1) The emission measure integrated over the line of sight, $(1/4\pi) \int n_e n_H ds$ in the unit of $10^{14} \text{ cm}^{-5} \text{ Sr}^{-1}$.

(2) photons $\text{s}^{-1} \text{ cm}^{-2} \text{ keV}^{-1} \text{ Sr}^{-1}$ @ 1 keV.

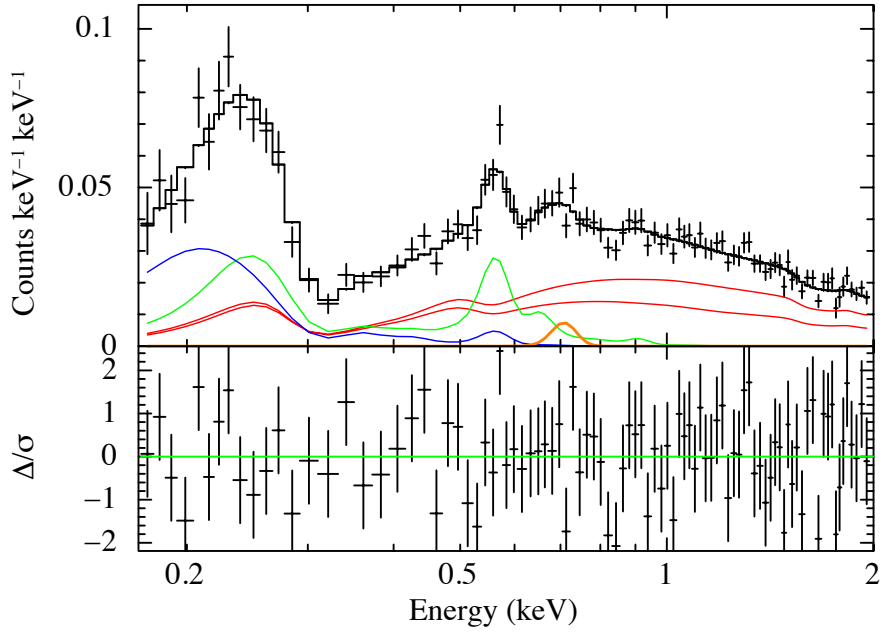


Fig. 5.17 Spectral fit to the LH06-09 spectrum, adding a Gaussian model (thick orange line) to the LB SXDB model presented in Fig. 5.9.

5.6.2 Discrepancy between the SWCX-contributed spectrum and Gaussian H-SWCX Emission Model

In Subsection 5.4.2, the Gaussian line located at 1.34 keV, originated in $\text{Mg}_{\text{XI}} \text{K}\alpha$ is not significantly detected observationally. However in the Gaussian model, many lines from highly ionized Mg such as Mg_{VIII} , Mg_{IX} and Mg_{X} contribute to the 1/4 keV band. Here we investigate uncertainty in the model in the 1/4 keV band, assuming the solar wind contains much less Mg ions as a reasonable examination. We excluded Mg lines from the Gaussian model. The number of the emission lines were decreased from 103 to 90 in 0.17-1.5 keV. We re-performed the observation simulations based on this emission model. The Gaussian lines at 219 eV (9.6 LU) and 267 eV (6.7 LU) were changed to 225 eV (6.3 LU) and 273 eV (4.6 LU), respectively. We performed spectral fit to the SWCX-contributed spectrum and observed 4.1 (0.2-7.7) and 1.9 (0.1-3.0) LU for the lines at 225 and 273 eV, respectively. In Fig. 5.18, we compare the model and observed emission intensity for each line. Although there is still a difference between the model and observation, the discrepancy becomes smaller compared with the Gaussian model with Mg (see Fig. 5.16).

This inspection result supports the hypothesis that the contribution from heavier ions to the H-SWCX spectrum tends to be overestimated in Koutroumpa et al. (2009). Presumptively, if the same verification is possible for other ions like Si, S and Fe, the difference between the model and observation will be further reduced. The ACX model predict almost no contribution to the 1/4 keV band. Therefore, the SWCX-contributed spectrum observed in the solar maximum period is in-between the spectra predicted by the ACX model and Koutroumpa et al. (2009). The SWCX-contributed spectrum presented in this thesis would be useful for testing SWCX models which will be proposed in the future.

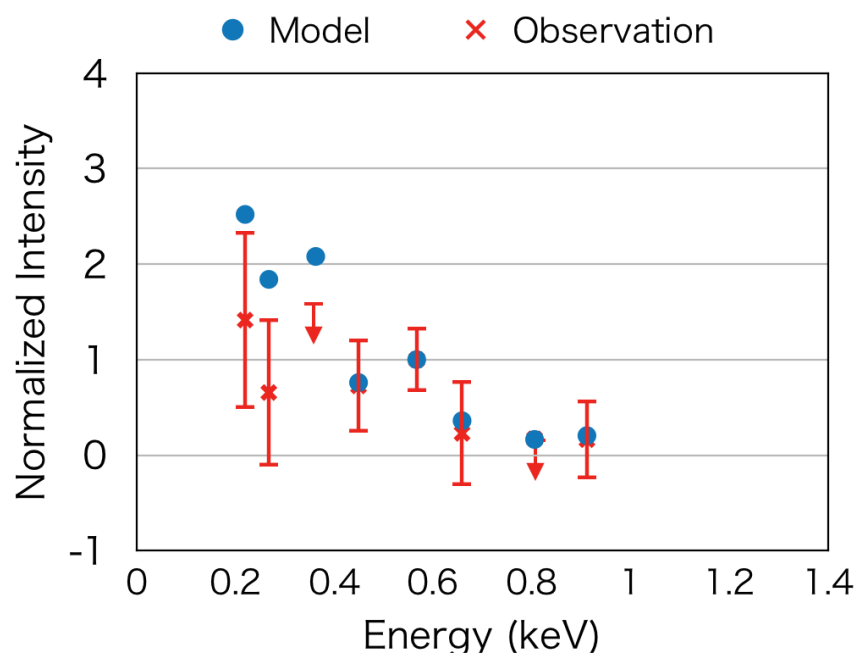


Fig. 5.18 Comparison of the intensity for each emission line between the observation and the Gaussian H-SWCX model without Mg contributions. The intensities are normalized by the ones for $O_{VII} K\alpha$ located at 567 eV. The error bars indicate 90 % statistical error range (The error for the $O_{VII} K\alpha$ is propagated to calculate the errors for line ratios).

5.6.3 Pressure of the LB

We estimate the pressure of the LB using the spectral fit parameters obtained with the LB model for the LH06-09 spectrum. Figure 5.19 shows a 3D neutral density map cut out along with the cross section of 150° - 330° . The contours show H_I walls with Na_I absorption equivalent width for $20 \text{ m}\text{\AA}$ and $50 \text{ m}\text{\AA}$. The line-of-sight toward the Lockman Hole field is indicated with the blue line. From the plot, we can read the length of the LB to be about 230 pc.

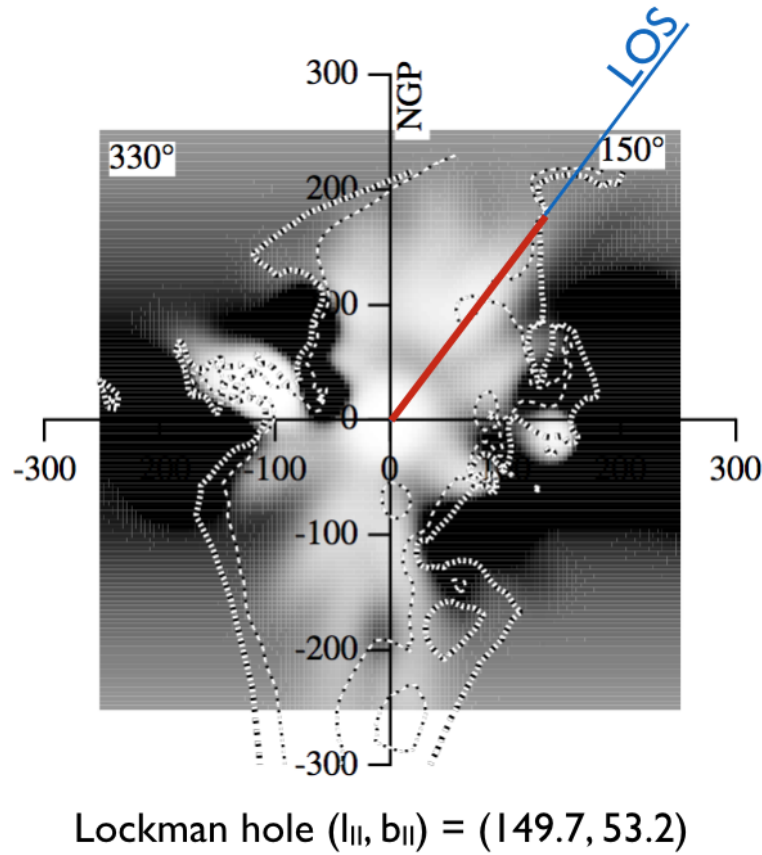


Fig. 5.19 Pictures taken from Lallement et al. (2003), showing iso equivalent width contours for $20 \text{ m}\text{\AA}$ and $50 \text{ m}\text{\AA}$, and cut in the 3D volumic density obtained from the global inversion of the column densities. The density map is cut out along with the cross section of 150° - 330° . The line-of-sight (LOS) toward the Lockman hole is indicated with a blue line. A red solid line indicates the distance from the Sun to the LB boundary ($W = 50 \text{ m}\text{\AA}$). From the figure, the distance can be read about 230 pc.

The definition of the normalization is the emission measure along the line of sight written as

$$\text{norm} = \frac{1}{4\pi} \int n_e n_H dl, \quad (5.1)$$

where n_e and n_H are the electron and proton densities, respectively. if we assume n_e and n_H distribute uniformly along the path length L , the electron density is written as

$$n_e n_H = \frac{4\pi \cdot \text{norm}}{L} \quad (5.2)$$

$$n_e = \sqrt{\frac{4\pi \cdot \text{norm}}{1.2L}}, \quad (5.3)$$

where $n_e n_H = n_e^2/1.2$ is assumed as the fully ionized plasma with 10% of He. The thermal pressure of the plasma p/k is then

$$p/k = n_{\text{total}} T_{\text{Kelvin}} \quad (5.4)$$

$$= 1.92 n_e T_{\text{Kelvin}} \quad (5.5)$$

$$= 1.92 \sqrt{\frac{4\pi \cdot \text{norm}}{1.2L}} \cdot 1.16 \times 10^7 T_{\text{keV}}, \quad (5.6)$$

where n_{total} is the total particle density defined as $n_t = 1.92 n_e$ in this case. If we assume the path length L is 230 pc read from Fig. 5.19, we obtain

$$p/k = 8.1 (5.9 - 9.1) \times 10^3 \text{ cm}^{-3} \text{ K}, \quad (5.7)$$

where the error is given as the 90 % confidence level calculated by using a kT – norm contour plot presented in Fig. 5.20. This value is still higher than the ISM pressure of $\sim p/k = 2 \times 10^3 \text{ cm}^{-3} \text{ K}$ but about half of the LB pressure estimated by Tanaka and Bleeker (1977). The pressure of the magnetic field is estimated to be $\sim p/k = 8 \times 10^3 \text{ cm}^{-3} \text{ K}$. Therefore, if the LB is relatively free of the global magnetic field, it can be in pressure equilibrium with the environment around the LB. It would be possible to consider that the magnetic field was swept out when the LB was created as a result of several supernova explosions. A similar LB pressure of $p/k = 10.6 (9.5 - 11.7) \times 10^3 \text{ cm}^{-3} \text{ K}$ is recently reported by Snowden et al. (2014). However, one of the difference from us is that they had to subtract the H-SWCX emission from the *ROSAT* observation data by assuming a H-SWCX contribution to the 1/4 keV band. Our analysis is more robust because we derived the LB properties from the spectral fit with the self-consistent SXDB model and no assumption on

the H-SWCX emission is required. Our result contains a possible contamination from the H-SWCX emission. Therefore, the LB pressure could be lower than what we estimated but not higher than this value.

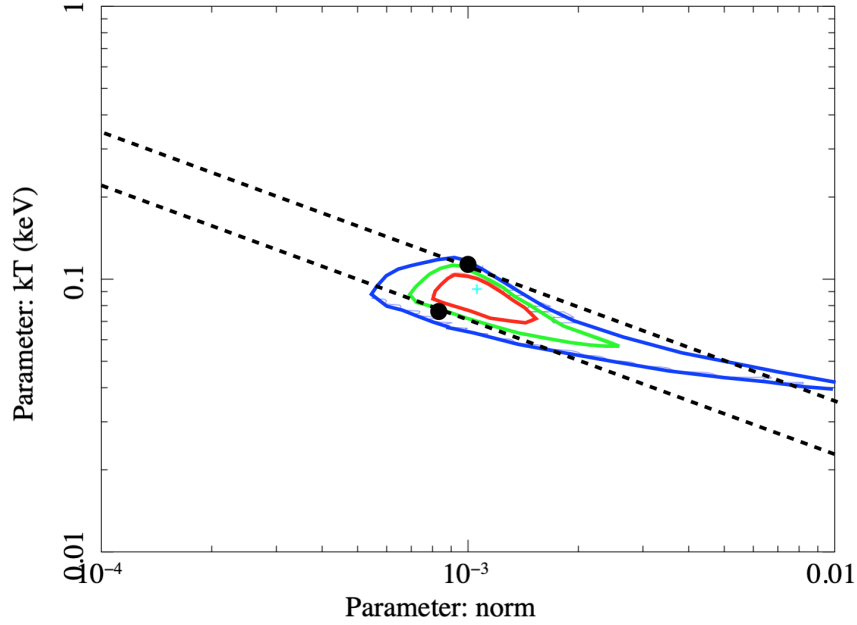


Fig. 5.20 68 % (red), 90 % (green) and 99 % (blue) confidence contours of the LB temperature vs. normalization. The broken lines indicate the relation $kT \times \text{norm} = \text{const.}$ that were used to estimate the upper and lower values of the 90 % statistical errors for the LB pressure. Note that the norm here is an Xspec normalization, not the emission measure integrated over the line of sight.

Chapter 6

Conclusions

In this thesis, we have deepened our understanding about the SXDB through the spectral analyses of the SXDB spectrum including the 1/4 keV band, by bringing out the maximum abilities of the XIS1 CCD instrument on-board the *Suzaku* observatory. Here we summarize our new findings.

We carefully analyzed the data biannually taken from 2005 to 2014 for the neutron star RXJ1856.5-3745 and discovered that sulfur, as a new contaminant element, well explains degradation of the quantum efficiency below 0.3 keV. We developed the new contamination growth curves of C, N, O and S. With these calibration curves, we validated the calibration accuracy is significantly improved within $\pm 10\%$ below 0.4 keV from 2005 to 2014.

We studied the SXDB in 0.1-2.0 keV toward the Lockman Hole field, employing the emission model consisting of the LB, H-SWCX, hot ISM and CXB. We first compared the spectra observed in the solar minimum (2006-2009) and solar maximum (2010-2012) periods and found that a systematic brightening in the spectrum in 0.17-1.0 keV in the later one. This result directly proves that the H-SWCX emission does contribute to the SXDB spectrum including the 1/4 keV band, at least in the solar maximum period.

On the other hand, the spectrum in the 1/4 keV band taken during the solar minimum period is well explained by the LB thermal model characterized with the temperature of 0.093 (0.06-0.11) keV. The temperature of the hot ISM is simultaneously determined as 0.18 (0.15-0.21) keV. These values naturally fit into the picture of the SXDB, emerged from studies that have been done in the past.

The SWCX-contributed spectrum was evaluated with existing H-SWCX models; the ACX model and the H-SWCX spectrum calculated by Koutroumpa et al. (2009), and revealed that both models cannot fully explain the observation. There seems an uncertainty in modeling of the emissions from heavier ions for example Si, S, Mg and Fe, whereas the emissions

from C, N and O are in good agreement with the observed spectrum. The SWCX-contributed spectrum would be useful for testing SWCX models which will be proposed in the future.

We estimated the pressure of the LB to be $p/k = 8.1 (5.9 - 9.1) \times 10^3 \text{ cm}^{-3} \text{ K}$. This value is still higher than the ISM pressure of $\sim p/k = 2 \times 10^3 \text{ cm}^{-3} \text{ K}$ but about half of the LB pressure estimated by Tanaka and Bleeker (1977). The pressure of the magnetic field is estimated to be $\sim p/k = 8 \times 10^3 \text{ cm}^{-3} \text{ K}$. If the LB is relatively free of the global magnetic field, then it can be in pressure equilibrium with the environment around the LB. It would be possible to consider that the magnetic field was swept out when the LB was created as a result of several supernova explosions.

References

- Anders, E. and Grevesse, N. (1989). Abundances of the elements - Meteoritic and solar. *Geochimica et Cosmochimica Acta*, 53:197–214.
- Asplund, M., Grevesse, N., Sauval, A. J., and Scott, P. (2009). The Chemical Composition of the Sun. *Annual Review of Astron and Astrophys*, 47:481–522.
- Bautz, M. W., Kissel, S. E., Prigozhin, G. Y., Lamarr, B., Burke, B. E., and Gregory, J. A. (2004). Progress in x-ray CCD sensor performance for the Astro-E2 X-ray imaging spectrometer. In Holland, A. D., editor, *High-Energy Detectors in Astronomy*, pages 111–123. International Society for Optics and Photonics.
- Beuermann, K., Burwitz, V., and Rauch, T. (2006). Establishing HZ43 A, Sirius B, and RX J185635-3754 as soft X-ray standards: a cross-calibration between the Chandra LETG+HRC-S, the EUVE spectrometer, and the ROSAT PSPC. *A&A*, 458(2):541–552.
- Boldt, E. (1992). The Extragalactic Volume X-Ray Emissivity. In Barcons, X. and Fabian, A. C., editors, *The X-ray Background*, page 115.
- Bowyer, C. S., Field, G. B., and Mack, J. E. (1968). Detection of an Anisotropic Soft X-ray Background Flux. *Nature*, 217:32–34.
- Burwitz, V., Haberl, F., Neuhäuser, R., Predehl, P., Trumper, J., and Zavlin, V. E. (2003). The thermal radiation of the isolated neutron star RX J1856.5-3754 observed with Chandra and XMM-Newton. *A&A*, 399:1109–1114.
- Clayton, D. (2003). *Handbook of Isotopes in the Cosmos*.
- Cox, D. P. (2005). The Three-Phase Interstellar Medium Revisited. *Annual Review of Astron and Astrophys*, 43:337–385.
- Cox, R. G. (1998). Inertial and viscous effects on dynamic contact angles. *Journal of Fluid Mechanics*, 357:249–278.
- Cumbee, R. S., Henley, D. B., Stancil, P. C., Shelton, R. L., Nolte, J. L., Wu, Y., and Schultz, D. R. (2014). CAN CHARGE EXCHANGE EXPLAIN ANOMALOUS SOFT X-RAY EMISSION IN THE CYGNUS LOOP? *ApJ*, 787(2):L31–5.
- Dickey, J. M. and Lockman, F. J. (1990). H I in the Galaxy. *Annual Review of Astron and Astrophys*, 28:215–261.

- Fujimoto, R., Mitsuda, K., McCammon, D., Takei, Y., Bauer, M., Ishisaki, Y., Porter, S. F., Yamaguchi, H., Hayashida, K., and Yamasaki, N. Y. (2007). Evidence for Solar-Wind Charge-Exchange X-Ray Emission from the Earth's Magnetosheath. *Publications of the Astronomical Society of Japan*, 59(sp1):133–140.
- Giacconi, R., Gursky, H., Paolini, F. R., and Rossi, B. B. (1962). Evidence for x Rays From Sources Outside the Solar System. *Physical Review Letters*, 9(11):439–443.
- Gilli, R., Comastri, A., and Hasinger, G. (2007). The synthesis of the cosmic X-ray background in the Chandra and XMM-Newton era. *A&A*, 463(1):79–96.
- Hagihara, T., Yamasaki, N. Y., Mitsuda, K., Takei, Y., Sakai, K., Yao, Y., Wang, Q. D., and McCammon, D. (2011). An X-Ray Spectroscopic Study of the Hot Interstellar Medium toward the Galactic Bulge. *Publications of the Astronomical Society of Japan*, 63:S889–S901.
- Hasinger, G., Burg, R., Giacconi, R., Hartner, G., Schmidt, M., Trumper, J., and Zamorani, G. (1993). A Deep X-Ray Survey in the Lockman-Hole and the Soft X-Ray N-Log. *Astronomy & Astrophysics*, 275:1.
- Henley, D. B. and Shelton, R. L. (2013). An XMM-Newton Survey of the Soft X-Ray Background. III. The Galactic Halo X-Ray Emission. *ApJ*, 773(2):92.
- Henley, D. B. and Shelton, R. L. (2015). XMM-Newton and Suzaku X-Ray Shadowing Measurements of the Solar Wind Charge Exchange, Local Bubble, and Galactic Halo Emission. *ApJ*, 808(1):22.
- Henry, R. C., Fritz, G., Meekins, J., Friedman, H., and Byram, E. T. (1968). Possible Detection of a Dense Intergalactic Plasma. *Astrophysical Journal Letters*, 153:L11.
- Ishisaki, Y., Maeda, Y., Fujimoto, R., Ozaki, M., Ebisawa, K., Takahashi, T., Ueda, Y., Ogasaka, Y., Ptak, A., Mukai, K., Hamaguchi, K., Hirayama, M., Kotani, T., Kubo, H., Shibata, R., Ebara, M., Furuzawa, A., Iizuka, R., Inoue, H., Mori, H., Okada, S., Yokoyama, Y., Matsumoto, H., Nakajima, H., Yamaguchi, H., Anabuki, N., Tawa, N., Nagai, M., Katsuda, S., Hayashida, K., Bamba, A., Miller, E. D., Sato, K., and Yamasaki, N. Y. (2007). Monte Carlo Simulator and Ancillary Response Generator of Suzaku XRT/XIS System for Spatially Extended Source Analysis. *Publications of the Astronomical Society of Japan*, 59(sp1):S113–S132.
- Kalberla, P. M. W., Burton, W. B., Hartmann, D., Arnal, E. M., Bajaja, E., Morras, R., and Pöppel, W. G. L. (2005). The Leiden/Argentine/Bonn (LAB) Survey of Galactic HI. Final data release of the combined LDS and IAR surveys with improved stray-radiation corrections. *Astronomy & Astrophysics*, 440:775–782.
- Koutroumpa, D., Lallement, R., and Kharchenko, V. (2009). The Spectrum of the Solar Wind Charge Exchange Emission: Contribution to the Soft X-ray Background. In *THE LOCAL BUBBLE AND BEYOND II: Proceedings of the International Conference. AIP Conference Proceedings*, pages 62–73. UMR 7620, IPSL/Service d'Aéronomie, CNRS, Université Versailles-Saint Quentin en Yvelines, Université Pierre et Marie Curie, Verrières-le-Buisson, France.

- Koyama, K., Tsunemi, H., Dotani, T., Bautz, M. W., Hayashida, K., Tsuru, T. G., Matsumoto, H., Ogawara, Y., Ricker, G. R., Doty, J., Kissel, S. E., Foster, R., Nakajima, H., Yamaguchi, H., Mori, H., Sakano, M., Hamaguchi, K., Nishiuchi, M., Miyata, E., Torii, K., Namiki, M., Katsuda, S., Matsuura, D., Miyauchi, T., Anabuki, N., Tawa, N., Ozaki, M., Murakami, H., Maeda, Y., Ichikawa, Y., Prigozhin, G. Y., Boughan, E. A., Lamarr, B., Miller, E. D., Burke, B. E., Gregory, J. A., Pillsbury, A., Bamba, A., Hiraga, J. S., Senda, A., Katayama, H., Kitamoto, S., Tsujimoto, M., Kohmura, T., Tsuboi, Y., and Awaki, H. (2007). X-Ray Imaging Spectrometer (XIS) on Board Suzaku. *Publications of the Astronomical Society of Japan*, 59(sp1):23–33.
- Kuntz, K. D. (2019). Solar wind charge exchange: an astrophysical nuisance. *The Astronomy and Astrophysics Review*, 27(1):1.
- Kushino, A., Ishisaki, Y., Morita, U., Yamasaki, N. Y., Ishida, M., Ohashi, T., and Ueda, Y. (2002). Study of the X-Ray Background Spectrum and Its Large-Scale Fluctuation with ASCA. *Publications of the Astronomical Society of Japan*, 54:327–352.
- Lallement, R., Vergely, J. L., Valette, B., Puspitarini, L., Eyer, L., and Casagrande, L. (2014). 3D maps of the local ISM from inversion of individual color excess measurements. *A&A*, 561:A91–17.
- Lallement, R., Welsh, B. Y., Vergely, J. L., Crifo, F., and Sfeir, D. (2003). 3D mapping of the dense interstellar gas around the Local Bubble. *Astronomy & Astrophysics*, 411:447–464.
- Lallement, R., Welsh, B. Y., Vergely, J. L., Crifo, F., and Sfeir, D. (2003). 3D mapping of the dense interstellar gas around the Local Bubble. *A&A*, 411:447–464.
- Lehmer, B. D., Xue, Y. Q., Brandt, W. N., Alexander, D. M., Bauer, F. E., Brusa, M., Comastri, A., Gilli, R., Hornschemeier, A. E., Luo, B., Paolillo, M., Ptak, A., Shemmer, O., Schneider, D. P., Tozzi, P., and Vignali, C. (2012). The 4 Ms Chandra Deep Field-South Number Counts Apportioned by Source Class: Pervasive Active Galactic Nuclei and the Ascent of Normal Galaxies. *ApJ*, 752(1):46.
- Lisse, C. M., Dennerl, K., Englhauser, J., Harden, M., Marshall, F. E., Mumma, M. J., Petre, R., Pye, J. P., Ricketts, M. J., Schmitt, J., Trümper, J., and West, R. G. (1996). Discovery of x-ray and extreme ultraviolet emission from comet c/hyakutake 1996 b2. *Science*, 274(5285):205–209.
- Lodders, K. (2003). Solar System Abundances and Condensation Temperatures of the Elements. *Astrophysical Journal*, 591:1220–1247.
- Luo, B., Brandt, W. N., Xue, Y. Q., Lehmer, B., Alexander, D. M., Bauer, F. E., Vito, F., Yang, G., Basu-Zych, A. R., Comastri, A., Gilli, R., Gu, Q. S., Hornschemeier, A. E., Koekemoer, A., Liu, T., Mainieri, V., Paolillo, M., Ranalli, P., Rosati, P., Schneider, D. P., Shemmer, O., Smail, I., Sun, M., Tozzi, P., Vignali, C., and Wang, J. X. (2016). THE CHANDRA DEEP FIELD-SOUTH SURVEY: 7 MS SOURCE CATALOGS. *ApJS*, 228(1):1–30.
- Mathis, J. S., Rumpl, W., and Nordsieck, K. H. (1977). The size distribution of interstellar grains. *Astrophysical Journal*, 217:425–433.

- McCammon, D., Almy, R., Apodaca, E., Bergmann Tiest, W., Cui, W., Deiker, S., Galeazzi, M., Juda, M., Lesser, A., Mihara, T., Morgenthaler, J. P., Sanders, W. T., Zhang, J., Figueroa-Feliciano, E., Kelley, R. L., Moseley, S. H., Mushotzky, R. F., Porter, F. S., Stahle, C. K., and Szymkowiak, A. E. (2002a). A High Spectral Resolution Observation of the Soft X-Ray Diffuse Background with Thermal Detectors. *ApJ*, 576(1):188–203.
- McCammon, D., Almy, R., Apodaca, E., Bergmann Tiest, W., Cui, W., Deiker, S., Galeazzi, M., Juda, M., Lesser, A., Mihara, T., Morgenthaler, J. P., Sanders, W. T., Zhang, J., Figueroa-Feliciano, E., Kelley, R. L., Moseley, S. H., Mushotzky, R. F., Porter, F. S., Stahle, C. K., and Szymkowiak, A. E. (2002b). A High Spectral Resolution Observation of the Soft X-Ray Diffuse Background with Thermal Detectors. *ApJ*, 576(1):188–203.
- McCammon, D. and Sanders, W. T. (1990). The soft X-ray background and its origins. *IN: Annual review of astronomy and astrophysics. Vol. 28 (A91-28201 10-90). Palo Alto*, 28(1):657–688.
- Mitsuda, K., Bautz, M., Inoue, H., Kelley, R. L., Koyama, K., Kunieda, H., Makishima, K., Ogawara, Y., Petre, R., Takahashi, T., Tsunemi, H., White, N. E., Anabuki, N., Angelini, L., Arnaud, K., Awaki, H., Bamba, A., Boyce, K., Brown, G. V., Chan, K.-W., Cottam, J., Dotani, T., Doty, J., Ebisawa, K., Ezoe, Y., Fabian, A. C., Figueroa, E., Fujimoto, R., Fukazawa, Y., Furusho, T., Furuzawa, A., Gendreau, K., Griffiths, R. E., Haba, Y., Hamaguchi, K., Harrus, I., Hasinger, G., Hatsukade, I., Hayashida, K., Henry, P. J., Hiraga, J. S., Holt, S. S., Hornschemeier, A., Hughes, J. P., Hwang, U., Ishida, M., Ishisaki, Y., Isobe, N., Itoh, M., Iyomoto, N., Kahn, S. M., Kamae, T., Katagiri, H., Kataoka, J., Katayama, H., Kawai, N., Kilbourne, C., Kinugasa, K., Kissel, S., Kitamoto, S., Kohama, M., Kohmura, T., Kokubun, M., Kotani, T., Kotoku, J., Kubota, A., Madejski, G. M., Maeda, Y., Makino, F., Markowitz, A., Matsumoto, C., Matsumoto, H., Matsuoka, M., Matsushita, K., McCammon, D., Mihara, T., Misaki, K., Miyata, E., Mizuno, T., Mori, K., Mori, H., Morii, M., Moseley, H., Mukai, K., Murakami, H., Murakami, T., Mushotzky, R., Nagase, F., Namiki, M., Negoro, H., Nakazawa, K., Nousek, J. A., Okajima, T., Ogasaka, Y., Ohashi, T., Oshima, T., Ota, N., Ozaki, M., Ozawa, H., Parmar, A. N., Pence, W. D., Porter, F. S., Reeves, J. N., Ricker, G. R., Sakurai, I., Sanders, W. T., Senda, A., Serlemitsos, P., Shibata, R., Soong, Y., Smith, R., Suzuki, M., Szymkowiak, A. E., Takahashi, H., Tamagawa, T., Tamura, K., Tamura, T., Tanaka, Y., Tashiro, M., Tawara, Y., Terada, Y., Terashima, Y., Tomida, H., Torii, K., Tsuboi, Y., Tsujimoto, M., Tsuru, T. G., Turner, M. J. L., Ueda, Y., Ueno, S., Ueno, M., Uno, S., Urata, Y., Watanabe, S., Yamamoto, N., Yamaoka, K., Yamasaki, N. Y., Yamashita, K., Yamauchi, M., Yamauchi, S., Yaqoob, T., Yonetoku, D., and Yoshida, A. (2007). The X-Ray Observatory Suzaku. *Publications of the Astronomical Society of Japan*, 59(sp1):1–7.
- Neuhäuser, R., Walter, F. M., and Wolk, S. J. (1996). ROSAT Observations of Isolated Neutron Stars. In Greiner, J., editor, *Supersoft X-Ray Sources*, volume 472 of *Lecture Notes in Physics*, Berlin Springer Verlag, page 279.
- Plucinsky, Paul P., Beardmore, Andrew P., Foster, Adam, Haberl, Frank, Miller, Eric D., Pollock, Andrew M. T., and Sembay, Steve (2017). Snr 1e 0102.2-7219 as an x-ray calibration standard in the 0.5-1.0 keV bandpass and its application to the CCD instruments aboard Chandra, Suzaku, Swift and XMM-Newton. *A&A*, 597:A35.

- Pons, J. A., Walter, F. M., Lattimer, J. M., Prakash, M., Neuhäuser, R., and An, P. (2002). Toward a Mass and Radius Determination of the Nearby Isolated Neutron Star RX J185635-3754. *Astrophysical Journal*, 564:981–1006.
- Revnivtsev, M., Gilfanov, M., Sunyaev, R., Jahoda, K., and Markwardt, C. (2003). The spectrum of the cosmic X-ray background observed by RTXE/PCA. *Astronomy & Astrophysics*, 411:329–334.
- Sakai, K., Yao, Y., Mitsuda, K., Yamasaki, N. Y., Wang, Q. D., Takei, Y., and McCammon, D. (2014). Structural study of Galactic hot gas toward Markarian 421 from X-ray absorption and emission lines. *Publications of the Astronomical Society of Japan*, 66:83.
- Sekiya, N., Yamasaki, N. Y., Mitsuda, K., and Takei, Y. (2014). O I fluorescent line contamination in soft X-ray diffuse background obtained with Suzaku/XIS. *Publications of the Astronomical Society of Japan*, 66(2):L3–L3.
- Serlemitsos, P. J., Soong, Y., Chan, K.-W., Okajima, T., Lehan, J. P., Maeda, Y., Itoh, K., Mori, H., Iizuka, R., Itoh, A., Inoue, H., Okada, S., Yokoyama, Y., Itoh, Y., Ebara, M., Nakamura, R., Suzuki, K., Ishida, M., Hayakawa, A., Inoue, C., Okuma, S., Kubota, R., Suzuki, M., Osawa, T., Yamashita, K., Kunieda, H., Tawara, Y., Ogasaka, Y., Furuzawa, A., Tamura, K., Shibata, R., Haba, Y., Naitou, M., and Misaki, K. (2007). The X-Ray Telescope onboard Suzaku. *Publications of the Astronomical Society of Japan*, 59:S9–S21.
- Smith, R. K., Bautz, M. W., Edgar, R. J., Fujimoto, R., Hamaguchi, K., Hughes, J. P., Ishida, M., Kelley, R., Kilbourne, C. A., Kuntz, K. D., McCammon, D., Miller, E., Mitsuda, K., Mukai, K., Plucinsky, P. P., Porter, F. S., Snowden, S. L., Takei, Y., Terada, Y., Tsuboi, Y., and Yamasaki, N. Y. (2007). Suzaku Observations of the Local and Distant Hot ISM. *Publications of the Astronomical Society of Japan*, 59(sp1):141–150.
- Smith, R. K., Foster, A. R., Edgar, R. J., and Brickhouse, N. S. (2014). Resolving the Origin of the Diffuse Soft X-Ray Background. *Astrophysical Journal*, 787:77.
- Snowden, S. L., Chiao, M., Collier, M. R., Porter, F. S., Thomas, N. E., Cravens, T., Robertson, I. P., Galeazzi, M., Uprety, Y., Ursino, E., Koutroumpa, D., Kuntz, K. D., Lallement, R., Puspitarini, L., Lepri, S. T., McCammon, D., Morgan, K., and Walsh, B. M. (2014). Pressure Equilibrium between the Local Interstellar Clouds and the Local Hot Bubble. *The Astrophysical Journal Letters*, 791(1):L14.
- Snowden, S. L., Egger, R., Finkbeiner, D. P., Freyberg, M. J., and Plucinsky, P. P. (1998). Progress on Establishing the Spatial Distribution of Material Responsible for the 1–4 keV Soft X-Ray Diffuse Background Local and Halo Components. *Astrophysical Journal*, 493:715–729.
- Snowden, S. L., McCammon, D., and Verter, F. (1993). The X-ray shadow of the high-latitude molecular cloud MBM 12. *Astrophysical Journal Letters*, 409:L21–L24.
- Tanaka, Y. and Bleeker, J. A. M. (1977). The diffuse soft X-ray sky - Astrophysics related to cosmic soft X-rays in the energy range 0.1–2.0 keV. *Space Sci Rev*, 20:815–888.

- Tawa, N., Hayashida, K., Nagai, M., Nakamoto, H., Tsunemi, H., Yamaguchi, H., Ishisaki, Y., Miller, E. D., Mizuno, T., Dotani, T., Ozaki, M., and Katayama, H. (2008). Reproducibility of Non-X-Ray Background for the X-Ray Imaging Spectrometer aboard Suzaku. *Publications of the Astronomical Society of Japan*, 60(sp1):S11–S24.
- Walter, F. M., Eisenbeiß, T., Lattimer, J. M., Kim, B., Hambaryan, V., and Neuhäuser, R. (2010). Revisiting the Parallax of the Isolated Neutron Star RX J185635-3754 Using HST/ACS Imaging. *Astrophysical Journal*, 724:669–677.
- Yao, Y., Wang, Q. D., Hagihara, T., Mitsuda, K., McCammon, D., and Yamasaki, N. Y. (2009). X-Ray and Ultraviolet Spectroscopy of Galactic Diffuse Hot Gas Along the Large Magellanic Cloud X-3 Sight Line. *Astrophysical Journal*, 690:143–153.
- Yoshino, T., Mitsuda, K., Yamasaki, N. Y., Takei, Y., Hagihara, T., Masui, K., Bauer, M., McCammon, D., Fujimoto, R., Daniel Wang, Q., and Yao, Y. (2009). Energy Spectra of the Soft X-Ray Diffuse Emission in Fourteen Fields Observed with Suzaku. *Publications of the Astronomical Society of Japan*, 61(4):805–823.
- Yoshitake, H., Sakai, K., Mitsuda, K., Yamasaki, N. Y., Takei, Y., and Yamamoto, R. (2013). Long-Term Variability of the O VII Line Intensity toward the Lockman Hole Observed with Suzaku from 2006 to 2011. *Publications of the Astronomical Society of Japan*, 65(2):32–32.
- Zubko, V., Dwek, E., and Arendt, R. G. (2004). Interstellar Dust Models Consistent with Extinction, Emission, and Abundance Constraints. *Astrophysical Journal Supplement Series*, 152:211–249.

Appendix A

Data Screening with the Day Earth elevation angle

We investigated influence of contamination from solar X-rays scattered off the Earth's atmosphere by checking the counting rate in the 0.45-0.6 keV band, as a function of day earth elevation angle (see Fig. A.1, Fig. A.2 and Fig. A.3). A summary of the screening threshold for each observation is given in A.1.

Table A.1 Summary of the data screening threshold for the day Earth elevation angle (*DYE_EL*V).

Target	Abbreviation	Obs. ID	Date yyyy-mm-dd	<i>DYE_EL</i> V (deg.)
RXJ1856	RX05b	100041010	2005-10-24	20
	RX06a	100041020	2006-03-23	20
	RX06b	101009010	2006-10-20	10
	RX07b	102014010	2007-10-15	10
	RX08a	102015010	2008-03-22	20
	RX08b	103006010	2008-10-20	50
	RX09b	104022010	2009-10-23	30
	RX10a2	104022030	2010-03-26	20
	RX10b	105008010	2010-10-27	20
	RX11b	106009010	2011-10-22	90
	RX12a	107007010	2012-04-02	30
	RX12b	107007020	2012-10-20	60
	RX13a	108007010	2013-04-15	30
	RX14a	109008010	2014-04-08	30
	RX14b	109008020	2014-10-23	90
Lockman Hole	LH06	101002010	2006-05-17	40
	LH07	102018010	2007-05-03	40
	LH08	103009010	2008-05-18	20
	LH09	104002010	2009-06-12	10
	LH10	105003010	2010-06-11	30
	LH11	106001010	2011-05-04	100
	LH12	107001010	2012-05-05	50

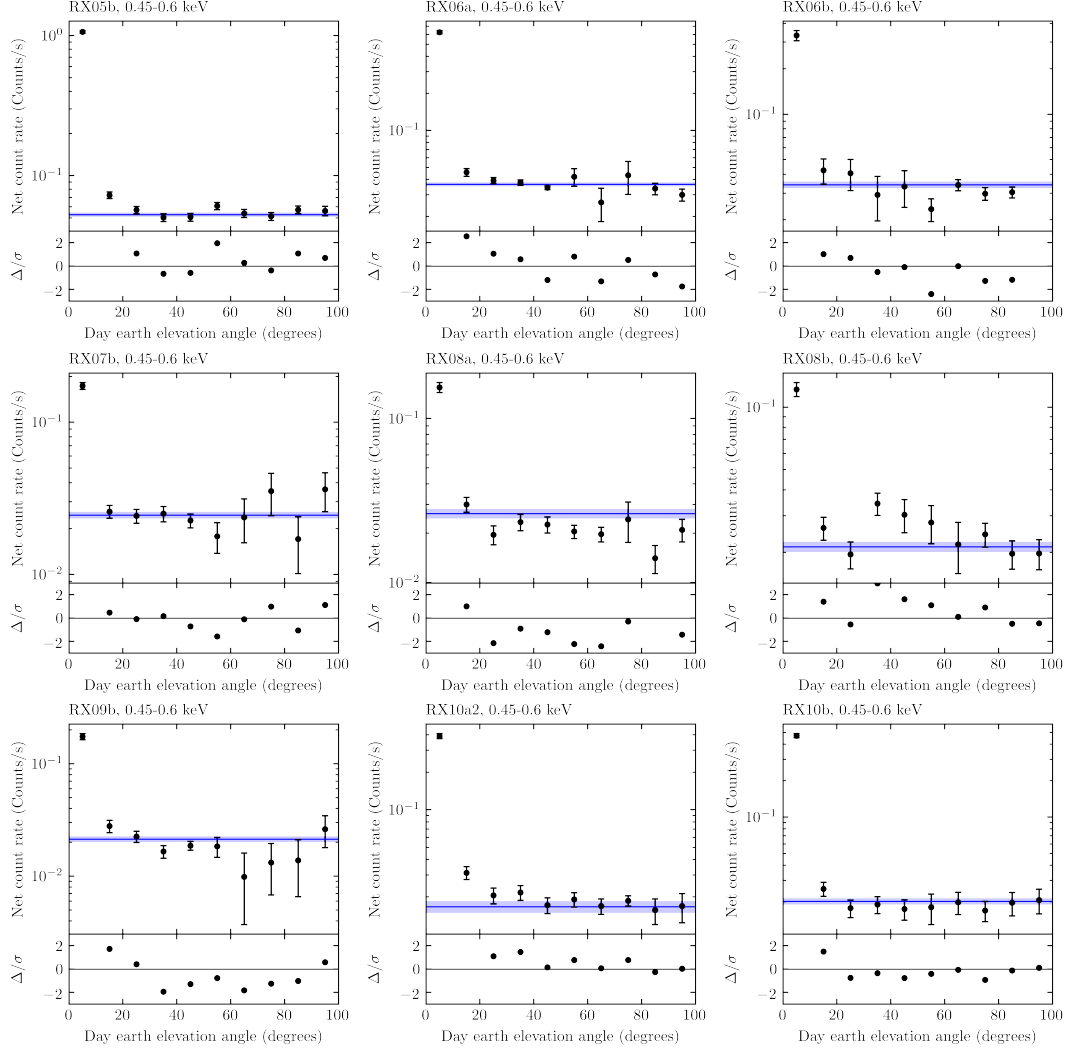


Fig. A.1 Net count rate in 0.45-0.6 keV as a function of the *DYE_ELV* angle. The results for RX05b to RX10b are presented.

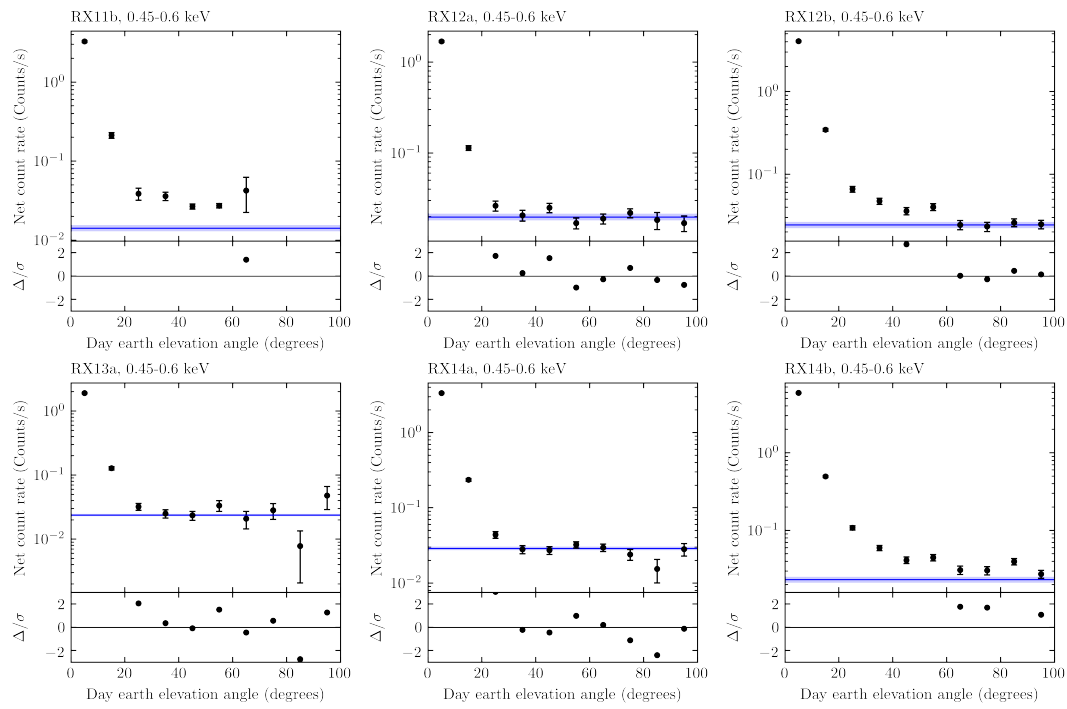


Fig. A.2 Net count rate in 0.45-0.6 keV as a function of the *DYE_ELV* angle. The results for RX11b to RX14b are presented.

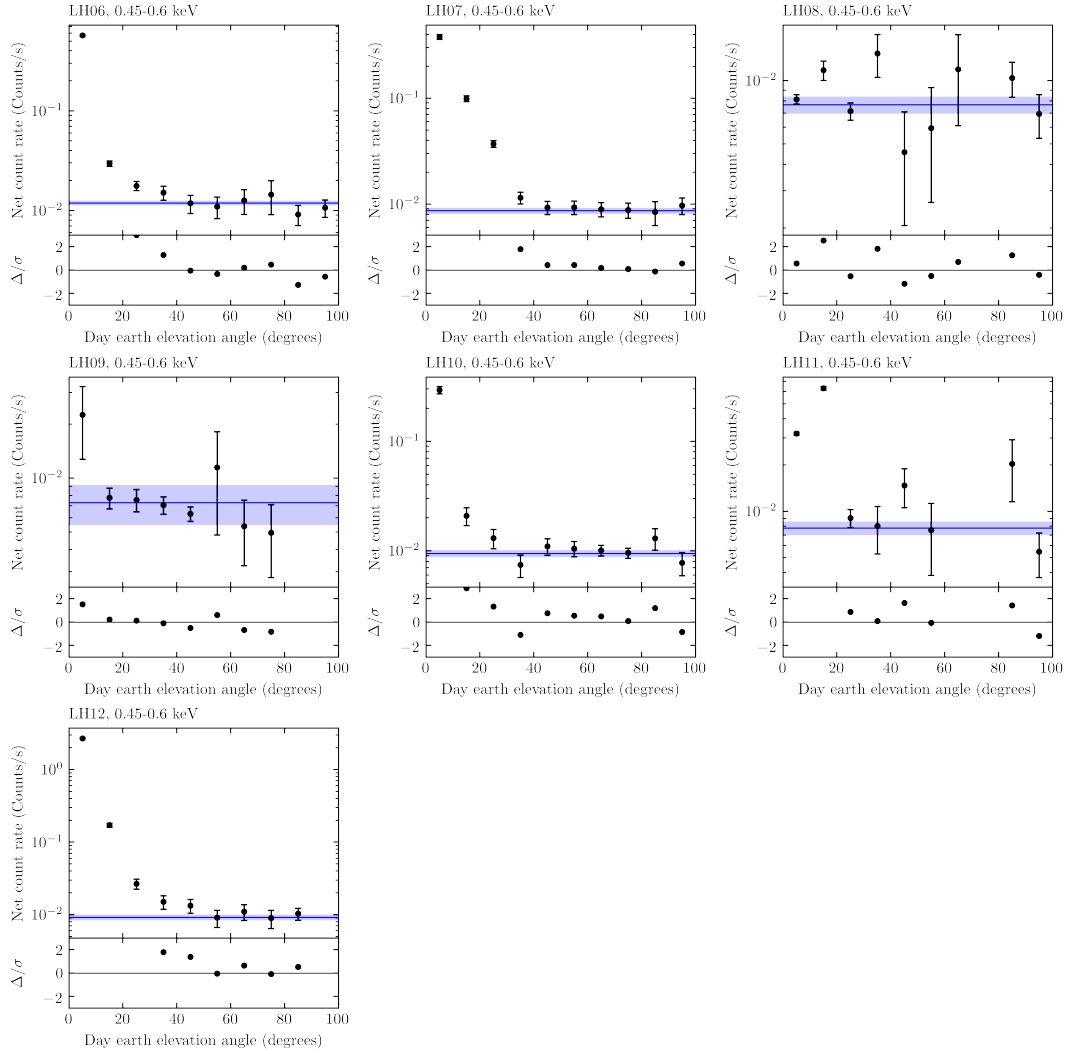


Fig. A.3 Net count rate in 0.45-0.6 keV as a function of the *DYE_ELV* angle. The results for LH06 to LH12 are presented.

Appendix B

Modeling of the H-SWCX Emission

We investigated an approximate model to the H-SWCX emission model calculated by Koutroumpa et al. (2009). We produced a mock spectrum assuming 103 zero-width Gaussian lines whose line center energies and intensities were read fixed at the values presented in Koutroumpa et al. (2009). We found that the H-SWCX model was well reproduced with 9 zero-width Gaussian lines. The simulation results are shown in Fig. B.1.

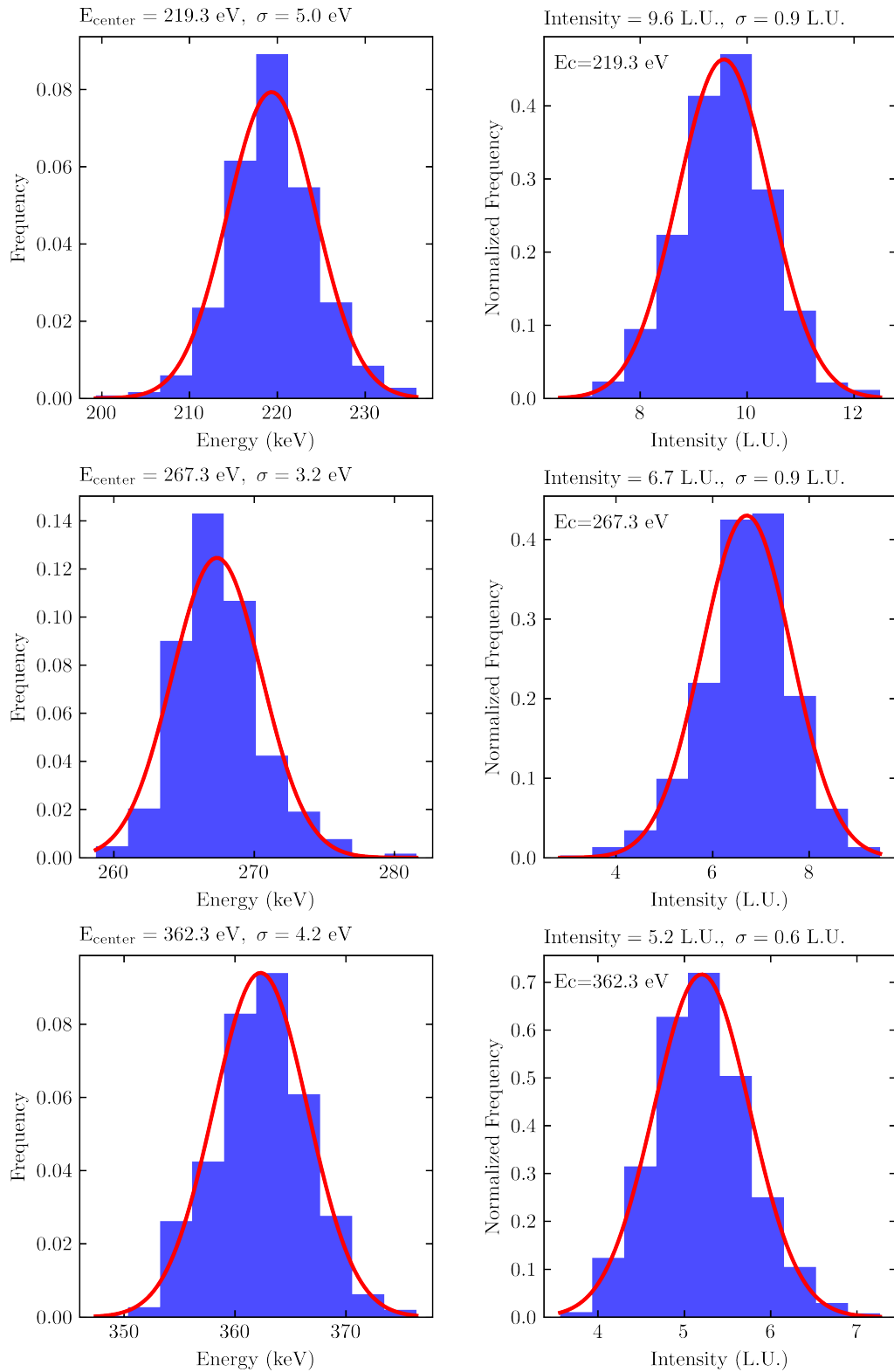


Fig. B.1 Histograms of the best fit parameters of the energy center and intensity for each line, obtained by fitting 1000 mock H-SWCX spectra with the zero-width Gaussian model.

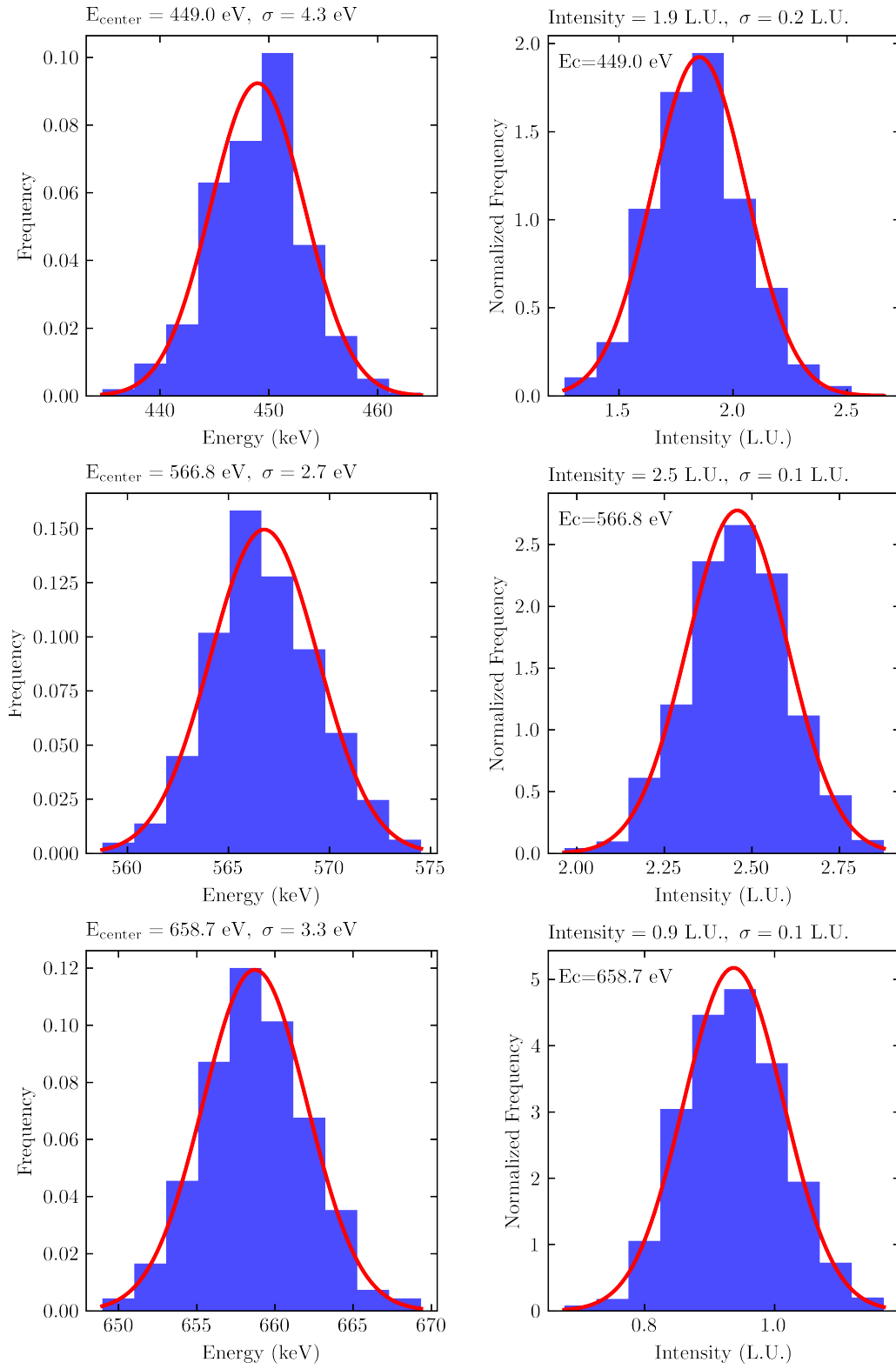


Fig. B.2 Continue from Fig. B.1

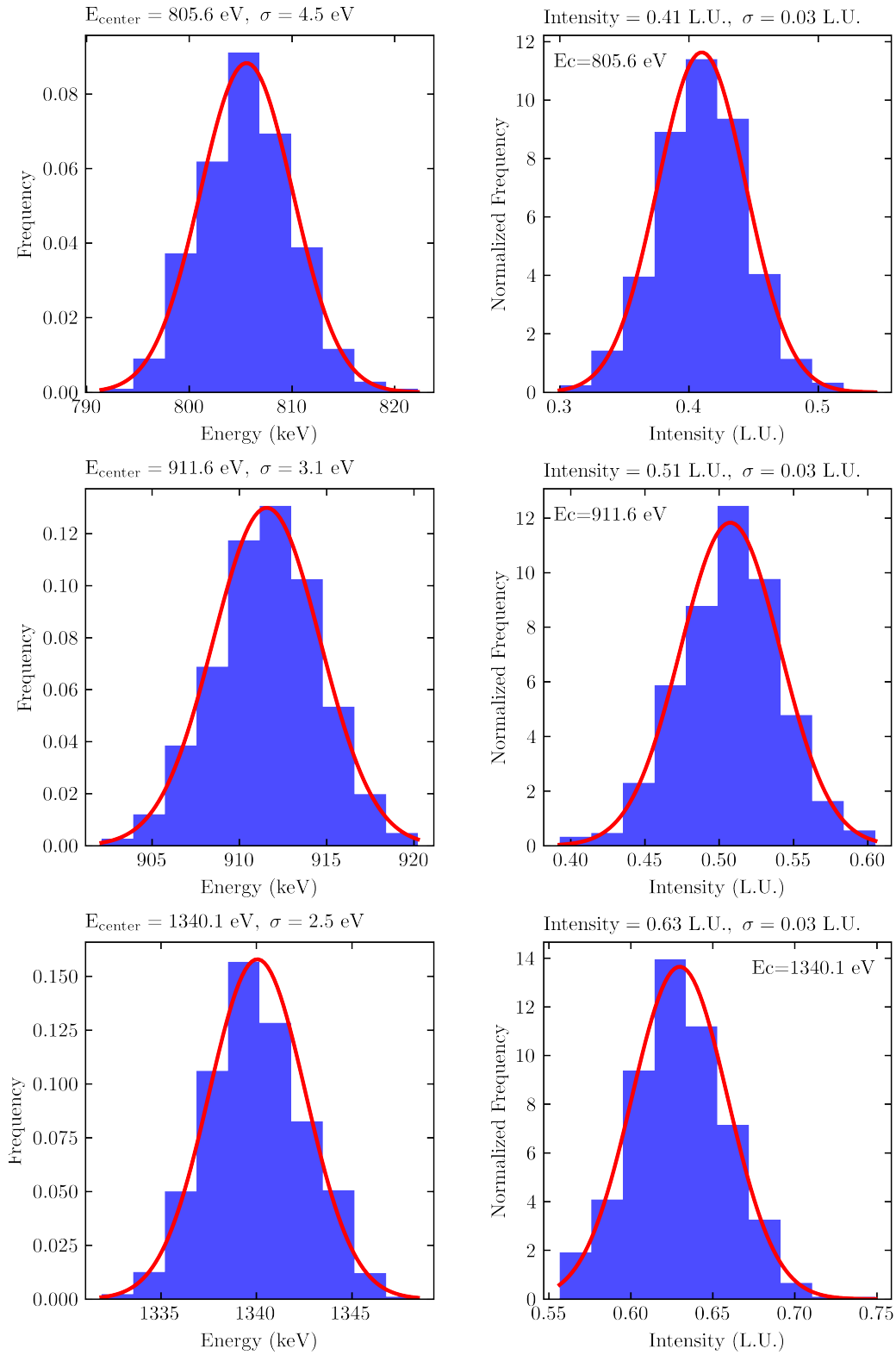


Fig. B.3 Continue from Fig. B.1